The Effect of Fluid Acceleration on Sediment Transport in the Surf Zone

By

William McKinney Durham

B.S., Civil Engineering (2004)

Clemson University

Submitted to the Department of Civil and Environmental Engineering
in Partial Fulfillment of the Requirements for the Degree of
Master of Science in Civil and Environmental Engineering

at the

Massachusetts Institute of Technology

February 2007

Signature of Author.....
Department of Civil and Environmental Engineering
October 10, 2006

Certified by .....
Ole Secher Madsen
Professor of Civil and Environmental Engineering
Thesis Supervisor

Accepted by .....
Andrew J. Whittle
Professor of Civil and Environmental Engineering
Chairman, Departmental Committee for Graduate Students

Abstract
The Effect of Fluid Acceleration on Sediment Transport in the Surf Zone

By

William M. Durham

Submitted to the Department of Civil and Environmental Engineering
on October 10, 2006 in Partial Fulfillment of the
Requirements for the Degree of Master of Science in
Civil and Environmental Engineering

ABSTRACT

The surf zone is defined by highly non-linear, breaking waves that have very different acceleration signatures beneath their respective crests and troughs. The consequences of this dissimilarity on sediment transport is not fully understood. This thesis develops methodologies to predict sediment transport under these assymetric, skewed waves. Two different transport mechanisms are considered: bedload transport and "subsurface" transport. The potential for subsurface transport was first realized by *Madsen* (1974) who found that the large pressure gradient beneath a breaking wave was sufficient to drive a substantial porous-media flow, adequate to create a soil-mechanics type failure extending several centimeters into a sandy sediment bed. The theoretical model of *Madsen* (1974) is extended to obtain estimates of subsurface transport by subdividing the sediment in failure into distinct, kinematically-admissible slipcircles. An equation governing the rotation of each slipcircle is developed, yielding the subsurface sediment's horizontal movement as a function of depth. By integration, subsurface transport can predicted. In addition, a method is developed for estimating bedload transport under breaking waves, accounting for the enhanced shear stress beneath the wave's crest. An existing bedload formula is used as the foundation for this predictive model.

The validity of the two predictive models is substantiated by experiments conducted in a laboratory wave flume. Breaking waves are passed over lightweight, plastic beads representive of uncohesive sediment. The surficial and subsurface transport is experimentally measured. Using velocity records from the laboratory waves, the theoretical models are used to make predictions of each type of transport. Both models produce good agreement with experimental observations. Finally, laboratory wave data from *Madsen* (1974) are scaled to the the size of waves typical of the surf zone. Using parameters characteristic of sand, the two models predict a subsurface transport of the same order as bedload transport for typical wave and sediment parameters. Furthermore, subsurface transport is found to be proportional to the characteristic length scale of the wave squared, while bedload transport is proportional to the length scale to the power of 1.5.

Thesis Supervisor: Ole Madsen
Title: Professor of Civil and Environmental Engineering

ACKNOWLEDGEMENTS

I would like to extend my sincere appreciation to Ole for supporting me since my arrival at MIT. His unflagging willingness to help me through any difficulties that arose in coursework, research, or any other area was marvelous. I am truly fortunate to have had the opportunity to work for such an excellent advisor.

As a UROP, Lizzie Lundgren contributed immensely to the collection and analysis of data contained in this thesis.

I would not have had the ability to make it through this endeavor without the support of my family. Dwight, Gay, Holiday and Carolyn Durham, have all provided me with a constant source of encouragement throughout this experience.

The fellow citizens of Parsons have made my time here especially enjoyable. I found the atmosphere within Parsons wonderful, both academically and socially.

Lastly, I would like to thank everyone else who shared with me the past two years; you know who you are.

The following sources of funding are gratefully acknowledged: the Department of Civil and Environmental Engineering (including a Schoettler Fellowship and teaching assistantship position) and a grant from the Office of Naval Research.

TABLE OF CONTENTS

1 - INTRODUCTION 17

1.1 MOTIVATION 17

1.2 OVERVIEW 18

2 - LITERATURE REVIEW 21

3 - EXPERIMENTAL SETUP AND INSTRUMENTATION 32

3.1 WAVE FLUME 32

3.2 TEST SECTION 33

3.3 BEAD PROPERTIES 38

3.3.1 Bead Density and Porosity 38

3.3.2 Bead Size 41

3.3.3 Internal Angle of Friction of the Beads 42

3.4 WAVE GENERATION 44

3.4.1 Three Wave Burst 45

3.4.2 Solitary Wave 48

3.5 WAVE MEASUREMENTS 52

3.5.1 Wave Gauge System 53

3.5.1.1 Measurement of Water Surface Elevation 53

3.5.1.2 Measurement of Wave Phase Velocity 56

3.5.2 Acoustic Doppler Velocimetry System 57

4 - METHODS 61

4.1 EXPERIMENTAL METHODS 61

4.1.1 Measurement of Subsurface Transport 61

4.1.2 Measurement of Surficial Transport 67

4.1.2.1 Sediment Volume Test 67

4.1.2.2 Measurement of Surficial Transport 69

4.2 THEORETICAL METHODS 75

4.2.1 Determination of Phase Velocity 75

4.2.1.1 Linear Wave Theory 75

4.2.1.2 Solitary Wave Theory 77

4.2.1.3 Cnoidal Wave Theory 77

4.2.2 Modeling Surficial Transport 78

4.2.2.1 Solitary Wave 79

4.2.2.2 Periodic Wave 85

4.2.3 Calculation of Bead Excursion Lengths 87

4.2.4 Modeling Subsurface Transport 87

4.2.4.1 Determination of the Bottom Pressure Distribution 88

4.2.4.2 Limiting Slip Circle Geometry 93

4.2.4.3 Slip Circle Geometry 97

4.2.4.4 Calculation of Subsurface Transport 101

4.2.4.4.1 Solving for Subsurface Displacement Numerically 104

4.2.4.4.2 Solving For Subsurface Displacement Analytically 106
4.2.5 Predictions of Transport Using Data from *Madsen* (1974) 110
5 - RESULTS 116
5.1 PHASE VELOCITY 116
5.1.1 Three Wave Burst 116
5.1.2 Solitary Wave 119
5.2 SURFICIAL TRANSPORT 121
5.2.1 Solitary Wave 121
5.2.1.1 Theoretical Surficial Transport – Solitary Wave 121
5.2.1.2 Experimental Surficial Transport – Solitary Wave 123
5.2.2 Three Wave Burst 126
5.2.2.1 Theoretical Surficial Transport – Three Wave Burst 126
5.2.2.2 Experimental Surficial Transport – Three Wave Burst 130
5.3 SUBSURFACE TRANSPORT 132
5.3.1 Solitary Wave 132
5.3.1.1 Comparison of Theoretical and Experimental Results 132
5.3.1.2 Sensitivity of Theoretical Model to Sediment Density 146
5.3.2 Three Wave Burst 148
5.3.2.1 Experiment with PVC Beads 148
5.3.2.2 Experiment with PET Beads 154
5.4 PROTOTYPE WAVE 159
6 – CONCLUSIONS 168

6.1 SUMMARY OF RESULTS 168
6.1.1 Surficial Transport 168
6.1.2 Subsurface Transport 169
6.1.2.1 Subsurface Sediment Seaward Movements 170
6.1.2.2 Attenuation of Subsurface Movements 173
6.1.3 Correlation of Experimental and Theoretical Results 174
6.1.4 Transport Under the Prototype Wave 176
6.2 AREAS OF FUTURE RESEARCH 179

LIST OF FIGURES

Figure 1 - Limiting Slip Circle Notation 25

Figure 2 – Schematic View of Wave Flume 32

Figure 3 – Side View of the Experimental Test Section 36

Figure 4 – Section View of the Experimental Test Section 36

Figure 5 – Device Used to Measure the Internal Angle of Friction of the Plastic Beads 42

Figure 6 - Three-Wave Burst Velocity and Pressure Gradient Time Series 47

Figure 7 – Entire Wavemaker Movement Used to Generate Solitary Wave 50

Figure 8 – Forward Wavemaker Movement Used to Generate Solitary Wave 51

Figure 9 - Solitary Wave Velocity and Pressure Gradient Time Series 52

Figure 10 – Calibration of Wave Gauge 55

Figure 11 – ADV Probe Depiction (Sontek, 2006) 58

Figure 12 - Photographs of the Colored Sediment Column (Initial and After 100 Waves) 62

Figure 13 – Experimental Colored Sediment Displacement After 100 Waves 64

Figure 14 – Experimental Subsurface Transport as a Function of Number of Waves 65

Figure 15 – Verification of Lateral Uniformity of Colored Bead Column 66

Figure 16 – Lateral Positioning of Transects 68

Figure 17 – Typical Average Surficial Transport Record for One Solitary Wave 73

Figure 18 – Velocity Record at station 50 79

Figure 19 – Velocity Points Used for Fitting Sinusoid (Method 1) 81

Figure 20 – Theoretical Bedload Measurements at Station 50 85

Figure 21 – Calculation of Friction Factors for an Assymetric Periodic Wave 86

Figure 22 - Comparison of Measured and Smoothed Velocity Time Records 90

Figure 23 - Average Pressure Gradient Record with Standard Deviations 91

Figure 24 - Pressure Gradient and Pressure Distribution..... 93

Figure 25 - Average Pressure Gradient..... 94

Figure 26 - Limiting Slip Circle Notation..... 95

Figure 27 - Limiting Slip Moment Record 96

Figure 28 - Slip Circle Geometry..... 97

Figure 29 - Slip Circle Notation..... 98

Figure 30 - Moments of Concentric Slip Circles 99

Figure 31 - Relative Slip Circle Motion Analysis 102

Figure 32 - Displacements of Slip Circles 104

Figure 33 - Angular Velocity and Angular Position Records Obtained Analytically 107

Figure 34 - Final Displacements for $\phi = 30^{\circ}$ 108

Figure 35 - Final Displacements for $\phi = 35^{\circ}$ 108

Figure 36 - Final Displacements for $\phi = 40^{\circ}$ 109

Figure 37 – Types of Breaking Waves 112

Figure 38 – Smoothed Pressure Gradient Obtained from *Madsen* (1974)..... 113

Figure 39 – Wave Gauge Data from *Madsen* (1974) and Velocity Record Obtained from (100) 115

Figure 40 – Average Surficial Transport of First Wave Cycle Passed Over a Smoothed Bed... 124

Figure 41 - Average Surficial Transport of Second Wave Cycle Passed Over a Smoothed Bed125

Figure 42 - Average Surficial Transport of Third Wave Cycle Passed Over a Smoothed Bed.. 125

Figure 43 – TWB Ensemble-Averaged Velocity Record with Integrated Sections 128

Figure 44 – TWB Theoretical Subsurface Transport..... 129

Figure 45 – Three Measurements of Experimental Surficial Transport Beneath the TWB 131

Figure 46 – Average Experimental Surficial Transport Beneath the TWB 131

Figure 47 – 02/07/06 Solitary Wave Displacements using c=190 cm/sec 135

Figure 48 – 06/06/06 Solitary Wave Displacements using c=190 cm/sec 135

Figure 49 – 06/22/06 Solitary Wave Displacements using c=190 cm/sec 136

Figure 50 – 06/25/06 Theoretical Solitary Wave Displacements using c=190 cm/sec 136

Figure 51 – Solitary Wave Average Displacements using c=190 cm/sec 138

Figure 52 – Solitary Wave Average Displacements using c=180 cm/sec 139

Figure 53 – Solitary Wave Average Displacements using c=160 cm/sec 139

Figure 54 – Solitary Wave Average Displacements using c=140 cm/sec 140

Figure 55 – Experimental Maximum Depth of Movement (Solitary Wave) 141

Figure 56 –Experimental Depth-Integrated Forward Excursion (Solitary Wave) 143

Figure 57 –Experimental Depth-Integrated Forward Excursion (Solitary Wave) 143

Figure 58 – Cumulative Net Subsurface Transport (Solitary Wave) 145

Figure 59 – Sensitivity of Theoretical Maximum Depth of Displacement to $(\rho_t - \rho)$, c, and ϕ 147

Figure 60 – Sensitivity of Theoretical Depth-Integrated Displacement to $(\rho_t - \rho)$, c, and ϕ .. 148

Figure 61 – TWB Displacements with PVC Beads using c=140 cm/sec 149

Figure 62 – TWB Displacements with PVC Beads using c=150 cm/sec 150

Figure 63 – TWB Displacements with PVC Beads using c=165 cm/sec 150

Figure 64 – Experimental Maximum Depth of Movement (TWB) with PVC Beads 152

Figure 65 –Experimental Depth-Integrated Forward Excursion (TWB) with PVC Beads 153

Figure 66 – Experimental Depth-Integrated Cumulative Displacements (TWB) with PVC Beads 153
Figure 67 – TWB Displacements with PET Beads using c=140 cm/sec 154
Figure 68 – TWB Displacements with PET Beads using c=150 cm/sec 155
Figure 69 – TWB Displacements with PET Beads using c=165 cm/sec 155
Figure 70 – Experimental Maximum Depth of Movement (TWB) with PET Beads 158
Figure 71 –Experimental Depth-Integrated Forward Excursion (TWB) with PET Beads 158
Figure 72 – Experimental Depth-Integrated Cumulative Displacements (TWB) with PVC Beads 159
Figure 73 – Dependency of Prototype Surficial Transport on *Lr* 162
Figure 74 – Dependency of Prototype Slip Circle Length on *Lr* 166
Figure 75 – Dependency of Prototype Maximum Depth of Movement on *Lr* 166
Figure 76 – Dependency of Prototype *As* on *Lr* 167
Figure 77 – Prototype Subsurface Displacements Scaled by *Lr* 167
Figure 78 – Difference Between Model and Possible Field Subsurface Sediment Movements 172
Figure 79 – Subsurface Deflections on a Slope 179

LIST OF TABLES

Table 1 - Density and Porosity of Clear PET Beads 40

Table 2 - Density and Porosity of Colored PET Beads 40

Table 3 - Density and Porosity of PVC Beads 40

Table 4 – Tabulated Size Distribution of PET Beads 41

Table 5 – Internal Angle of Friction for PET Beads 43

Table 6 – Internal Angle of Friction for PVC Beads 44

Table 7 – Experimentally Measured Three Wave Burst Phase Velocities 117

Table 8 – Experimentally Measured Three Wave Heights 118

Table 9 – Experimental Phase Velocity for Solitary Wave 120

Table 10 – Experimental Wave Heights for Solitary Wave 120

Table 11 – Surficial Sediment Transport Using Method 1 (Solitary Wave) 121

Table 12 – Surficial Sediment Transport Using Method 2 (Solitary Wave) 122

Table 13 – Bead Excursion Lengths (Solitary Wave) 123

Table 14 – TWB Amplitudes and Wave Friction Factors 128

Table 15 – Colored Sediment Column Characteristics – Solitary Wave 133

Table 16 – Model and Prototype Wave Parameters 160

Table 17 – Theoretical Surficial Transport for Prototype Wave 160

Table 18 – Theoretical Subsurface Transport for Prototype Wave 165

1 - INTRODUCTION

1.1 MOTIVATION

Understanding the mechanisms that transport sediment in coastal environments is of essential importance. The most obvious impact of coastal sediment transport in the near-shore environment is the erosion of beaches and shorelines. Shoreline erosion is widespread; it occurs on much of our nation's coasts. It has been estimated that 86% of California's coastline is in a state of active erosion (*Northcutt*, 2001). On the eastern coast, the Atlantic's coastline erodes at an average rate of about 2-3 feet per year. The states that are most affected are those along the Gulf of Mexico, with an average of six or more feet of beach lost per year. In fact, a single, major hurricane is capable of washing 100 feet or more of shoreline out to sea in a single day, demolishing any structures that are near the shoreline (*John Heinz III Center*, 2000) Overall, shoreline erosion is the cause of roughly half a billion dollars of losses to landowners per year. This figure includes both physical property loss and damage to structures built along the coast. To combat this threat, the federal government spends about $150 million dollars a year on shoreline erosion control measures and replacing eroded sands on beaches (*Sea Grant*, 2005).

The net erosion of shorelines is not solely a natural event. Society has increased the rates of shoreline erosion by several means. First, the damming of rivers prevents sediments from advecting downstream into coastal areas to replenish beaches. The dams precipitate out sediments in their reservoirs, trapping them upstream. In Southern California, it is estimated that dams prevent four million cubic meters of sediments per year from reaching the shore. For the

coastlines of the five Southern California counties, this is equivalent to three cubic meters of sand per linear foot of shoreline every year (*Sherman*, 2002). In addition, river channelization, the dredging of rivers, and levees all reduce the amount of sand that reaches the shore (*Northcutt,* 2001) (*The Resources Agency of California*, 1995).

The greatest cause of shoreline erosion is likely sea-level rise (*Pilkey and Cooper*, 2004 and *Day*, 2004). Pilkey and Cooper's article states, "In general, the world's shorelines would not be in a ubiquitous state of erosion without sea-level rise." Currently, sea level rise is accelerating; most likely due to increasing CO_2 levels that lead to global warming. It was found that, without intervention, sea level rise will cause a lateral shoreline erosion two orders of magnitude greater than the height of the rise (*Zhang et.al.,* 2004). This translates to a meter of shoreline lost for every centimeter of sea-level rise.

1.2 OVERVIEW

Understanding the physical processes that lead to shoreline erosion and accretion will allow us to make accurate predictions of how our shorelines will change over time. This knowledge will allow us to make intelligent decisions on what types of treatment will be necessary to maintain a particular stretch of coastline. Classically, there are two modes by which sediment is moved, bedload transport and suspended transport. Bedload transport is characterized by sediment particles rolling and tumbling along the sediment-water interface. Suspended transport is characterized by the entrainment of sediment particles into the water column. The entrained particles advect with the fluid and are deposited in locations that have more quiescent conditions. Suspended transport usually occurs when smaller sediment grain sizes are present as they are

more likely to be entrained. Bedload transport typically occurs with larger, denser sediment grains.

This study investigates a possible third sediment transport mechanism. This mechanism has the potential to transport sediment in a shorenormal direction under forward-leaning, asymmetric waves which are typical of the surf zone. A soil mechanics type failure induced by the overhead waves allows sediment particles to advect without rising above the sediment-water interface. Suspended and bedload transport can move sediment concurrently with this "subsurface" transport.

A goal of this study is to determine the relative importance of subsurface transport by comparing it to the classical "surficial" sediment transport mechanisms (suspended and bedload transport). To achieve this goal the following steps are taken:

- Experimental measurements are made of both surficial and subsurface transport using a laboratory wave flume that passes breaking or broken waves over a bed of lightweight plastic beads.
- A predictive theoretical model of the subsurface transport is developed that captures the mechanics of sediment movement beneath the water-sediment interface during the passage of a forward-leaning wave.
- An existing theoretical model is used to estimate the bedload transport induced in the experimental setup.
- Experimental data are used to verify and confirm the applicability of both theoretical models for forward leaning waves.
- Wave data from the laboratory are scaled up to conditions typical of waves found in the field.

- Using the predictive theoretical models for bedload and subsurface transport with the scaled wave parameters as input, the transport quantities are determined for sediment typical of that found in the field.
- By comparing the subsurface and bedload transport quantities for a variety of wave and sediment conditions, the relative importance of the subsurface transport in relation to surficial transport is assessed.

Shoreline erosion is a serious problem along our nation's coasts, precipitating negative economic consequences and potentially negative environmental circumstances. Although shoreline erosion occurs naturally, humans have had a detrimental effect on the stability of our coasts, hastening the recession of many of our shorelines. The research described in this thesis will increase understanding of the processes that contribute to coastal sediment transport.

2 - LITERATURE REVIEW

To understand coastal sediment transport in the surf zone, we must first understand the waves which drive the concerned processes. Ocean waves create an orbital velocity in the water column as they propagate. As a wave crest passes overhead, a shoreward velocity is sustained; whereas, a seaward velocity is generated during the passage of a wave trough. In deeper waters, the waves are nearly linear; that is, their water surface levels and velocity records can be accurately be described by a sinusoidal function. A linear wave produces shorewards and seawards velocity records that only differ in direction. If averaged over complete wave periods, the total, net sediment transport from a perfectly linear wave is zero. However, nonlinear effects, such as wave asymmetry, skewness, mass-transport currents, and topography, all produce a net transport of sediment (*Foda*, 2003). Typically, sediment moves offshore during storm events because of strong offshore currents that develop during periods of large wave heights. This offshore transport is balanced by onshore transport during calm conditions. The onshore transport is typically of lower intensity but occurs for longer intervals of time. This study focuses on onshore transport that dominates during periods of small wave heights.

As waves propagate into shallower depths, the crests become taller and forward leaning, as they begin to feel the bottom. These characteristics are termed positive wave skewness and positive wave asymmetry, respectively. Positive skewness is characterized by long, shallow troughs and narrow, tall peaks. Positive wave asymmetry is characterized by crests with a steep front face and a gently sloping back face. Positive skewness leads to shore-directed velocities that are substantially greater in magnitude but shorter in duration than the seaward velocities. Positive wave asymmetry leads to a large onshore acceleration during passage of the forward leaning part

of the crest and a smaller magnitude of seaward acceleration after passage of the crest (*Hoefel and Elgar*, 2003).

For most of the water column the fluid velocity can be well approximated using potential theory which neglects the effects of fluid viscosity. However, in order to accurately model a velocity of zero along the sediment-water interface, we must consider a region in which viscous effects are no longer negligible. This region of large velocity spatial gradients is known as the wave bottom boundary layer. The formation of boundary layers is induced by wave orbital velocities during both the shoreward (positive) and seaward (negative) excursions of the fluid. Boundary layers increase in thickness over time as a fluid velocities are sustained in a single direction (Schlichting, 1955). As the horizontal component of a wave's orbital velocity passes through zero, the boundary layer that developed for the previous velocity direction is no longer relevant. After the change in velocity direction, a new boundary layer is formed and begins to grow in thickness. At any given moment, the shear stress exerted on the bottom is inversely proportional to the instantaneous boundary layer thickness and proportional to the square of the instantaneous bottom velocity.

Both positive wave asymmetry and positive wave skewness induce a net onshore transport. In an asymmetric wave there is an acceleration of large magnitude up to the maximum positive horizontal velocity, u_{bm}, and a smaller magnitude deceleration of the fluid after u_{bm}. The large magnitude acceleration during the velocity rise allows the boundary layer less time to develop yielding an increased bottom shear stress under the steep front face of the crest. In skewed waves, the peaked velocity record leads to larger magnitude accelerations and decelerations on the leading and trailing sides of the wave crest, also yielding a thin bottom boundary layer under

the crest. The disparity in the shoreward and seaward associated bottom boundary layer thicknesses yields larger bottom shear stresses under the crest compared to the bottom shear stresses beneath the troughs. Since the instantaneous surficial transport vector is proportional to a power greater than one of the instantaneous bottom shear stress vector, the skewed, asymmetric waves yield higher rates of instantaneous transport during the shoreward fluid movements. The effect of wave asymmetry and skewness on surficial transport is explained in quantitative terms in Section 4.2.2.

In addition to shoreward surficial transport, the peaked, forward leaning waves present in the surf zone can potentially create subsurface transport. Considering only hydrostatic forces, it can easily be seen that the steep front face of a breaking wave generates a significant horizontal pressure gradient. The magnitude of the pressure gradient is highly correlated with the magnitude of the fluid accelerations. *Madsen* (1974) observed these pressure gradients can induce a significant porous media-type flow within the sediment pore space. The intergranular flow within the sediment bed exerts a seepage force on the sediment grains, potentially creating a momentary failure within the sediment bed. Calculation of seepage forces are routine in geotechnical engineering and are often encountered when considering the stability of earthen dams. The seepage force, F_s, is negatively correlated to the pressure gradient, Δp.

$$F_s = -\Delta p \tag{1}$$

To determine the depth to which a failure can occur, *Madsen* neglected the unsteadiness of the problem and used a soil mechanics approach. The strength of an uncohesive sediment in the x-direction (horizontal) can be determined from the a soil element's normal effective stress and the sediment's angle of internal friction, ϕ. The effective stress is defined as the sum of the vertical forces carried by the sediment particles at their points of contact per unit of cross-sectional area.

The internal angle of friction relates the normal effective stress to the amount of intergranular horizontal friction shear stress that can be mobilized. The internal angle of friction is equivalent to the angle of repose and can be measured using the direct shear test.

The critical horizontal pressure gradient, $\left(\frac{\partial p}{\partial x}\right)_{cr}$, that induces a seepage force equivalent to the intergranular horizontal frictional force, can be expressed as:

$$-(F_s)_{cr} = \left(\frac{\partial p}{\partial x}\right)_{cr} = (\rho_t - \rho) g \tan(\phi) \tag{2}$$

with:

$$\rho_t = (1-n)\rho_s + n\rho \tag{3}$$

where $(F_s)_{cr}$ is the critical horizontal seepage force, g is gravity, ρ_t is saturated bed density, and n is porosity (*Madsen*, 1974). If the critical pressure gradient is exceeded, the seepage forces will be greater than the soil's strength, creating a temporary failure in the sediment bed. A vertical pressure gradient is also generated by the breaking wave but its magnitude is unlikely to affect the stability of the sediment bed (*Madsen*, 1974).

To obtain a estimate of the depth of the failure, $\delta_{\max}$, *Madsen* considered a limiting slip circle whose length, $\ell_{s\,\max}$, is the horizontal distance over which a failure, defined by (2), occurs. The depth of the failure is found by equating the moment generated by the wave's pressure forces, M_d, to the moment generated by the frictional forces acting along the slip circle's failure plane, M_s. Both moments act about the slip circle's axis of rotation *C*. Figure 1 shows *Madsen's* limiting slip circle; the failure plane is along the slip circle's curved bottom.

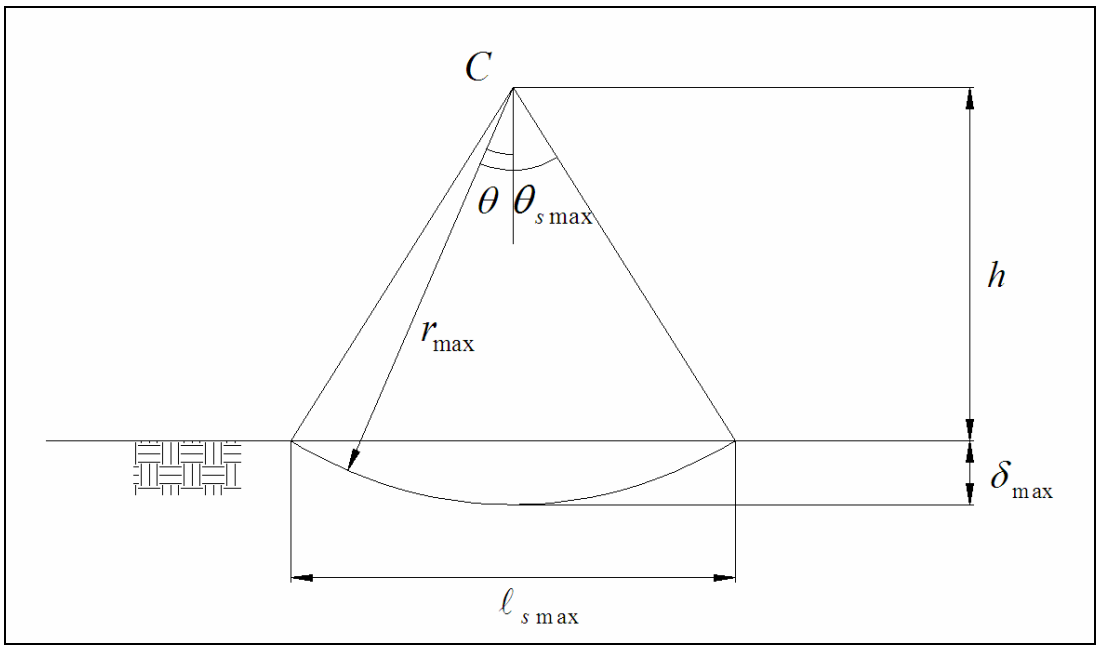

Figure 1 - Limiting Slip Circle Notation

Madsen (1974) assumed a linear pressure distribution over the horizontal extent of the failure, $\ell_{s\max}$. The average slope of the pressure distribution, $\langle\alpha\rangle$, is given as:

$$\langle\alpha\rangle = \frac{1}{\rho g}\left\langle\frac{\partial p}{\partial x}\right\rangle_{\ell s\max} \tag{4}$$

where the brackets denote averaging over $\ell_{s\max}$. The moment generated by the linearly varying pressure distribution about *C* is determined by:

$$Md_{\max} = \frac{2}{3}\rho g\alpha {r_{\max}}^3 \sin^3\theta_{s\max} \tag{5}$$

The effective normal stress, σ'_n, that acts along the slip circle's failure plane is:

$$\sigma'_n = \frac{p - p_p}{1-\tan\phi\tan\theta} + \frac{g(\rho_t - \rho)r(\cos\theta - \cos\theta_{s\max})}{1-\tan\phi\tan\theta} \tag{6}$$

where p_p is the pore pressure and p is the pressure on the bottom. Both pressures are defined as the deviations from the average hydrostatic pressure. The pore pressure is essentially the pressure of the fluid within the sediment bed's interstitial pore space. The wave-induced pore pressure has an

exponential decay as the depth beneath the sediment-water interface is increased. This decay is scaled by the wavelength of the wave passing overhead. The maximum stabilizing frictional moment that can be mobilized can be expressed in terms of the effective normal stress.

$$Ms = \int_{-\theta_{s\max}}^{\theta_{s\max}} \sigma'_n \tan\phi r^2 d\theta \tag{7}$$

To obtain a solution for Ms, *Madsen* (1974) reasoned that $p - p_p$ is a small quantity if the slip circle is assumed to only extend a short depth into the sediment bed relative to the wave's length. Additionally, with the assumption of a linear bottom pressure distribution, $p - p_p$ is antisymmetric about C, yielding no moment. With the neglect of the first term of (6), the integration in equation (7) can be performed to give:

$$Ms = 2g(\rho_t - \rho)\tan\phi r^3 \sin\theta_{s\max}(1 - \theta_{s\max}\cot\theta_{s\max}) \tag{8}$$

The angle, $\theta_{s\max}$, is determined by equating the driving moment to the stabilizing moment to yield the following. Iteration is required.

$$\frac{\sin^2\theta_{s\max}}{1 - \theta_{s\max}\cot\theta_{s\max}} = 3\frac{\rho_t - \rho}{\rho}\frac{\tan\phi}{\alpha} \tag{9}$$

The radius of the slip circle is given by:

$$r_{\max} = \frac{\ell_{s\max}}{2\sin\theta_{s\max}} \tag{10}$$

With $\theta_{s\max}$ and $\ell_{s\max}$ the maximum depth of disturbance, $\delta_{\max}$, can be obtained from:

$$\delta_{\max} = \ell_{s\max}\frac{1 - \cos\theta_{s\max}}{2\sin\theta_{s\max}} \tag{11}$$

Madsen (1974) performed laboratory experiments in a wave flume to determine the magnitude of the pressure gradient induced by a breaking wave. Pressure taps were installed 1.7cm apart in a 1:10 beach built into the wave flume. A differential pressure transducer was connected to these pressure

taps. It was found that a spilling breaking wave could produce a maximum pressure gradient of $\alpha_{\max} = \frac{1}{\rho g}\left(\frac{\partial p}{\partial x}\right) = 0.71$ (no averaging) whereas a plunging breaking wave is capable of producing an maximum pressure gradient of $\alpha_{\max} = 0.65$. For relatively loose sand, the critical pressure gradient was found to be approximately:

$$\alpha_{cr} = \frac{1}{\rho g}\left(\frac{\partial p}{\partial x}\right)_{cr} = 0.50 \tag{12}$$

Averaged over the failure length, $\ell_{s\max}$, *Madsen* found that the pressure gradient was $\langle \alpha \rangle = 0.64$ and 0.60 for spilling and plunging breakers, respectively. Thus, a breaking wave of sufficient steepness has the ability to create a failure within a sandy sediment bed. It was determined that a spilling breaker was capable of producing a maximum disturbance depth of:

$$\delta_{\max} = 0.22\ell_s \simeq 0.11H_b \tag{13}$$

where H_b is the wave height at breaking. *Madsen* explained that during the momentary failure sediment particles slide past one another, moving grains from their initial position. This "shuffling" of grains could explain why tracer particles that initially are placed on the sediment-water interface have been found by researchers to later be buried several centimeters into the sediment bed. *Madsen* found that the relationship given by (13) matches the order of magnitude of the burial depths measured by *Komar and Inman* (1970).

As for subsurface transport induced by this pressure gradient, *Madsen* (1974) noted that the momentary failure creates a "slight motion" of the sediment above the limiting slip circle as each wave passes overhead, however, no estimates of the magnitude of the movement of the subsurface grains are given.

The impetus of *Madsen* (1974) was observations of divers that witnessed an "explosion" on the ocean floor just before a wave crest passed overhead. No such observations were made underneath the wave trough. The mechanism behind these "explosions" was suspected to be because of the flow through the porous bed. A field study of the movements of the fluidized upper sediment layer under near-breaking waves by *Conley and Inman* (1992) found similar conditions. Three distinct regimes of sediment movement were identified under a breaking wave: streaking, roiling, and pluming. The first regime, streaking, occurs when strength of the sediment bed in exceeded by a small margin. The sand particles begin rolling and tumbling along the sediment-water interface, in a manner consistent with bedload transport. Small streaks of moving sand particles develop in weak areas of the bed and are on the order of 10cm long. The second regime, roiling, occurs under more vigorous conditions and is characterized by the movement of the entire sediment surface. Small "tufts" of fluidized sediment form, making a three-dimensional surface. The moving sediment layer extends roughly 1.6cm above the stationary sediment bed. This regime is otherwise known as to sheet flow. The last regime, pluming, occurs just after the wave crest passes overhead and the fluid begins to decelerate. The roiling layer ejects the sediment into the water column to a height approximately five to ten times the height of the roiling layer. The sediment particles then move with the fluid and eventually settle down to the bottom. Pluming is likely the regime noted by *Madsen* (1974).

Although the *Conley and Inman* (1992) study provides observations of different types of sediment movements under highly asymmetric waves, it is important to note that each of the three regimes cannot be classified as subsurface transport. In the failure mechanism noted by *Madsen* (1974), the portion of the sediment bed above the maximum depth of displacement is in failure but sediment grains do not roll along the bottom of the bed nor do they become entrained into the water column. Field observations of subsurface transport are likely to encounter significant difficulties in tracking

the movements of marked sediment particles embedded within the bed. The author is not aware of any experimental or field observations of sediment transport that occurs under a soil-mechanics type failure. However, many studies present findings that show that fluid acceleration can enhance or dominate surficial sediment transport.

Sleath (1999), *Flores and Sleath* (1998), and *Dick and Sleath* (1991) present an experimental and theoretical examination of sediment transport induced by a pressure gradient. The study observes the velocities and concentrations of the top layer of sediment that moves back and forth horizontally with the fluid in a wave tunnel. The wave tunnel used in these experiments is essentially a U-shaped tube in which a sinusoidal-varying velocity is generated via a piston. The effect of wave acceleration is found on sediment beds comprised of either nylon or acrylic beads in *Dick and Sleath* (1991) and of sand, acrylic, or PVC in *Flores and Sleath* (1998). The observed sediment movement can occur ~10cm beneath the sediment-water interface and can sometimes achieve a "plug" type flow in which the upper sediment layer moves uniformly as a block (*Sleath,* 1999). In these experiments the mobile sediment shows a decrease in sediment concentration after initiation of motion. The nearly sinusoidal velocities in these experiments do not create a failure as theorized by *Madsen* (1974). The transport mechanism described by *Sleath* (1999), *Flores and Sleath* (1998), and *Dick and Sleath* (1991) is characterized as sheetflow. However, *Sleath* (1999) notes that if the sediment bed experiences no dilation, an analysis of sediment bed stability similar to that given by *Madsen* (1974) can be used to determine a minimum threshold that must be exceeded before sediment "plugs" can form.

In many recent papers (*Thornton et. al.* (1996), *Gallagher et. al.* (1998), and *Hoefel and Elgar*, (2003)) sandbar movement has been modeled numerically with different methodologies and

schemes. As the sandbar movements are easily discernable, modeling their movements allow researchers a straightforward way to verify/compare model predictions of cross-shore transport with field observations. Some researchers agree that skewness or/and asymmetry of waves in the surfzone are responsible for the shoreward migration of sandbars during calm, non-storm conditions (*Hoefel and Elgar*, 2003) and (*Drake and Calantoni,* 2001). However, these effects are dominated during stormy periods by a large, seaward current (undertow) which causes seaward sandbar movement. Modeling onshore sediment transport during calm conditions has proven to be much more difficult than modeling offshore sediment transport in stormy conditions. The models of *Thornton et. al.* (1996) and *Gallagher et. al.* (1998), accurately estimated seaward sandbar movements but failed to accurately model onshore movements. Both studies, however, did not consider the enhanced shear stress that occurs underneath wave crests.

Drake and Calantoni (2001) developed a computer simulation that estimated sheet flow regime sediment transport created by a pressure gradient. Their model is complex; it incorporates many more intergranular processes than the theoretical model of *Madsen* (1974). It was found that once a critical pressure gradient was exceeded, pressure gradient driven transport would contribute significantly to overall transport. *Drake and Calantoni* (2001) found that this mechanism can be characterized by a single acceleration term that is adjusted to field data and noted that it should be included in numerical simulations of sandbar movement.

Hoefel and Elgar (2003) adopted *Drake and Calantoni's* acceleration term in their model of cross-shore transport, calibrating it for their field conditions. By including the pressure gradient driven transport in their model, they were able to accurately predict both seaward and shoreward sandbar movements. It is suspected that although the model of *Hoefel and Elgar* (2003)

incorporated a term for pressure-induced transport developed for sheetflow, their acceleration term could include subsurface transport which is driven by the same type of forcings. Since the coefficients of the acceleration term are calibrated to yield the best fit to field data as opposed to being derived mechanistically, the ratio of subsurface to sheetflow shoreward transport actually occurring in the field is not known. This study seeks a method by which mechanistic determinations of subsurface transport can be made.

3 - EXPERIMENTAL SETUP AND INSTRUMENTATION

Experiments were conducted in the Ralph M. Parsons Laboratory for Water Resources and Hydrodynamics at the Massachusetts Institute of Technology. The 28m long, 76cm wide wave flume located in the J. Robert Gunter Environmental Fluid Mechanics Laboratory was utilized for this study.

3.1 WAVE FLUME

The wave flume is outfitted with a hydraulically-operated piston-type wavemaker. Large rectangular basins are present on either end of the flume, up-wave of the wavemaker and down-wave of a permanent 1:10 beach. The flume has capability to generate currents within the flume; however, no currents are used in the present study. Figure 2 shows a schematic view of the wave flume.

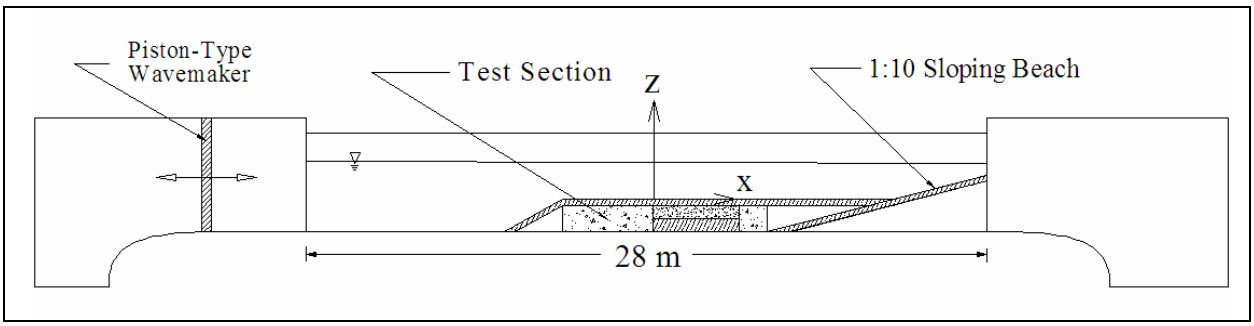

Figure 2 – Schematic View of Wave Flume

The rectangular flume's sidewalls are constructed of 1/2" thick glass panels permitting direct observation of the flume contents in the lateral direction. Additionally, the bottom of the wave flume is constructed of the same glass panels with the exception of the first 3 and the last 12 meters which are constructed of steel. Care must be taken not to damage the glass bottom while moving heavy objects into and out of the flume.

For clarification, throughout this document “longitudinal” will refer to the x-direction as shown in Figure 2, while “lateral” will refer to the y-direction that extends in and out of the page. A right-handed coordinate system is used in this study; positive y-direction is into the plane of Figure 2.

Along the top of the flume sidewalls two tubular rails are mounted to allow a carriage to roll longitudinally the length of the flume. This carriage provides a platform onto which instruments can be mounted. (see section 3.5)

3.2 TEST SECTION

A false-bottom test section was installed in the wave flume. The test section consists of a ramp that extends down to the glass flume bottom and a constant depth portion that ties into the permanent 1:10 beach. Depending on the length of ramp used, the test section begins approximately 16 meters into the wave flume. The test section was designed to allow the insertion of a transparent Plexiglas tray containing granulated material into the false bottom and to allow the material to be photographed through the glass side walls. The test section contains twelve 8” concrete blocks sandwiched between ¾” pressure-treated plywood. The considerable heft of the concrete blocks is necessary to prevent movement of the test section under wave action. Additionally, rubber matting was used underneath the test section to provide protection against sliding.

Because the wave flume is not capable of generating wave heights typical of those found in the field, plastic beads are used to model non-cohesive sediment (sand). The plastic beads' lower density (compared to quartz) permits larger magnitudes of surficial and subsurface transport, allowing easier quantification. A 10.6 cm-wide, 12.3 cm-deep, and 1.03-m long (inside dimensions) Plexiglas tray was constructed to contain the granulated plastic beads. The Plexiglas tray is securely bolted to the test section to ensure that the box is not jostled as the wave passes overhead.

Since a tray of finite size is used to model sediment transport in the surfzone (where dimensions are not constrained), the tray's effect must be considered. To prevent the plastic beads from moving as a cohesive unit along the smooth interior of the tray, a thin layer of beads glued to rigid plastic sheeting is used to line the bottom of the tray before it is filled with loose beads. In early experiments without the rough bottom, the sediment bed merely slid as a unit down wave without undergoing deformation. The roughened bottom provides sufficient friction to anchor the beads in place, allowing a failure in the bed to occur. For the wave conditions used in this study, bead movement never extended down to the bottom of the tray when a roughened bottom was used.

The wave flume produces waves that are laterally uniform, which translates to a near lateral uniformity in the subsurface transport. Since there are no differences in the subsurface sediment movement in the lateral direction, there are no intergranular stresses in the sediment bed along longitudinal planes. To most accurately represent a sediment bed of infinite lateral extent, the tray's side walls remain smooth to decrease the friction along the Plexiglas/bead interface as

much as possible. The lateral uniformity of the subsurface sediment movement is discussed in section 4.1.1.

It is assumed that the tray's 1m length does not create interference with the beads' subsurface movement in the center of the tray. The tray's finite length affects surficial sediment transport, which is further explained in section 4.1.2.

The tray's edges extend two centimeters above the false bottom (and the initial sediment level) to provide support for a strip of petticoat gauze that is draped over the top of the tray. The gauze prevents the plastic beads from escaping the tray in a lateral direction during wave agitation. The tray's raised edges prevent the gauze from contacting the beads and thereby inhibiting its movement. The gauze is securely fastened using thumbtacks to the plywood surrounding the tray.

Gauze sediment collection bags are affixed to the upstream and downstream ends of the sediment box to collect beads that spill over the ends of the box as a wave passes overhead. The sediment collected in these bags is used as a boundary condition in the calculation of sediment transport rates (further explained in section 4.1.2). The bags' openings surround a Plexiglas sleeve which is attached to the tray using Velcro. The rigid Plexiglas sleeve holds the mouth of the bag open to ensure free movement of the beads into the bags.

Figure 3 and Figure 4 show schematic drawings of the experimental test section. All dimensions are in centimeters. The location of the section view presented in Figure 4 is shown in Figure 3.

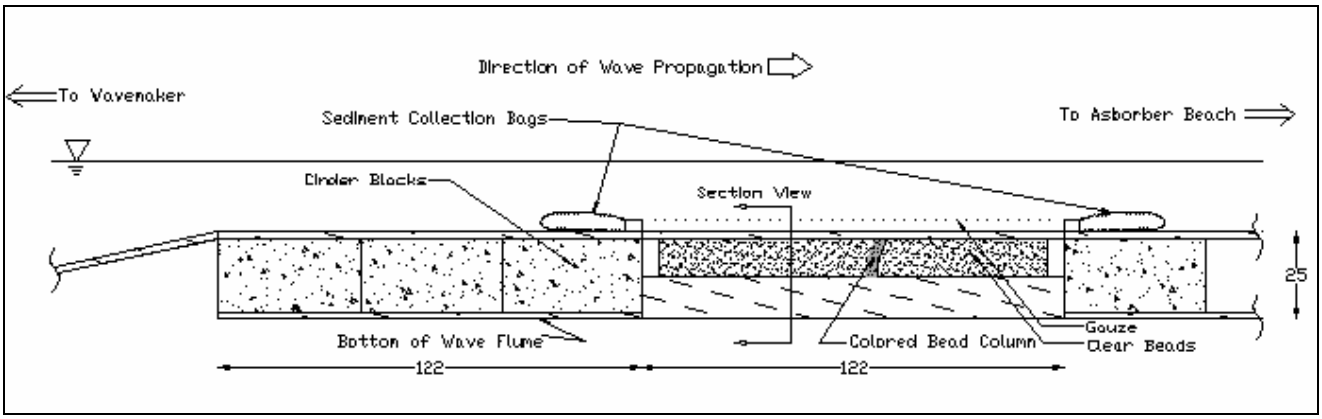

Figure 3 – Side View of the Experimental Test Section

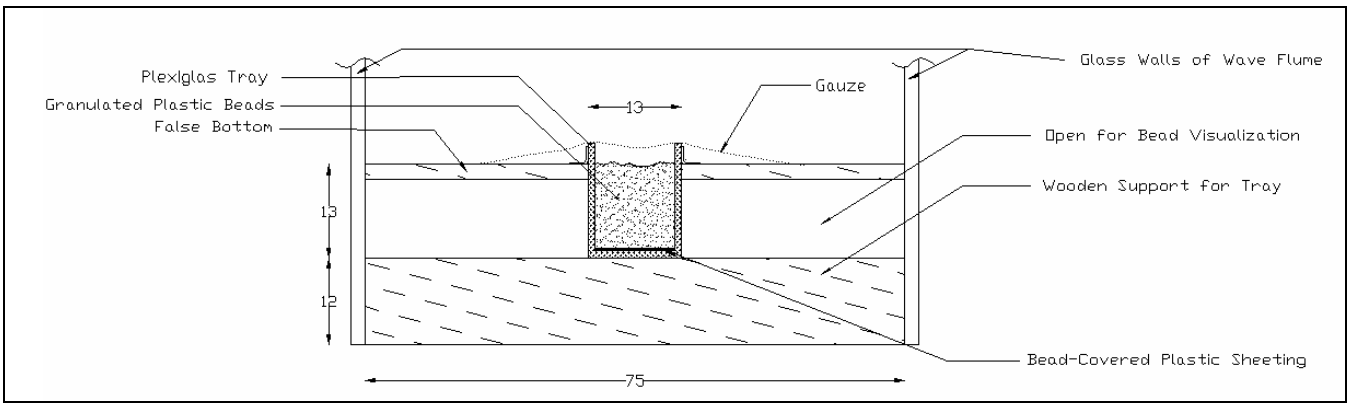

Figure 4 – Section View of the Experimental Test Section

Subsurface sediment movement is measured by inserting a column of colored plastic beads across the entire width of the tray into a bed of clear beads. With the exception of color, the colored and clear beads have nearly identical properties. The colored column's movement, and hence the subsurface sediment movement, can be observed through both glass sidewalls of the wave flume. The colored column is inserted into the sediment bed using a custom-made injector. The injector clamps to the sediment tray and holds two Plexiglas sheets perpendicular to the longitudinal axis of the sediment tray. Additionally, the sheets are kept vertical and parallel to

one another. The injector allows the Plexiglas sheets to slide vertically while maintaining their orientation.

To obtain a uniform column of colored beads, the following steps are used. First, the injector is clamped to the walls of the tray. Next, Plexiglas sheets are slid into the injector, creating a seal along the bottom and sides of the tray that partitions off a section for the colored beads. The beads, colored and clear, are separately prepared by fully submerging them for 15-20 minutes in a mixture of Windex (an emulsifying agent) and water. While submerged, the beads are thoroughly stirred and mixed. This process removes air bubbles, which can lead to cohesion in the sediment bed and buoyant beads that float to the surface. The colored bead emulsion is poured between the two parallel Plexiglas sheets. Next, the clear bead emulsion is poured into the sections up- and downstream of the colored column. The Plexiglas dividers are then slowly removed one at a time, leaving a uniform column of colored beads with clear beads to either side. On the outside of the box, lines marking the initial position of the colored-clear bead interfaces are drawn with a waterproof marker. The tray is then lowered into the false bottom and fastened. Much care must be used while lowering the box into the false bottom as a slight jostle can dislocate the colored-clear bead interface. The flume is then filled with water. The tray is watertight; the beads are saturated continuously from the time that they are first mixed with the water/Windex solution.

The tray is filled with beads such that the sediment water interface is level with the top of the plywood sheeting (false bottom) on either side of the tray. This creates a nearly uniform initial bottom elevation in the lateral direction across the top of the test section. Because the sediment

level is even with the top of the plywood, the top two centimeters of the colored column cannot be visualized through the glass sidewalls.

Flow interference created by the longitudinal vertical edges of the sediment tray that extend above the false bottom is assumed to be negligible. A tight-fitting cap is applied over the sediment tray while filling the wave flume with water to prevent erosion of the plastic beads.

3.3 BEAD PROPERTIES

Two types of beads were used in this study. Initially, beads made from polyvinyl chloride (PVC) were used to conduct experiments. These beads had less than satisfactory characteristics, as after being submersed in water for ~1-2 hours they turned opaque and potentially became cohesive. The manufacturer, Ronald Mark Associates, said this is likely due to plasticizer leaching out from the beads during submersion. They recommended using Polyethylene Terephthalate (PET) beads, as they have no plasticizer and are commonly used in wet environments. The properties of both types of beads are given in the following sections.

3.3.1 Bead Density and Porosity

Samples of PET and PVC beads were analyzed to determine their respective densities. A graduated cylinder was used to measure a volume (~100mL) of dry plastic beads. The dry mass, M_{dry}, of the beads was recorded. Next, a solution of Windex and water was mixed with the beads and agitated to remove any air bubbles. During mixing, the beads are suspended in the solution; after settling back down to the bottom of the cylinder they appear to be uncompacted and loose. To maintain a uniform level of compaction, the beads were tamped lightly with a

dowel to settle them slightly. In addition, the graduated cylinder is tapped against the lab bench to remove any large voids in the pore space.

The excess water volume is defined as the volume of water above the bead-water interface in the graduated cylinder. The excess water is not inside the beads' pore spaces; it is the water overlying the bead-water mixture. The volume of the beads after the solution was added, V_b; excess water volume, V_e; and the total mass, M_t, is recorded. The total mass includes the excess water and the saturated beads. To determine the volume of the voids, V_v, equation (14) is used:

$$V_v = \frac{M_t - M_{dry}}{\rho} - V_e \tag{14}$$

where V_v is the volume of the pore space within the bead matrix and ρ is the density of water. The Windex's contribution to ρ will be considered negligible as the volume of Windex added to the graduated cylinder is much smaller than the volume of water. The density of the plastic material, ρ_s, is found using:

$$\rho_s = \frac{M_{dry}}{(V_b - V_{v)}} \tag{15}$$

and the porosity , n , is:

$$n = \frac{V_v}{V_b} \tag{16}$$

Bead characteristics obtained in this manner are presented in Table 1 and Table 2

Table 1 - Density and Porosity of Clear PET Beads

	ρ_s (g/cm^3)	n (cm^3/cm^3)
	1.252	0.384
	1.258	0.381
	1.248	0.395
	1.265	0.396
	1.263	0.356
	1.275	0.372
	1.265	0.353
Average	1.261	0.377
Std. Dev.	0.008	0.016

Table 2 - Density and Porosity of Colored PET Beads

	Blue Beads			Pink Beads	
	ρ_s (g/cm^3)	n (cm^3/cm^3)		ρ_s (g/cm^3)	n (cm^3/cm^3)
	1.282	0.350		1.267	0.362
	1.293	0.367		1.282	0.373
Average	1.288	0.359		1.274	0.368

The colored beads appear to have a slightly higher density, but this difference is assumed to be negligible. For the calculations presented in this study both the clear and colored PET beads were assumed to have a density of $\rho_s = 1.27$ g/cm^3 and a porosity of $n = 0.37$.

Table 3 shows the density and porosity of a blend (colored and clear) PVC beads.

Table 3 - Density and Porosity of PVC Beads

	ρ_s (g/cm^3)	n (cm^3/cm^3)
	1.228	0.385
	1.218	0.380
	1.208	0.383
	1.218	0.386
Average	1.218	0.384
Std. Dev.	0.008	0.003

Measurements of density and porosity were carried out on clear bead and colored PVC beads separately, but Windex was not used to remove air bubbles which lead to inaccurate results. A sample of clear PVC beads was not available after it was found that an emulsifier could release the air bubbles. The characteristics of the clear and colored beads are assumed to be approximately the same. A sediment density of ρ_s = 1.22 (g/cm^3) and porosity of n = 0.38 was used for the PVC beads for calculations in this study.

3.3.2 Bead Size

Both types of beads were sieved by the manufacturer and determined to between a 16 and 18 sieve size. This corresponds to a sieve diameter between 1 mm and 1.19 mm. To verify the manufacturer's specifications, the PET beads were sieved at MIT. Values are tabulated in Table 4.

Table 4 – Tabulated Size Distribution of PET Beads

Sieve No.	Opening Size (mm)	Cumulative Percent Finer (%)
12	1.7	-
14	1.41	99.4
18	1	5.20
20	0.85	1.10
25	0.71	0.177
Pan	0	0

The results appear to be consistent with the manufacturer's data with the exception of a small amount of fine particles. Since both types of beads have the same manufacturer size specification, a representative grain size of 1.1mm (nominal) will be used in the calculations in this study for both the PET and PVC beads.

3.3.3 Internal Angle of Friction of the Beads

To determine the internal angle of friction of the beads used in this study a device was constructed to tilt a bead sample until the angle of repose was reached. A diagram of this apparatus is shown in Figure 5. The device allows controllable rotation about a single axis and provides reliable angle measurement. The direct shear test, normally used by geotechnical engineers to ascertain the internal angle of friction, exerts a normal pressure much higher than the beads would experience under laboratory conditions. The large vertical pressure would likely crush the plastic beads and not provide results relevant to this study. In addition, the tilting method allows beads to be fully submerged while testing, the same condition the beads experience in the wave flume.

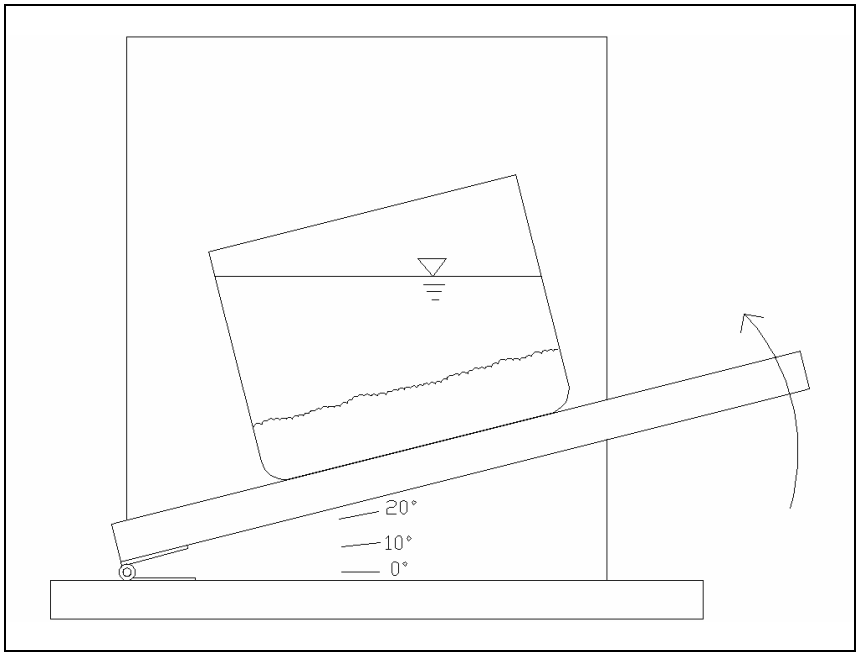

Figure 5 – Device Used to Measure the Internal Angle of Friction of the Plastic Beads

Beads were placed in a cylinder with an oblong, ellipsoidal shaped cross section for testing. The cylinder was tilted such that the long dimension of the cross section is aligned down the slope. This is necessary to minimize the cylinder sidewalls' stabilizing effect upon the beads. To determine the effect of vibration on the friction angle, the cylinder containing beads was placed

on a large, running belt sander for 10 seconds. A platform on the belt sander provided a convenient location to place the cylinder during vibration.

The sediment-water interface in the unvibrated cases was carefully smoothed with a small board. Without this smoothing the uneven surface yields large (~5-6 deg) standard deviations in the measurement of the friction angle. The sediment-water interface of the vibrated bead samples was leveled by the vibrations, no smoothing was needed.

Three different bead conditions were tested in both unvibrated and vibrated states. Beads were tested dry, recently submerged in a mixture of water and Windex, and submerged for some time in a water and Windex mixture. Both of the submerged case are vibrated immediately before testing. The long term bead submersion provides a metric to ascertain if the sediment bed gains strength after being immersed.

The following results were obtained for the PET beads.

Table 5 – Internal Angle of Friction for PET Beads

	Dry		Submerged		Submerged for Several Weeks	
	unvibrated	vibrated for 10 sec	unvibrated	vibrated for 10 sec	unvibrated	vibrated for 10 sec
Number Of Tests	20	20	20	10	20	20
Average	32.4	36.4	34.8	39.2	34.7	38.7
Std.Dev.	0.8	0.7	1.0	1.1	1.0	0.9

For the PVC beads the following was obtained. The test conditions were identical to that of the PET beads with the exception being that the long-term submersion sample was only immersed for three days in the mixture.

Table 6 – Internal Angle of Friction for PVC Beads

	Dry		Submerged		Submerged for 3 days	
	unvibrated	vibrated for 10 sec	unvibrated	vibrated for 10 sec	unvibrated	vibrated for 10 sec
Number Of Tests	20	20	20	20	20	20
Average	31.1	39.3	33.3	37.6	35.1	39.2
Std.Dev.	0.7	0.5	0.77	0.8	0.9	0.7

Theoretically, the angle of repose of an uncohesive, granular material should be the same whether the sample is submerged or dry. The PET beads show an increase in friction angle in both the unvibrated and vibrated cases when the beads are submerged. The unvibrated PVC beads show an increase in friction angle after submersion, whereas this trend is reversed in the vibrated case.

The PVC bed shows signs of strengthening after being submerged in the mixture for three days in both the vibrated and unvibrated states. Several hours after submersion the PVC beads turn from clear to opaque. It is suspected that this change in color is related to a physical process that gives the bed slightly cohesive properties. This cohesion leads to an increase in friction angle. The PET bed showed no strengthening after being submerged in the mixture for several weeks.

3.4 WAVE GENERATION

The programmable, hydraulically-actuated wavemaker used in this study drives a vertical paddle which moves uniformly in the longitudinal direction of the wave flume (see Figure 2). The hydraulic oil used to power the piston increases in temperature and expands as the wavemaker is operated. Therefore, the wavemaker must be turned on for approximately thirty minutes to allow the oil to reach a steady-state temperature before a repeatable wave can be produced, (*Carter,* 2002).

The wavemaker has the capability to be operated via an internal signal generator or by an external analog signal ranging from -10V to +10V. For maximum control, the wavemaker was operated externally. Analog signals are produced using a DOS-based PC and Keithley DAS-1600 digital to analog (D/A) conversion board. Custom software written in *Borland C/C++*, by *Carter* (2002), was used to generate the analog signals.

3.4.1 Three Wave Burst

Two different wave conditions were used in this study. The first condition was a three-wave burst. The software developed by *Carter* (2002) was used, unmodified, to produce this wave condition. The wavemaker motion was gradually transitioned from rest to pure sinusoidal motion and then gradually transitioned back to rest. Out of many different configurations, a period of T= 5.5 sec, a wave maker amplitude of a_p= 25 cm, a flume water depth of h= 45 cm (measured from glass bottom to water surface), and a ramp length of 122 cm (ramp inclination of 12º from horizontal) yielded the largest negative pressure gradient.

To a first approximation, the pressure gradient can be calculated with the momentum equation using:

$$\frac{\partial u}{\partial t} = -\frac{1}{\rho}\frac{\partial p}{\partial x} \tag{17}$$

Section 4.2.3 gives describes a method used to find the pressure gradient with greater accuracy.

Note: Throughout this study the pressure gradient is plotted as $-\frac{\partial p}{\partial x}$. Thus, a positive $\left(-\frac{\partial p}{\partial x}\right)$ quantity will yield a shoreward subsurface transport.

Each of the three waves broke near the middle of the test section. This wave condition will be referred to as the "three-wave burst" throughout this thesis. Figure 6a shows the ensemble average of ten smoothed realizations of velocity time series for this wave condition and the corresponding pressure gradient. Velocities were measured with the ADV probe positioned in the center of the box. (see section 3.5.2 for details about velocity measurement). See section 4.2.4.1 for more information about the smoothing. Figure 6b shows the ensemble-averaged velocity and pressure gradient records of the three-wave burst. The realizations are aligned using the first maximum velocity and maximum pressure gradient of the first wave. The average is shown as a solid line in blue. The standard deviation across the ten realizations is shown in red.

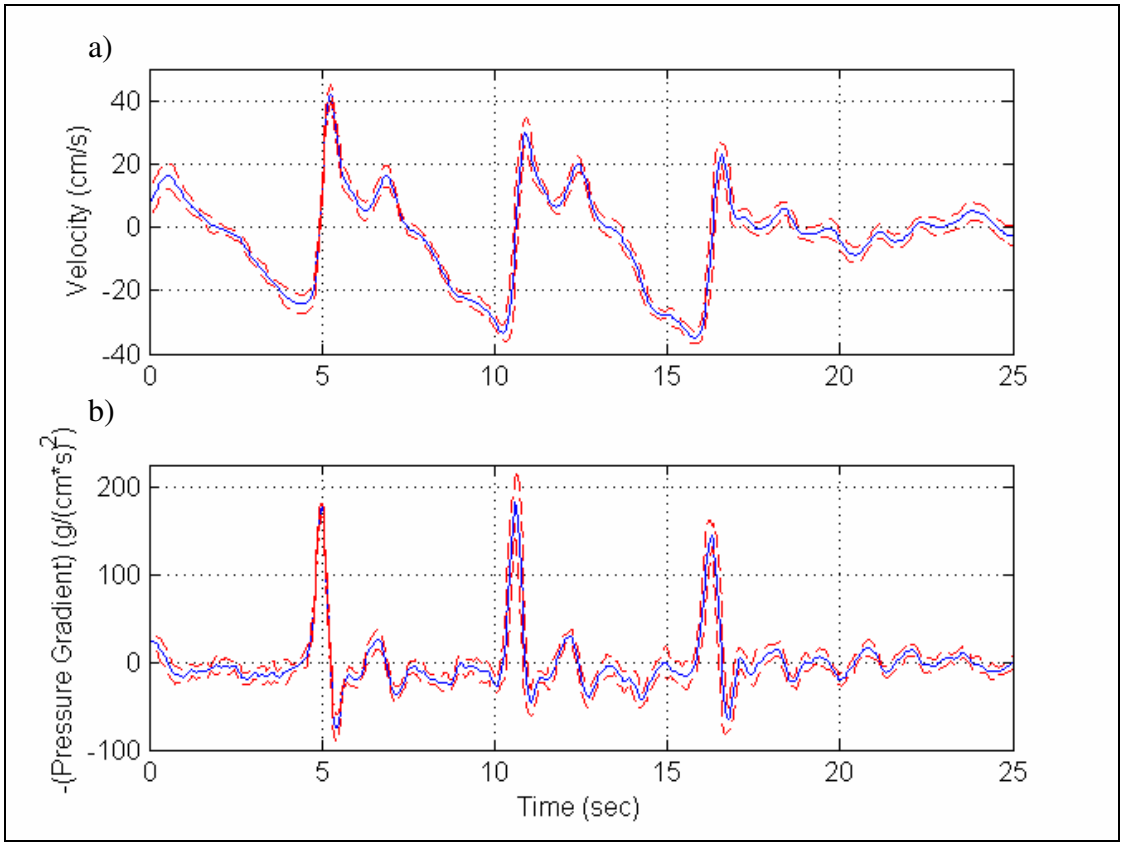

Figure 6 - Three-Wave Burst Velocity and Pressure Gradient Time Series

This wave condition has a few shortcomings that make it not ideal for generating and measuring subsurface transport of the sediment. First, the maximum negative pressure gradient is larger in magnitude than other wave conditions tested later in this study. Second, after each wave's maximum velocity a secondary velocity peak occurs, creating an additional back and forth subsurface movement. Third, measurement of subsurface and surficial transport can only be made in increments of three waves. Lastly and perhaps most importantly, the three wave burst produces back and forth subsurface movements, but no net forward subsurface movement. This is partly due to the large negative pressure gradient. The colored sediment column returns to its original location after the waves have passed overhead.

To rectify these issues the solitary wave condition was developed.

3.4.2 Solitary Wave

A second wave condition was developed by modifying the program developed by *Carter* (2002). The program was originally written to produce 2nd order Stokes waves by evaluating a continuous, analytical function prescribing the position of the wave maker piston at each time step. *Carter's* program was modified to obtain greater level of control over the motion of the wave paddle by enabling it to read a wavemaker position from a vector at each time step. The modified program allows the user to piece together different curves in any combination, instead of relying on a single analytical expression. A temporal discretization of 1/40 of a second produced smooth wave paddle motion. The vector of wavemaker positions can be modified without recompiling the Borland C/C++ wave generation program.

When using the external wavemaker control it is important to ensure that the prescribed wavemaker motion does not exceed the wavemaker's capabilities. Prescribing a large acceleration of the wave paddle can create very high pressures in the wavemaker's hydraulic system, possibly leading to damage. In addition, the maximum excursion amplitude (~30 cm) of the wave paddle should not be exceeded. Both of these factors must be taken into consideration when specifying the wavemaker's motion. A signal's characteristics should be verified with an oscilloscope before being used to operate the wavemaker.

Many different types of waves were tested to find a wave that had a large maximum pressure gradient which was not followed by a large magnitude negative pressure gradient. A solitary type wave was found to yield the best characteristics.

According to *Dong and Huang* (2004), a solitary wave can be generated with a piston-type wavemaker using the following wavemaker displacement, ξ, as a function of time:

$$\xi(t) = \frac{H}{Kh} \tanh K(c_s t - \xi) \tag{18}$$

where:

$$K = \sqrt{3H/4h^3} \tag{19}$$

and:

$$c_s = \sqrt{g(h+H)} \tag{20}$$

H is the solitary wave height above still water level, h is the still water depth, and c_s is the theoretical phase velocity of the solitary wave obtained from *Mei et. al*. (2005).

The generation of an exact solitary wave is not required in this study as the wave is not of permanent form (breaking) as it passes over the test section. An explicit form similar to that of equation (18) was developed to pass one wave over the test section at a time. The coefficients for this equation were chosen by trial and error. The equation used in this study to create a solitary wave is:

$$\xi(t) = Q \tanh(E + Bt) \tag{21}$$

where Q = 25.69cm, E = -7 (dimensionless), and B = 6.69s^{-1}, time is started at t = 0s, and points are calculated until t = 9s.

This wave condition will be referred as the "solitary wave," which, as implied by the name, consists of a single wave. A flume water depth (from glass flume bottom to water surface) of h= 34.3 cm and a ramp length of 244 cm (ramp inclination of 5 degrees from horizontal) was

used for this wave condition. The wave is already broken by the time is passes overhead the colored bead column. The movement of the wavemaker is shown in Figure 7. Positive wavemaker displacements are in the direction of wave propagation relative to the wavemaker's mean position.

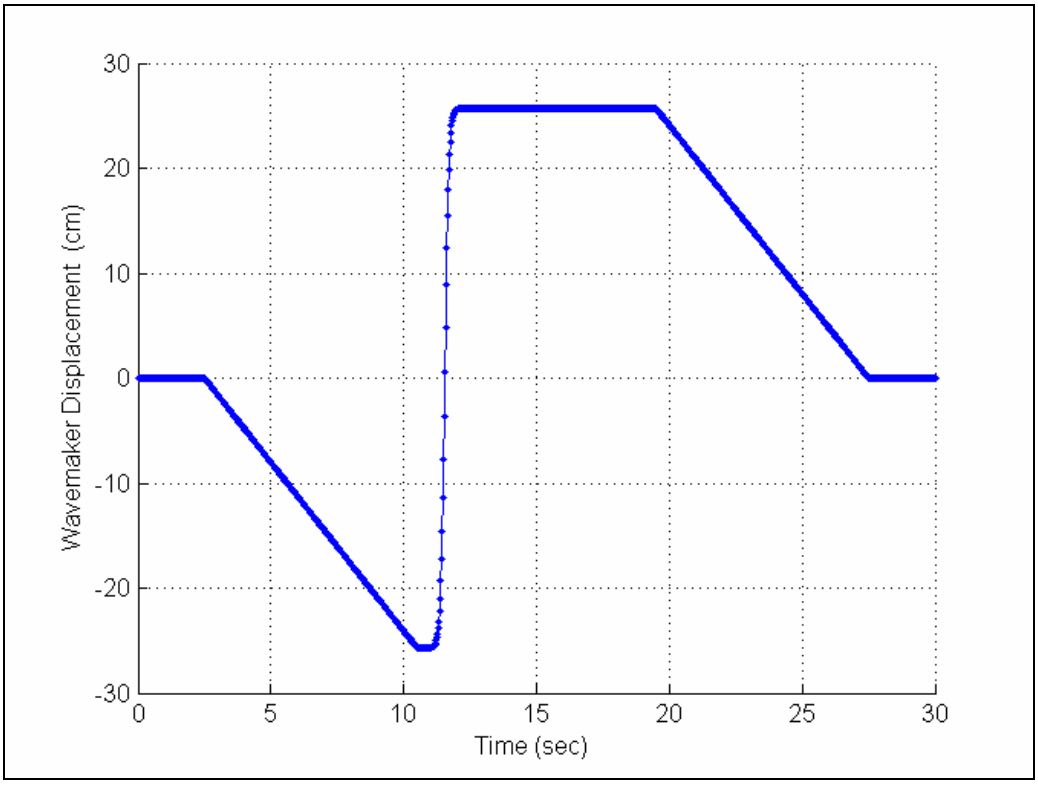

Figure 7 – Entire Wavemaker Movement Used to Generate Solitary Wave

The wavemaker piston's forward excursion was maximized by first moving it back to near the wavemaker's minimum negative displacement before moving it forward as a hyperbolic tangent to near the wavemaker's maximum positive displacement. The initial and final wavemaker movements were at a constant velocity small enough to create only a slight disturbance in the flume. The forward movement of the wavemaker is detailed in Figure 8.

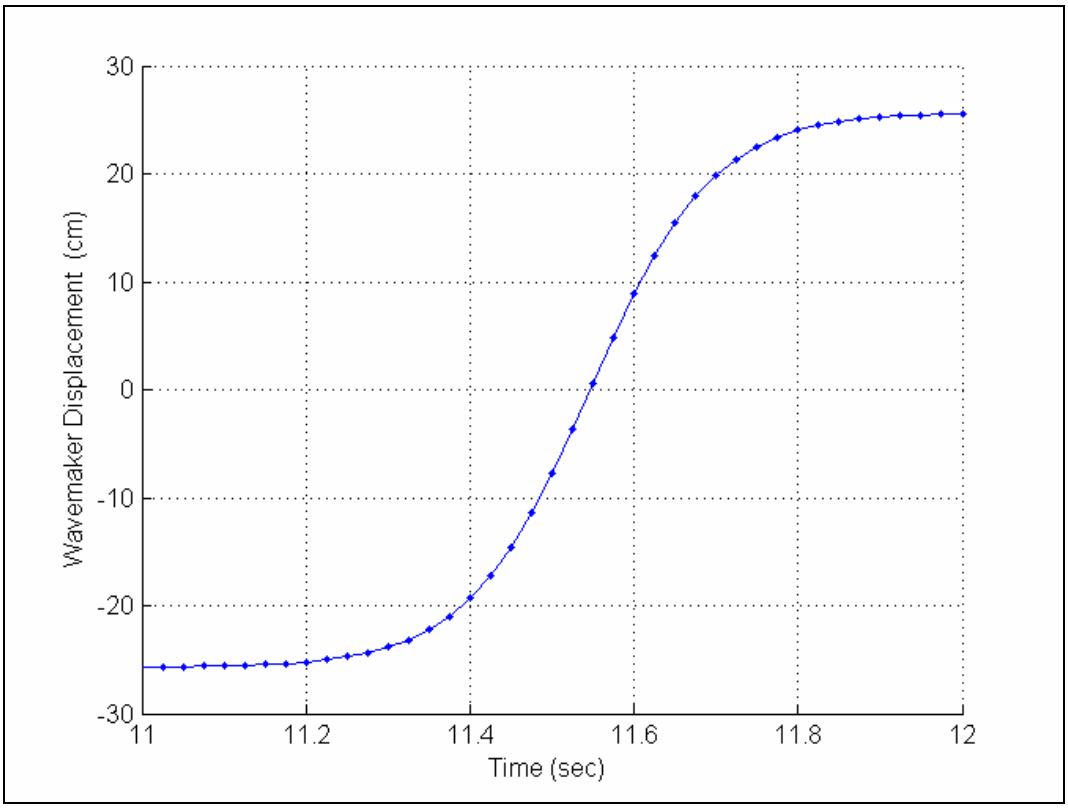

Figure 8 – Forward Wavemaker Movement Used to Generate Solitary Wave

The wavemaker was moved from its minimum negative position to its maximum positive position in the least amount of time possible in order to generate the largest wave height. This is accomplished by increasing the *B* parameter in equation (21). If the wavemaker paddle was prescribed to move at a velocity higher than shown in Figure 8 the wavemaker appeared to struggle by emitting an uncharacteristic sound. To avoid damage to the wavemaker, the movement was chosen to be below this threshold.

The velocity and pressure gradient time series for this wave condition is shown in Figure 9.

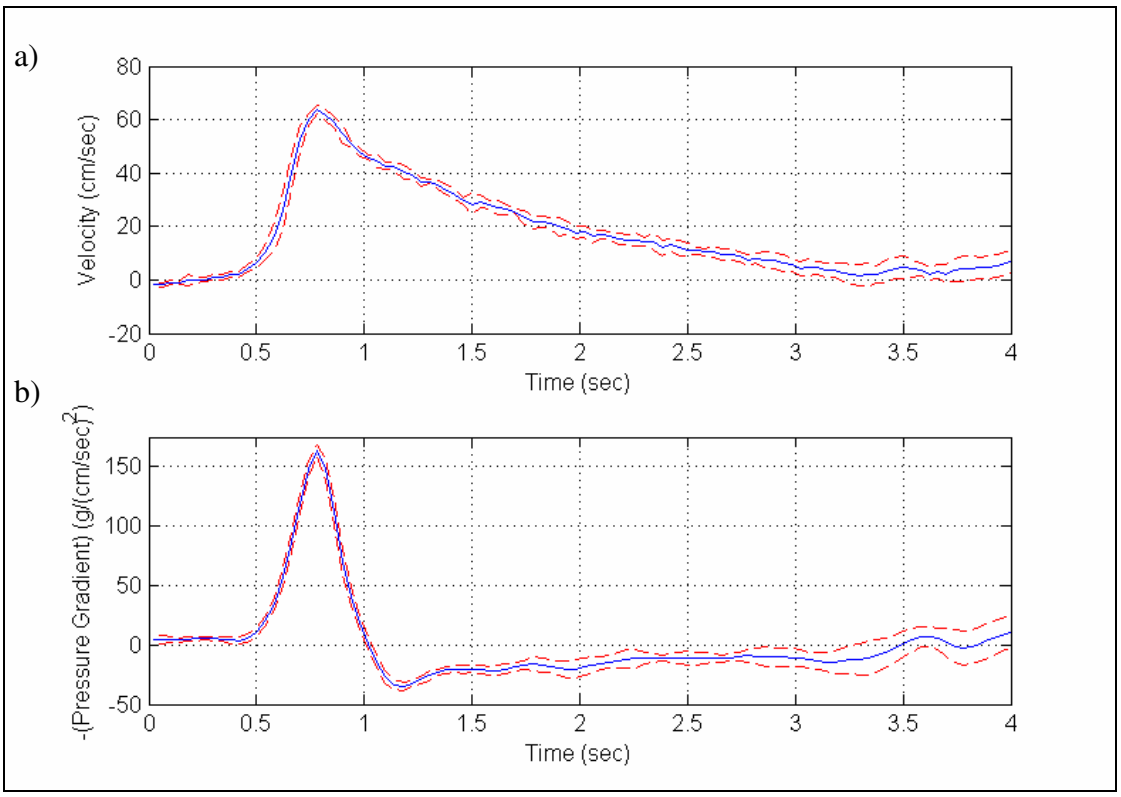

Figure 9 - Solitary Wave Velocity and Pressure Gradient Time Series

This wave condition does not exhibit the double velocity peak as seen in the three wave burst. In addition, a net subsurface transport is recorded as this wave is passed over the test section.

3.5 WAVE MEASUREMENTS

Two systems were used to measure the waves as they passed over the test section. A wave gauge system was used to measure the wave's surface profile and phase velocity. An Acoustic Doppler Velocimetry System was used to measure the orbital wave velocities as well as sediment-water interface elevations. Both systems are described in the following sections.

3.5.1 Wave Gauge System

3.5.1.1 Measurement of Water Surface Elevation

Surface piercing wave gauges are mounted perpendicular to the still water level on verniers that permit graduated vertical movement. The verniers are then mounted to the carriage that rolls along top of the flume sidewalls, allowing the wave gauges to be moved longitudinally along the length of the test section.

The wave gauges, manufactured by DHI, consist of two 1/8" parallel rods that extend into the water column. A signal conditioning module transmits an electrical current through each gauge via a shielded cable. As the water level changes relative to the wave gauge, the resistance between the two rods responds linearly. The change in potential is sampled by a 16-bit A/D (analog to digital) board and stored on a PC running DOS. The A/D board is capable of sampling a 10V range, e.g. 0 to 10V, -10 to 0V, or any combination in between. To optimize the signal to noise ratio, the gain is adjusted on the signal conditioning module to use as much of the 10V range as possible for the given wave condition. However, given the shallow depth of the water above the false bottom of the test section and the small amplitude wave conditions used, obtaining a range of 10V was not possible. The gain was raised to the maximum level possible for all experiments to guarantee the largest feasible voltage range.

When using the wave gauges one should note:

-The wave gauge must be positioned low enough such that parallel rods pierce the water surface at all times during the passage of a wave.

-The wave gauges have to be mounted such that the plane formed by two rods is in the lateral direction of the flume. This minimizes the effect of local wave slope on the surface elevation measurements.

-After being submerged for several days in the flume, the wave gauges develop a film from ADV seeding material and other particulate matter in the flume. This residue must be wiped clean before using the wave gauges.

-The signal conditioning unit must be powered on for at least 24 hours before making measurements to allow the signal to stabilize.

-The wave maker must be operated for several minutes before testing to ensure the conductivity of the water throughout the tank is constant.

The zero-shift (offset) is adjusted to keep the voltage magnitude within the confines of the A/D board. This adjustment provides no amplification of the signal; it adds or subtracts a constant value to the voltage record. An oscilloscope is used for the adjustment of both voltage and offset before the signal is sampled using the A/D board.

PC software developed by Sontek was used to sample the signal. Data is recorded as integers values from 0 to 4096 at a rate of 0.1Hz to 25Hz. The following equation is used to convert the integer values to an equivalent voltage:

$$\text{Voltage} = \frac{20 * \text{Integer}}{4096} - 10 \tag{22}$$

To convert voltages into an equivalent surface elevation, the system is calibrated by vertically repositioning the wave gauges and recording the voltage and vernier reading at each position. The water surface must be stationary and the wave gauge must pierce the water surface at each

vertical position. Since the wave gauges have a linear correlation between rod submersion and voltage, a linear regression can be performed using two data points. However, to ensure that an accurate calibration is made, three or more points are used for the calibration. Thirty seconds of 25 Hz data is collected at each vertical displacement from the still water level (SWL) position and averaged to determine the representative voltage. The SWL position is the vertical position of the gauges at which the wave measurements are made. The fitted calibration equation is:

$$\text{Displacement from SWL} = \text{Slope} * \text{Voltage} + \text{y-intercept} \tag{23}$$

The slope and y-intercept are determined using a least-squares regression. The slope of the calibration is influenced by the gain level and the y-intercept is influenced by the position of the offset. Figure 10 shows a sample calibration of the wave gauge. The black diamonds represent measured data points.

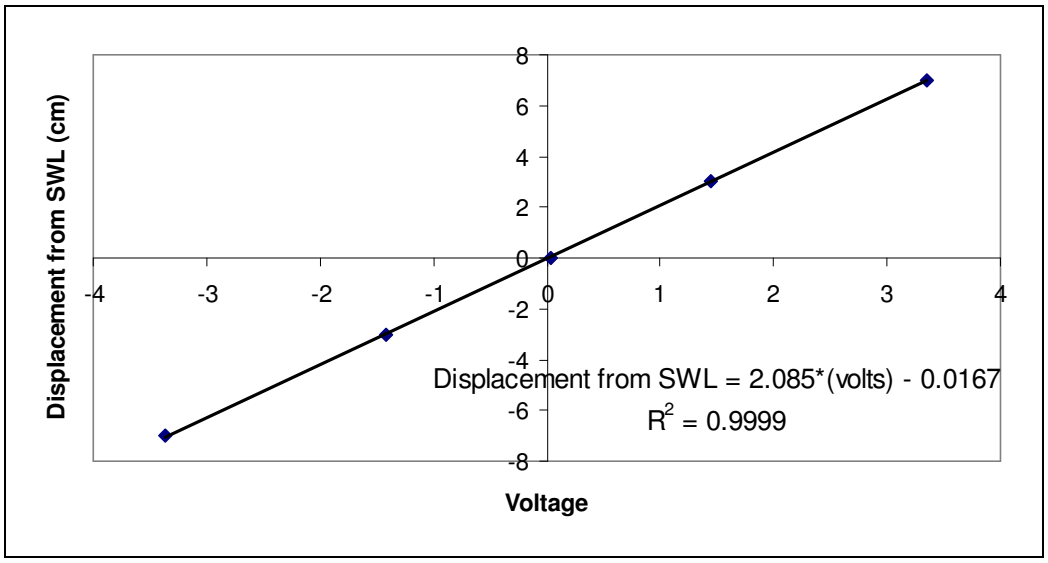

Figure 10 – Calibration of Wave Gauge

Applying (22) and the fitted calibration equation, the free surface displacement from the SWL can be determined at each time step from the data collected by the PC.

Sources of error in the wave gauge measurements can be attributed to two factors, vernier measurement errors and noise in the data acquisition system. The smallest unit of measurement on the vernier is 1 mm, thus the maximum likely measurement error is ±0.5 mm. The noise in the data acquisition system was found to have a peak to peak voltage of ±0.2V by *Carter* (2002). He found that the voltage error translates to a noise of ±0.2 cm in the measurement of the water surface at each time step. The measurement error (systematic) and noise (random) are uncorrelated, therefore for each time step:

Total Maximum Error in Wave Gauge Measurement = 0.5 mm + 2 mm = 2.5 mm (24)

It is expected that this level of error will be acceptable for use in this study.

3.5.1.2 Measurement of Wave Phase Velocity

One method used to estimate wave phase velocity over the test section utilizes two wave gauges separated by a known distance. Data from both wave gauges is collected simultaneously. By estimating the time that it takes for a particular wave feature to pass from one gauge to the next, the phase velocity can be found using the simple relationship:

$$c = \frac{\Delta L}{\Delta t} \tag{25}$$

where c is the phase velocity, ΔL is the distance between the two wave gauges, and Δt is the time that it takes for the wave feature to travel from one gauge to the next. Since the waves are breaking as they pass the wave gauges, there is some variability to be expected in the measurements of Δt. To reduce variability, several realizations of Δt are taken and averaged. Two wave features were tracked, the peak water surface elevation (crest) and the maximum slope of the water surface.

The accuracy of this method is also limited by the sampling frequency, f, of the A/D board. The maximum sampling error possible in a single measurement is found by calculating the error in phase velocity created by adding or subtracting a single sampling point to the measured value of Δt. Since points are sampled at a rate of $\frac{1}{f}$, a single measurement of Δt could correspond to an actual phase velocity within the range given by:

$$c = \frac{\Delta L}{\Delta t \pm \frac{1}{f}} \tag{26}$$

leading to a relative error in the measured phase velocity given by the range:

$$\text{Relative Error in } c = \left(\frac{1}{f(\Delta t) \pm 1} \right)(100\%) \tag{27}$$

The signal is sampled the highest frequency (f = 25 Hz) to minimize sampling error.

3.5.2 Acoustic Doppler Velocimetry System

A Sontek Acoustic Doppler Velocimetry System is utilized to provide velocity and bottom profile measurements in this study. The system consists of a probe, signal processing module, and serial connection for linking with a DOS-based PC. The probe is mounted to the carriage described in section 3.1 and can be adjusted in all three axes independently. The probe consists of three acoustic receivers that radiate out from a central acoustic transmitter. (See Figure 11)

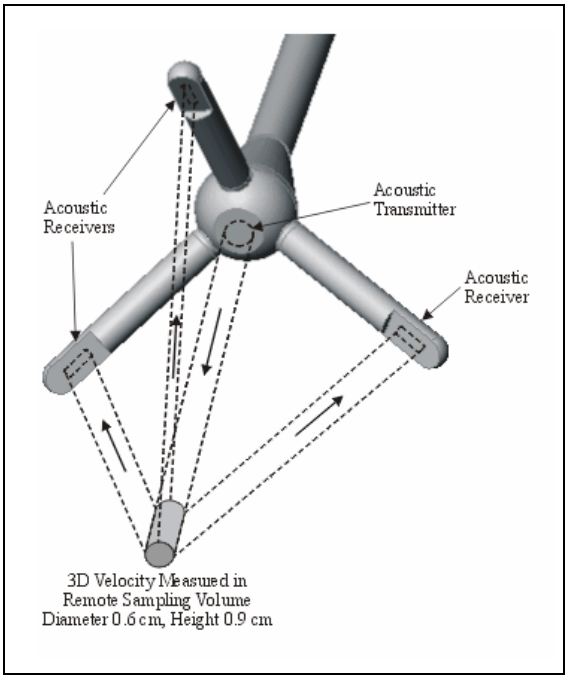

Figure 11 – ADV Probe Depiction (Sontek, 2006)

The transmitter emits acoustic pulses of a known frequency 200-250 times per second. The pulses travel out from the transmitter and reflect off ambient particulate matter *e.g.* microbubbles, detritus, or seeding material. Particulate material passing through a cylindrical sampling volume located ~5cm from the acoustic transmitter reflects a small amount of the transmitted signal back to the acoustic receivers which measure the reflection's frequency. The Doppler principle, which relates the frequency of the reflected signal relative to that of the transmitted signal, is used to ascertain the 3-D velocity of the fluid in the control volume. The probe's geometry is crucial to the calculation of velocity; each probe has a unique geometry which is provided by Sontek and must be uploaded to the computer before measurements can be taken. Since each of the 200-250 velocity realizations per second contain a high noise level, they are averaged over a user-specified time interval, Sontek (2006). The ADV used in this experiment is capable of sampling the velocity at frequencies from 0.1Hz to 25Hz. A sampling rate of 25 Hz was used for all measurements in this study. The sampling volume dimensions can

also be altered by the user, however, the default cylinder volume (6mm diameter by 9mm height) was used for this study because it is the most accurate.

The ADV is adjusted by the user to operate within a specified velocity range. Measurement error is proportional to the range's maximum velocity, so the smallest velocity range that still captures the entire wave record is used. The accuracy of the system is given by Sontek as 1% of the range's maximum velocity when operating at 25Hz and if the water contains a sufficient amount of particulate material. Ranges are available from ±3 cm/s to ±2.5 m/s. Any error of the system is random with a Gaussian distribution and contains no bias (systematic errors), Sontek (2006).

To ensure that enough particulate material is present within the sampling volume, seeding material (glass microspheres) are added to the water above the test section before measurements are made. Approximately two tablespoons of seeding material is dropped onto the water surface which is then agitated with a broom handle to properly disperse the particles. This will allow high-quality measurements to be taken for approximately 10 minutes. Along with velocity measurements, the ADV system records the signal to noise ratio (SNR) and the correlation of the data. The SNR (units of dB) is:

$$SNR(\text{dB}) = 10\log_{10}\left(\frac{P_{signal}}{P_{noise}}\right) \tag{28}$$

where P_{signal} is the power of the signal and P_{noise} power of the noise. Sontek suggests that the SNR be greater than 15 dB at all times to guarantee the accuracy of the measurement. The reliability of the measurement is measured by the correlation. The correlation (in percent) is given for each of the principal Cartesian directions. Sontek recommends that the correlation for each direction be greater than 70% (Sontek, 2006). In this study, the derivative of velocity is

taken to make estimates of a pressure gradient (see section 4.2.3). Because the acceleration record is extremely sensitive to noise in the velocity record, a SNR and correlation of 25 and 80 respectively, were maintained.

In addition to using the ADV to make measurements of velocity, the instrument was also used to make measurements of the sediment-water interface elevations. In one of the instruments startup screens, the distance from the probe to the nearest boundary is displayed. The ADV software was not designed to record measurements of the boundary distance; all distances were recorded by hand. The probe is positioned over the sediment tray to determine the local elevation of the sediment-water interface. The accuracy of the boundary distance measurements are ±1mm, Sontek (2006). *Carter* (2002) found that the accuracy of the boundary distance measurements were uncorrelated with magnitude of the distance measured. Section 4.1.2 outlines the procedure used to determine the bottom profiles using the ADV.

4 - METHODS

4.1 EXPERIMENTAL METHODS

To determine the importance of subsurface transport relative to surficial transport and provide data to which theoretical models can be compared, both types of transport were experimentally measured. The following sections describe the methodology used to make these measurements.

4.1.1 Measurement of Subsurface Transport

The colored bead column's movement is visualized through the transparent Plexiglas tray and the glass sidewalls of the wave flume. The colored column can be observed from both sides of the wave flume. The movement is quantified by measuring the clear/colored bead interfaces relative to a line denoting the interface's initial position. The sediment column is photographed both while stationary (stills) and as it deflects as the wave passes overhead (videos). A Canon Power Shot S230 digital camera is used to take both the stills and video. A focal length of 6.5 mm was used in macro mode for every shot to provide consistency when translating the image dimensions into real-life dimensions. An incandescent lamp was used to illuminate each side of the test section to improve photographic quality.

Since successive images are compared to one another, it is necessary to ensure that each image is taken from exactly the same position. A mark made on both the camera and the glass flume sidewalls are aligned before recording images. This ensures that the sediment column measurements are not distorted by parallax. The camera is placed touching the sidewall to maintain a constant distance from the lens to the sediment column between successive shots.

Still images are recorded as JPEGs at a resolution of 2048x1536. Videos are shot at a resolution of 640x480 with a frame rate of 15 frames per second in .avi format. The net subsurface transport of the sediment column under the action of waves can be determined from still pictures taken after several waves. Figure 12 shows still photographs of the sediment column's initial position and position of the column after 100 solitary waves. The images are stills of the sediment column at rest.

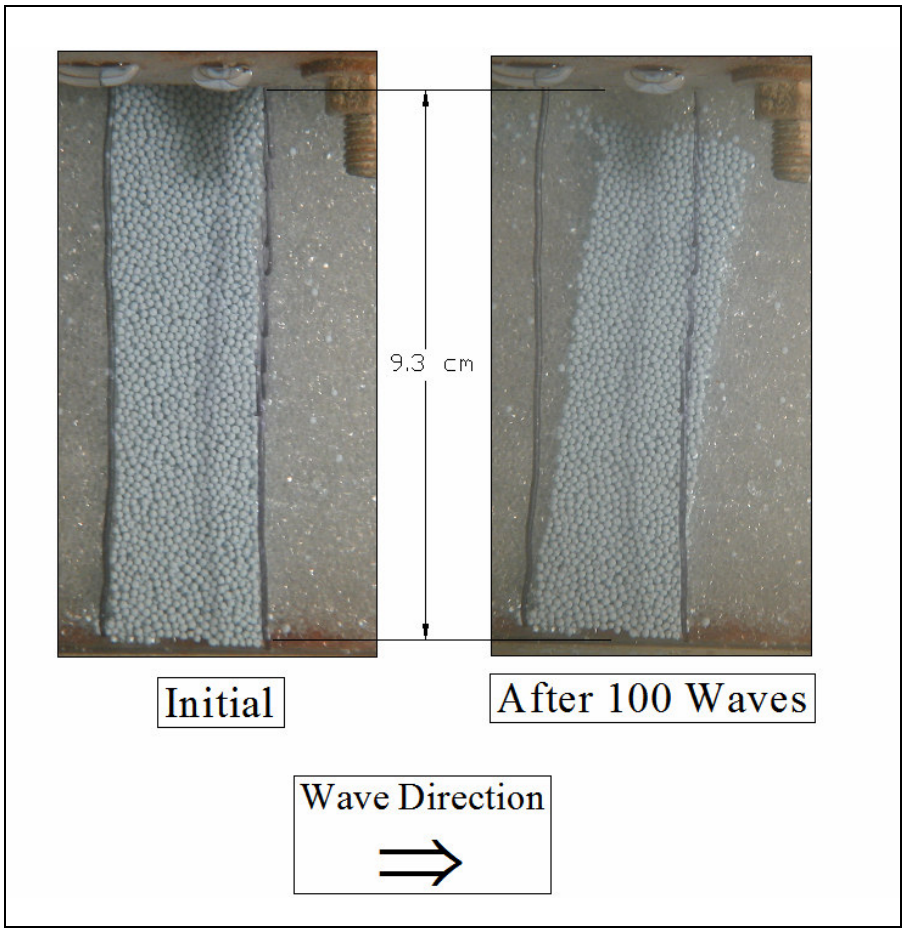

Figure 12 - Photographs of the Colored Sediment Column (Initial and After 100 Waves)

It can be seen in Figure 12 that the upper portion of the colored column has mixed with the clear beads and is no longer visible. This is due to surficial transport which is explained in section 4.1.2.

Videos of the sediment column are taken as the wave passes overhead, enabling quantification of the column's movement forward in the direction of wave propagation and movement back in the opposite direction after the wave crest has passed. The software *AVD Video Processor 7.1* is used to convert the video frames into still photographs. All images (both stills and video frames) are enlarged and printed in color on 8.5" by 11" paper. To convert between the dimensions of the prints and real-life dimensions, a scaling factor is determined by photographing an object of known size in each image. The scaling factor, *sf*, is determined by:

$$sf = \frac{\text{Real-Life Dimension of Object}}{\text{Dimension of Object's Image in Printout}} \tag{29}$$

For a focal length of 6.48mm while in macro mode, the scaling factor is 1.78. In other words, the prints are 1.78 times the real-life dimension. The scaling factor is verified for each experiment.

The sediment's initial position, either before any waves have passed over the bed (stills) or at the beginning of the video, can be determined using the enlarged prints. The movement of the sediment column relative to this initial position is found as a function of depth in each subsequent image. The column movements are found in 0.56 cm increments of depth (real-life dimension).

Using the sediment movement measurements from the still photographs taken of the sediment column at rest, the net depth-integrated subsurface transport can be found as a function of number of waves passed over the test section. Because the upper two centimeters of the sediment bed cannot be visualized (see section 3.2) and the top portion of the colored column

mixes with the clear beads, it is necessary to extrapolate the movements of the upper sediment bed when attempting to ascertain the depth integrated subsurface transport. The sediment movements from each photograph are fitted with a straight line using a least squares regression. The fitted line's equation is integrated from the shallowest depth at which a zero column displacement is measured to the sediment-water interface. Figure 13 shows the sediment column displacements after 100 solitary waves (blue dots) and the fitted line (red line). The data are obtained from Figure 12.

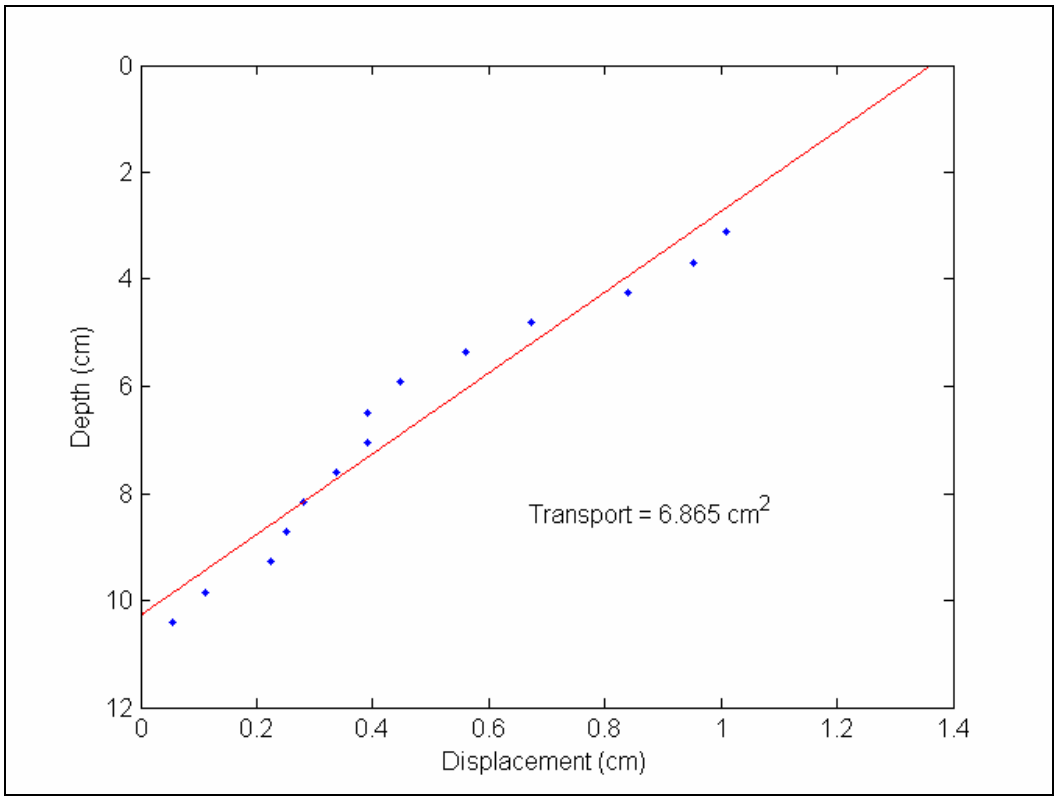

Figure 13 – Experimental Colored Sediment Displacement After 100 Waves

It is apparent that a better fit could be obtained using a polynomial or interpolant. Since we are extrapolating data from the top of the visible colored column to sediment-water interface it is important that the fitted equation be stable for the extrapolated region. Polynomial and interpolant regressions can sometimes give highly unrealistic sediment displacements for the extrapolated region. In addition, they can be highly sensitive to small changes in the shallowest

measured displacements. A linear regression is used to maintain consistency in the calculation of subsurface transport from image to image.

The subsurface transport quantity obtained by integration is found as a function of the number of waves passed over the test section. Using a linear least-squares regression, the data are fitted with a straight line. The slope of the regression approximates the net subsurface transport rate. Figure 14 shows the subsurface transport variation with number of solitary waves. The measured displacements are shown as blue dots and the linear regression is shown in red.

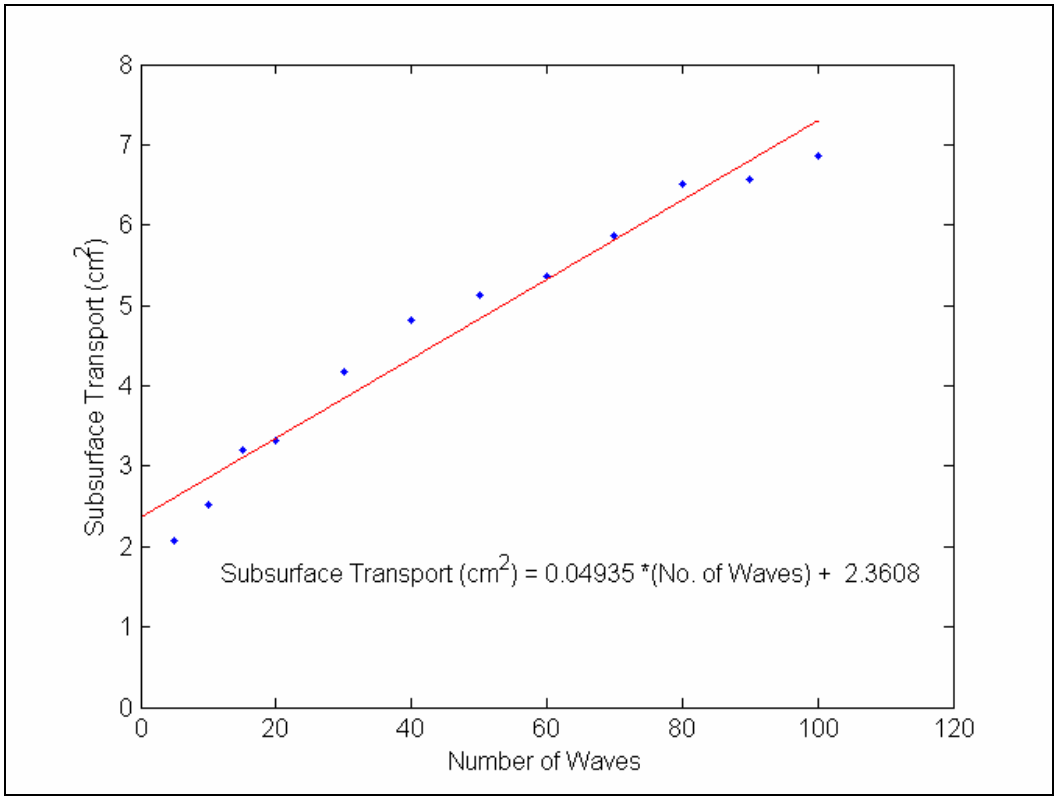

Figure 14 – Experimental Subsurface Transport as a Function of Number of Waves

There is a large subsurface transport after the first few waves have passed over the test section. See section 6.1.2.2 for explanations why this occurs.

Using a custom-made device that cuts two cross sections of the colored column, the lateral uniformity of the net movement of the colored column is verified. The cross section cutting device slides vertically within the confines of a wooden support which is clamped to the sides of the Plexiglas tray. After the experiment is complete, the colored/clear bead interfaces visible from the side of the tray are traced onto the transparent Plexiglas device and compared to the colored/clear bead interfaces of the cross-sections.

Figure 15 shows the colored sediment column from the side of the tray and from the cut cross-section. The column's position along the side of the tray is traced onto a transparency. This transparency is then placed on the cutting device and aligned in the same lateral position.

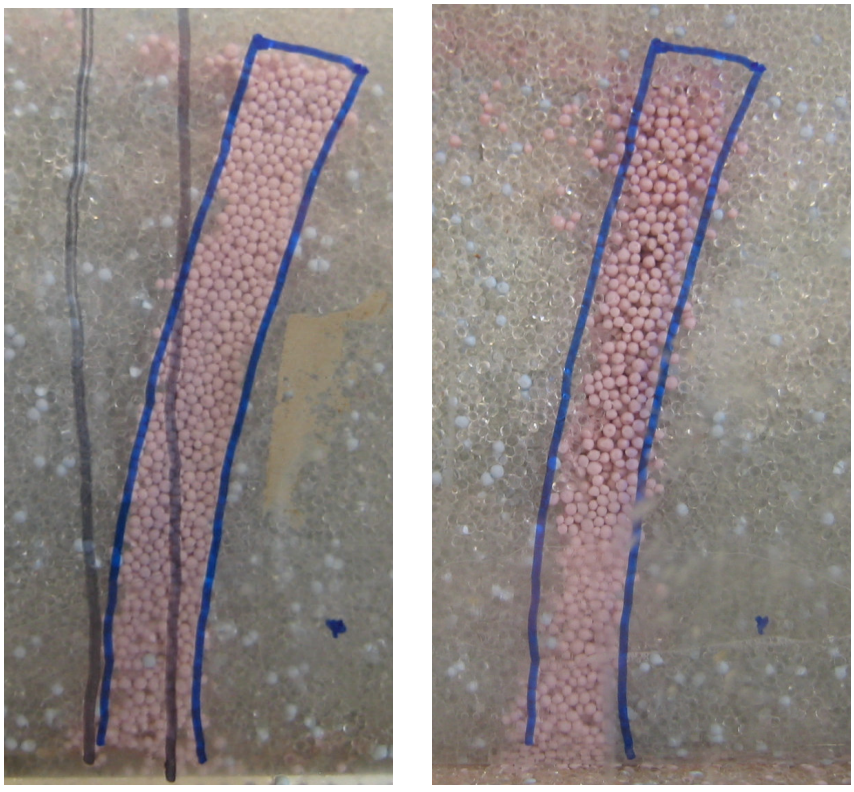

Side of Tray Cross-Section

Figure 15 – Verification of Lateral Uniformity of Colored Bead Column

The column is laterally uniform across the width of the tray with one exception. Along the inside edge of the tray the colored column extends roughly 3-4mm above the column at the cross-section. This could be the result of disturbing the colored column while moving beads from the downstream to upstream end of the box, because the sidewall's boundary effect, or due to particle movement as the sampler is forced into the sediment bed. Either way, the lateral differences in the column are negligible for the purposes of this study.

The lateral uniformity of the forward and reverse subsurface sediment displacements measured in the videos cannot be verified.

4.1.2 Measurement of Surficial Transport

4.1.2.1 Sediment Volume Test

Before measurements of surficial transport were made the accuracy of the ADV system (see section 3.5.2) and methodology used to calculate the surficial transport was verified. This was accomplished by adding a known volume of beads to the sediment tray and measuring the changes in sediment elevation. The sediment elevation changes can be converted into an equivalent volume which is compared to known volume of beads added.

The sediment bed was worn down to a highly eroded state by passing a couple hundred waves over the sediment tray. Once the sediment level is worn down several centimeters below its initial position, three longitudinal transects of the sediment-water interface's elevation are taken. The longitudinal transects are made by moving the ADV probe in two-centimeter increments along the length of the tray and recording distance from the probe to the sediment-water interface at each position. Each of the three transects is taken at a different lateral position by moving the

ADV probe in the y-direction. It would be ideal to space the transects equally, but because the raised sidewalls interfere with the ADV's reflected signal, this is not possible. Therefore, the outer two transects were moved inwards towards the tray's centerline. Figure 16 shows the ideal position of the transects and the position used in this study. The red, vertical arrows denote the transects. All dimensions are in centimeters.

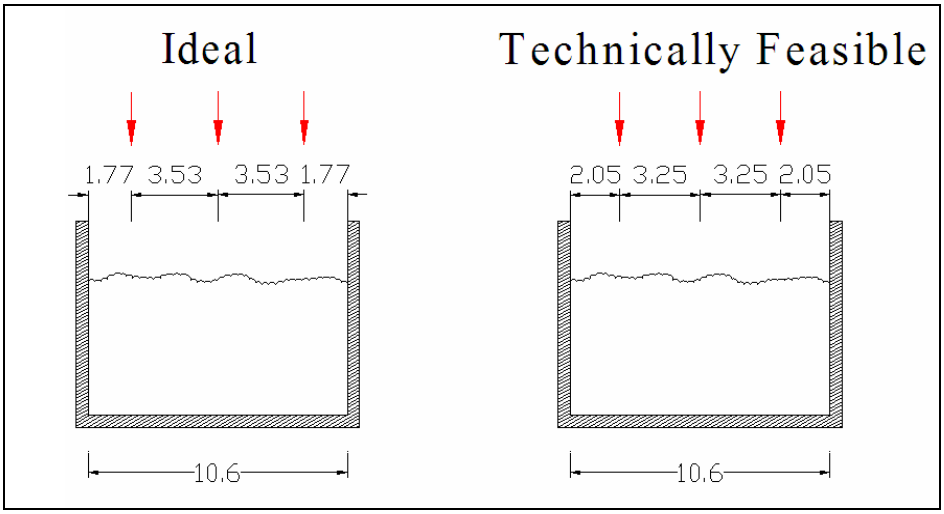

Figure 16 – Lateral Positioning of Transects

The three values at each longitudinal position are averaged. Next, two liters of plastic beads are carefully measured. The two liters of sediment are saturated with water and placed on top the beads already in the sediment tray. The transects are repeated to obtain new elevation measurements. The transects are then averaged for each longitudinal position.

Note: There was a lateral uniformity in the sediment elevation both before and after the two liters of beads were added. The laterally-averaged elevation represents the local sediment elevation within 0.5 mm (half a bead diameter). Because the "technically feasible" transect positionings are not equally spaced, the two outer transects should have a different weighting than the middle transect. However, because of the lateral uniformity of the sediment-water interface, it is safe to give each of the transects an equal weighting.

By subtracting the averaged transect of the sediment bed elevations after the two liters of beads were added from the averaged transect of the initial sediment bed, the change in sediment bed elevation is determined as a function of longitudinal distance. The elevation change is multiplied by the tray width and longitudinal discretization and summed over the longitudinal distance. A volume of 2036 cm^3 was obtained (a ~ 2% relative error from the actual volume added). This level of accuracy is expected to be sufficient for this study.

4.1.2.2 Measurement of Surficial Transport

To determine the amount of surficial transport it is necessary to make measurements of the sediment elevation before and after a number of waves have passed over the test section. After some initial testing, it was found that as the number of waves that have propagated over an initially flat bed increases, the amount of transport per wave decreases. To obtain accurate measurements of the surficial sediment transport beneath the solitary wave condition only six waves are passed over the test section before the sediment bed is replenished and smoothed. Just one three-wave burst is passed over the test section before replenishing and smoothing.

In order to neglect the subsurface transport that occurs concurrently with surficial transport, a large number of waves are passed over the sediment bed before any measurements are taken. Because an attenuation of subsurface transport occurs after many waves, its contribution to the total sediment transport measured by this method can be neglected. See sections (5.3.1) and (5.3.2.2) for analyses of the relative magnitudes of subsurface and surficial transport after many waves have been passed over a sediment bed.

The finite length of the box affects the measurements of surficial transport. There is no flux of sediment across the upstream end of the tray, leading to an erosion of the upstream portion of the sediment bed. Also, the end condition can make it difficult to enter the downwave sediment bag creating an accumulation of transported beads at the downwave end of the box. To achieve a constant transport, q_s, the difference in sediment elevation before and after waves are passed over the sediment bed must be negligible. For the wave conditions presented in this study, the elevations in the middle of the tray yields a constant transport. The end effects are quantified and discussed later in this section.

Both Wave Conditions:

The following is a list of procedures used to make measurements of surficial transport for both wave conditions:

1. The sediment bed is prepared by filling the tray with beads up to the level of the top of the plywood to the tray's sides.
2. A large number of waves are passed over the test section as to minimize the contribution of the subsurface transport.
3. A small stick, with the same width as the tray, is used to level the sediment surface, making the sediment-water interface uniform laterally and longitudinally.
4. Three transect measurements, identical to those made in the sediment volume test, are made to obtain the initial sediment elevations.

For the Solitary Wave Condition:

5. Two waves are passed over the test section and three transect measurements are taken. This step is repeated for a total of three times.

6. The sediment collection bags on either end of the tray are removed. The sediment contained within them is emptied so that the bead volume can be measured once it is dry.

7. The sediment bags are reattached and the entire process is repeated.

For the Three-Wave Burst Wave Condition:

5. One three-wave burst is passed over the test section and three transects are taken.

6. The sediment bags are removed and emptied. The beads within are dried and measured by volume.

7. The sediment bags are reattached and the process is repeated.

The inside dimension of the sediment tray is 1.03m; however, the ADV probe is only capable of measuring the sediment elevations 1.5cm from the up and down wave ends of the sediment tray's inside edge. This leaves a 1m long section in the middle of the tray in which measurements can be made. The most upstream point which the sediment levels are measured is denoted as station 0. The station number of each subsequent measurement in the downstream direction is given in terms of its distance from station 0. Fifty measurements (station 0 to station 100) are taken with a 2cm longitudinal discretization. The changes in sediment elevation in the two unmeasurable zones on either end of the tray are undoubtedly influenced by boundary effects. Any sediment elevation changes in these zones are not reflected in transport calculations and therefore introduce an error in conservation of sediment calculations. However, the length of the two unmeasurable zones is smaller than the spatial discretization used to evaluate the sediment elevations in the measurable zone of the tray; the error induced by two unmeasurable zones is expected to be within the confines of the experimental method.

Using the sediment surface elevation measurements before and after two waves have passed over the test section, the average surficial sediment transport, q_s, can be determined using the sediment continuity equation:

$$(1-n)\frac{\partial \zeta}{\partial t} = -\frac{\partial q_s}{\partial x} \tag{30}$$

where ζ is the sediment surface elevation. The derivatives in (30) can be estimated using finite differences. In addition since we want to find the transport per wave instead of in terms of time, the change in time, Δt, can be written as the change in the number of waves passed over the test section, Δwave. If these modifications are made the following is obtained:

$$(1-n)\frac{\Delta \zeta}{\Delta\text{wave}} = -\frac{\Delta q_s}{\Delta x} \tag{31}$$

Solving for the change in surficial transport:

$$\Delta q_s = -(1-n)\frac{\Delta \zeta}{\Delta\text{wave}}\Delta x \tag{32}$$

Equation (32) is used to determine the change in transport in the direction of wave propagation at each measurement of sediment elevation change. To determine the amount of transport at the upstream edge of the sediment tray, $q_s(0)$, the flowing equation is used:

$$q_s(0) = -(1-n)\frac{V_{up}}{B(\Delta\text{wave})} \tag{33}$$

where V_{up} is the volume of sediment collected in the upwave bag and B is the width of the sediment tray. To find the total surficial sediment transport, q_s, the changes in transport, Δq_s, are summed at each station in the direction of transport over the length of the sediment tray (from station 0 to station 100) yielding a record of the total transport at each station. Figure 17

shows the average surficial transport of one solitary wave. The error bars denote one standard deviation from the mean. This wave is the average transport per wave of the first two waves propagated over an initially flat, prepared sediment bed. Three realizations were measured.

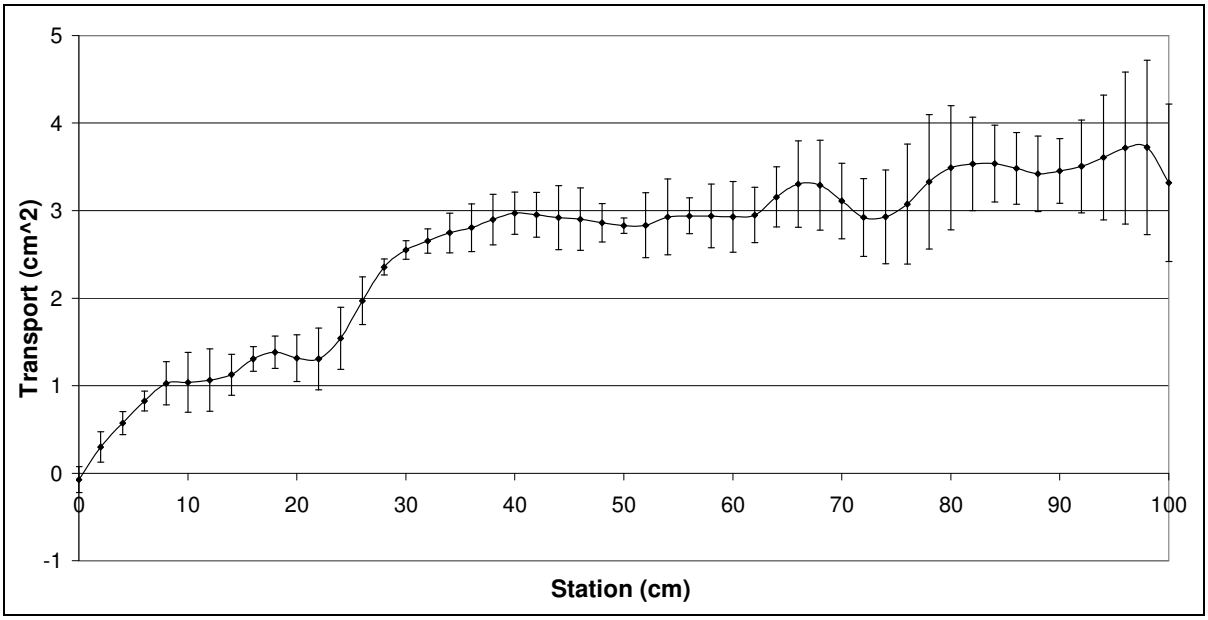

Figure 17 – Typical Average Surficial Transport Record for One Solitary Wave

It can be seen that there is a large increase in transport over the first ~40cm of the sediment tray. This is attributed to the upstream sediment tray boundary condition. The ~40 cm distance is correlated with the excursion length of a sediment particle within the tray. Section 4.2.3 gives the formulas used to calculate the excursion length of the particles.

The downstream sediment tray end boundary condition also has an effect on the surficial sediment transport, although apparently not as pronounced as the upstream condition. The sediment collection bag is held open using a Plexiglas rectangular sleeve that allows the sediment to freely enter the bag. Sometimes, however, sediment collects at the downstream end of the tray/bag opening which disrupts the surficial transport. This phenomenon can be seen in

Figure 17 at station 100 where transport is reduced relative to stations upwave. It could also possibly be responsible for the gradual increase in transport from station 75 to station 98.

The representative amount of surficial transport is obtained from the center of the tray where the transport is nearly constant. This corresponds to stations 40 through 60 in Figure 17. This value will be compared to the theoretical surficial transport. (see section 4.2.2)

A sediment balance (or closure of the method) is accomplished by comparing the volume of sediment collected in the downwave bag, V_{do} with V_e. V_e is the volume of sediment that should be in the bag based on the surficial transport measured at station 100. Each wave condition has a separate expression.

for the Three-Wave Burst (TWB):

$$V_e = \frac{B}{(1-n)}\left(q_s(100)\right) \tag{34}$$

for six Solitary waves:

$$V_e = \frac{2B}{(1-n)}\left(q_{s1}(100) + q_{s2}(100) + q_{s3}(100)\right) \tag{35}$$

where q_{s1} is the transport per wave for the first solitary wave pair, q_{s2} is the transport per wave for the second wave solitary wave pair, and q_{s3} is the transport per wave for the third solitary wave pair. The difference between V_{do} and V_e is an indicator of the accuracy of the method used to calculate the surficial transport. These two values are compared after each three wave burst and

after six solitary waves. The relative error between the two measurements averages 9% for the solitary wave condition and 10% for the three-wave burst. This level of accuracy is sufficient for the purposes of this study.

4.2 THEORETICAL METHODS

4.2.1 Determination of Phase Velocity

To perform many of the calculations presented in this study, namely transferring between spatial and temporal domains (see section 4.2.4.1), knowledge of the phase velocity is required. Three different theoretical formulations of phase velocity are compared for the waves presented in this study. For the solitary wave condition, linear shallow water wave theory and solitary wave theory are used to estimate to the phase velocity. For the three-wave burst, linear shallow water wave theory and cnoidal wave theory are utilized. It should be noted, however, that these theoretical calculations of phase velocity assume a wave of permanent form. The wave conditions presented in this study are breaking and evolving as they pass over the test section. Therefore, these formulations are expected to give only rough approximations of the phase velocity for wave conditions presented in this study.

4.2.1.1 Linear Wave Theory

According to linear wave theory, the phase velocity, c_l, of a sinusoidal wave of permanent form is given as:

$$c_l = \sqrt{gh\frac{\tanh(hk)}{hk}} \tag{36}$$

where:

$$k = \frac{2\pi}{L} \tag{37}$$

with k being the wave number and L the wavelength. However, this expression can be simplified if the water is considered shallow (or the wave "long"); *i.e.* the wavelength of the wave is much longer that the local water depth. The following criterion is used to determine if the shallow water approximation can safely be made.

$$\text{Shallow Water if: } \frac{h}{L} < 0.05 \tag{38}$$

For the wave conditions presented in this study, this criterion is well within the shallow water limit. If the shallow water criterion is met the following approximation can be made:

$$\frac{\tanh(hk)}{hk} \simeq 1 \tag{39}$$

simplifying (40) to :

$$c_{ls} = \sqrt{gh} \tag{40}$$

However, if the shallow water criterion is not satisfied this approximation cannot be made. For a given period, T, the length of the wave in deep water, L_o, is:

$$L_o = \frac{g}{2\pi} T^2 \tag{41}$$

Using *Guo* (2001) the wavelength of the wave propagating in a fluid of depth, h, can be approximated by:

$$L = L_o \left[1 - \exp\left\{ -\left(\frac{2\pi h}{L_o} \right)^{1.25} \right\} \right]^{0.4} \tag{42}$$

and the linear phase velocity at any water depth, c_l, is given by:

$$c = \frac{L}{T} \tag{43}$$

4.2.1.2 Solitary Wave Theory

The phase velocity of a solitary wave is given by *Mei et. al.* (2005) as:

$$c_s = \sqrt{g(h+H)} \tag{44}$$

where H is the wave. A true solitary wave is symmetric, of permanent form, and of infinite wavelength. It should be noted, however, that the "solitary" wave condition (presented in 3.4.2) produces waves that are neither true solitary waves in the constant depth portion of the flume nor upon reaching the test section.

4.2.1.3 Cnoidal Wave Theory

To be classified as cnoidal, a shallow water wave must meet the following criterion:

$$U = \frac{HL^2}{h^3} > 26 \tag{45}$$

where U is the Ursell number. Cnoidal waves are weakly non-linear and have surface profiles that are defined through the use of Jacobian Elliptic cosines. The phase velocity of a cnoidal wave can be found by iteration through the use of:

$$c_c = \sqrt{gh\left(1+\frac{AH}{h}\right)} \tag{46}$$

where A is a function of the Ursell number and can be found in a table provided by *Skougaard et. al.* (1974).

To calculate the phase velocity of the wave in the three-wave burst using cnoidal theory, a first approximation of the phase velocity is made using linear shallow theory, (40). With this estimate, *L,* the wavelength can be determined using:

$$L = cT \tag{47}$$

where c is the phase velocity and T is the wave's period, obtained from the period of the wavemaker's prescribed sinusoidal motion. With this estimate, a first approximation the Ursell number can be found using (45). Next, using the Ursell number, the A parameter can be approximated using *Skougaard's* table. From this, an estimate of the cnoidal phase velocity can be made using (46). The wavelength is then recalculated using (47). The process is repeated until the estimate of phase velocity converges.

4.2.2 Modeling Surficial Transport

This section explains the theoretical methods used to estimate the surficial transport using the ensemble-averaged velocity record obtained from the ADV system at five different positions along the length of the sediment tray. A Meyer-Peter Mueller (MP-M) type bedload formulation is used to estimate the surficial transport at each of these positions.

The first step in these calculations is the determination of the bottom wave friction factor, f_w, for the breaking, asymmetric waves in this study. The friction factor depends on two parameters, A_{bm}, the bottom excursion amplitude, and k_N, the equivalent Nikuradse sand grain roughness of the sediment. This study compares two procedures for obtaining the equivalent A_{bm} for a forward leaning wave. The methodology will be developed first for a solitary wave, with only

positive orbital velocities. Next, the methodology will be extended to waves with both positive and negative velocities.

4.2.2.1 Solitary Wave

Ten realizations of velocity are obtained for each of the five positions along the length of the sediment tray. The realizations are aligned using the peak velocity and averaged for each position. Figure 18 gives the ensemble-averaged velocity record (blue line) of the solitary wave at station 50. The red lines indicate one standard deviation from the mean. The velocity record is consistent across each of the realizations.

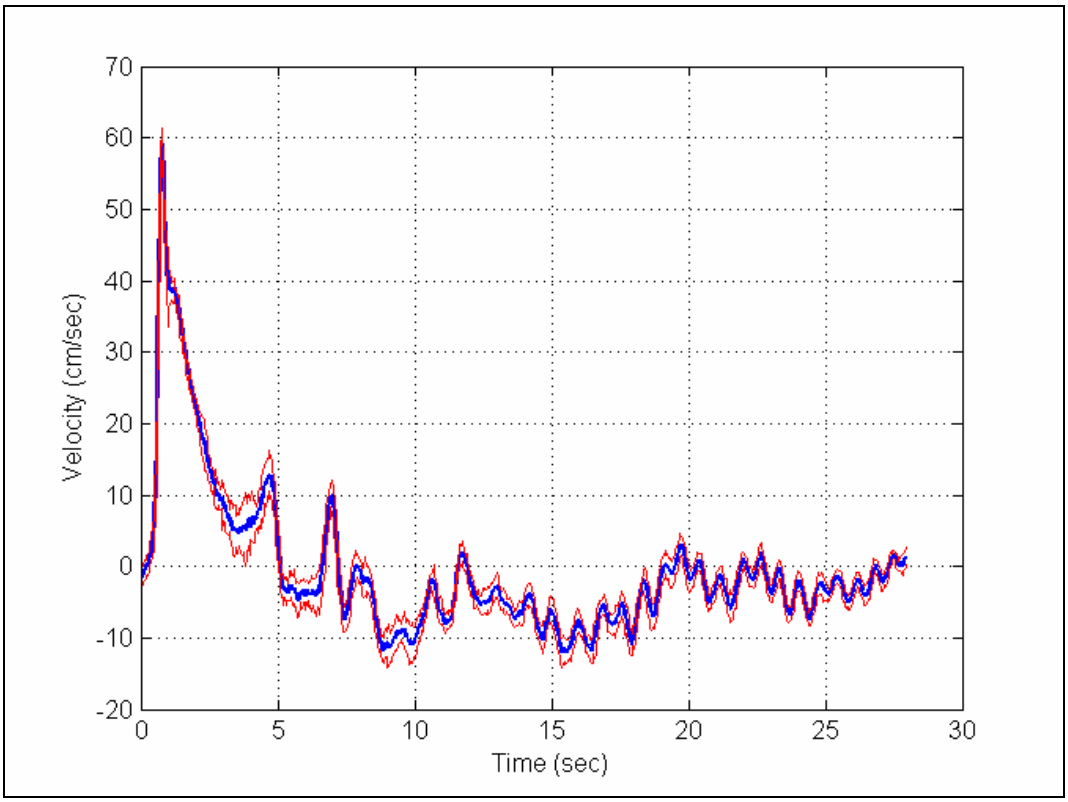

Figure 18 – Velocity Record at station 50

The rapid acceleration of the forward leaning, asymmetric waves up to the maximum velocity, u_{bm}, leads to an increased bottom shear stress. (see Section 2) In this study, the bottom shear stress associated with the rapid velocity rise will be used for the calculation of bedload transport throughout the entire wave record. Though obviously not entirely realistic as the thickness of the wave boundary layer continues to grow after u_{bm} is reached, this methodology provides a reasonable estimate of surficial transport near the peak velocity when the majority of the transport occurs. This method should yield a conservatively high estimate of bedload transport.

The first method used to determine the bottom excursion amplitude fits a sinusoid to the velocity rise using a least-squares regression. The regression varies the phase, amplitude, and period of the sinusoid to obtain the best fit. This method will be referred to as Method 1. The following expression is used to obtain the bottom excursion amplitude from the fitted amplitude and period.

$$A_{bm1} = \frac{u_{bmf}}{\omega_f} \tag{48}$$

and:

$$\omega_f = \frac{2\pi}{T_f} \tag{49}$$

where A_{bm1} is the bottom excursion obtained using Method 1, u_{bmf} is velocity amplitude obtained by the fitting, and T_f is the period of the sinusoid obtained by the fitting. Figure 19 shows the points used to perform the fitting for the solitary wave. Only points representative of the velocity rise are chosen for the regression. The fitted sinusoid is shown in black.

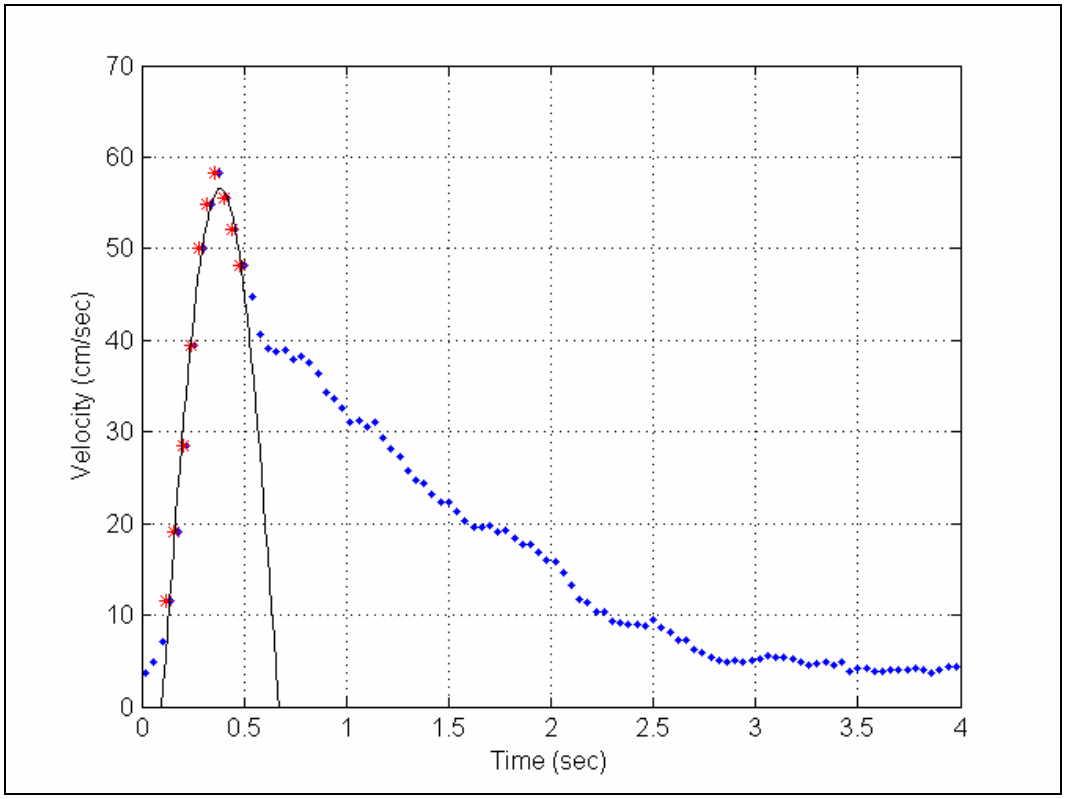

Figure 19 – Velocity Points Used for Fitting Sinusoid (Method 1)

For consistency, a few points after the peak velocity are used to fit the sinusoid. If only the velocity rise is used in the least squares regression, the fitted parameters can be somewhat unrealistic. Only the first few data points after the velocity maximum that seem to "belong" to the same sinusoid as the velocity rise are used in the fitting. This method incorporates some subjectivity when choosing which points should be used in the regression.

In Method 2, the velocity record is integrated from the first positive velocity to the maximum velocity to find the equivalent bottom excursion amplitude, A_{bm2}.

$$A_{bm2} = \int_{t_0}^{t_m} u dt \tag{50}$$

where t_o is time at which the velocity is zero and t_m is the time at which the maximum velocity occurs. Method 2 requires no fitting and does not rely on any subjective techniques as does Method 1.

Once the bottom excursion amplitude is obtained, using either Method 1 or Method 2, Steve McLean's approximation of the wave friction factor can be used to determine the wave friction factor:

$$f_w = \exp\left(5.5\left(\frac{A_{bm}}{30z_o}\right)^{-0.12} - 7.02\right) \tag{51}$$

where $30z_o$ is the bottom roughness. This expression is similar to that presented in *Madsen*, (1994).

The bottom roughness depends on the flow condition. If the sediment particles extend above the flow's viscous sublayer (where viscous effects dominate) the flow is considered rough turbulent whereas if they are completely beneath the viscous sublayer the flow is considered smooth turbulent. Rough turbulent flow is assumed and then verified. For rough turbulent flow:

$$30z_o = d \tag{52}$$

The wave friction factor calculated with the rough turbulent assumption is used to calculate the maximum wave shear velocity.

$$u_{*wm} = \sqrt{\frac{f_w}{2}} u_{bm} \tag{53}$$

where u_{bm} is maximum fluid velocity in the x-direction.

From u_{*wm} the smooth turbulent bottom roughness can be estimated using:

$$30z_o = 3.3\frac{\nu}{u_{*wm}} \tag{54}$$

The larger of the two $30z_o$ values, obtained using (54) and (52), is used to calculate the wave friction factor with (51). For the wave conditions and particle sizes in this study, the flow was always rough turbulent.

The Shields parameter, a dimensionless number that relates the bottom shear stress to the sediment particles' resistance to movement is given as:

$$\psi = \frac{\tau_b}{(s-1)\rho g d} = \frac{0.5 f_w |u| u}{(s-1) g d} \tag{55}$$

where:

$$s = \frac{\rho_s}{\rho} \tag{56}$$

τ_b is the bottom shear stress and u is the ensemble-averaged velocity measured above the test section. The Shields parameter is calculated for each velocity data point. If the magnitude of the Shields parameter exceeds a critical value, ψ_{cr}, bedload sediment transport will occur. The critical Shields parameter, ψ_{cr}, can be approximated by the following (*Soulsby*, 1997):

$$\psi_{cr} = \left(1 + \frac{\tan\beta(t)}{\tan\phi_s}\right)\begin{cases} 0.1 S_*^{-2/7} & \text{for } S_* < 0.8 \\ 0.095 S_*^{-2/3} + 0.056\left[1 - \exp\left(-S_*^{3/4}/20\right)\right] & \text{for } S_* > 0.8 \end{cases} \tag{57}$$

where:

$$S_* = \frac{d}{4\upsilon}\sqrt{(s-1) g d} \tag{58}$$

υ is the kinematic viscosity and $\beta(t)$ is the slope of the sediment water interface. A positive value of $\beta(t)$ is used if the direction of the instantaneous velocity is moving up the slope.

The bedload transport is given by the Generalized Meyer-Peter and Mueller equation (*Madsen*, 1991)

$$q_b = \begin{cases} \dfrac{14}{1+\frac{\tan\beta(t)}{\tan\phi_m}} \left|\psi - \psi_{cr}\right|^{3/2} \sqrt{(s-1)gd^3}\, \dfrac{|u|}{u} & \text{if } |\psi| > \psi_{cr} \\ 0 & \text{if } |\psi| < \psi_{cr} \end{cases} \tag{59}$$

The instantaneous bedload transport is calculated for each velocity data point (temporal resolution = 0.04s) using the instantaneous Shields parameter over the entire velocity record. The instantaneous bedload record is numerically integrated with respect to time to obtain a value of total bedload transport at each of the five stations. Figure 20 shows the instantaneous Shields parameter, instantaneous bedload, and cumulative bedload for the solitary wave condition at Station 50 using Method 2. In the top graph the red lines denote the critical Shields parameter.

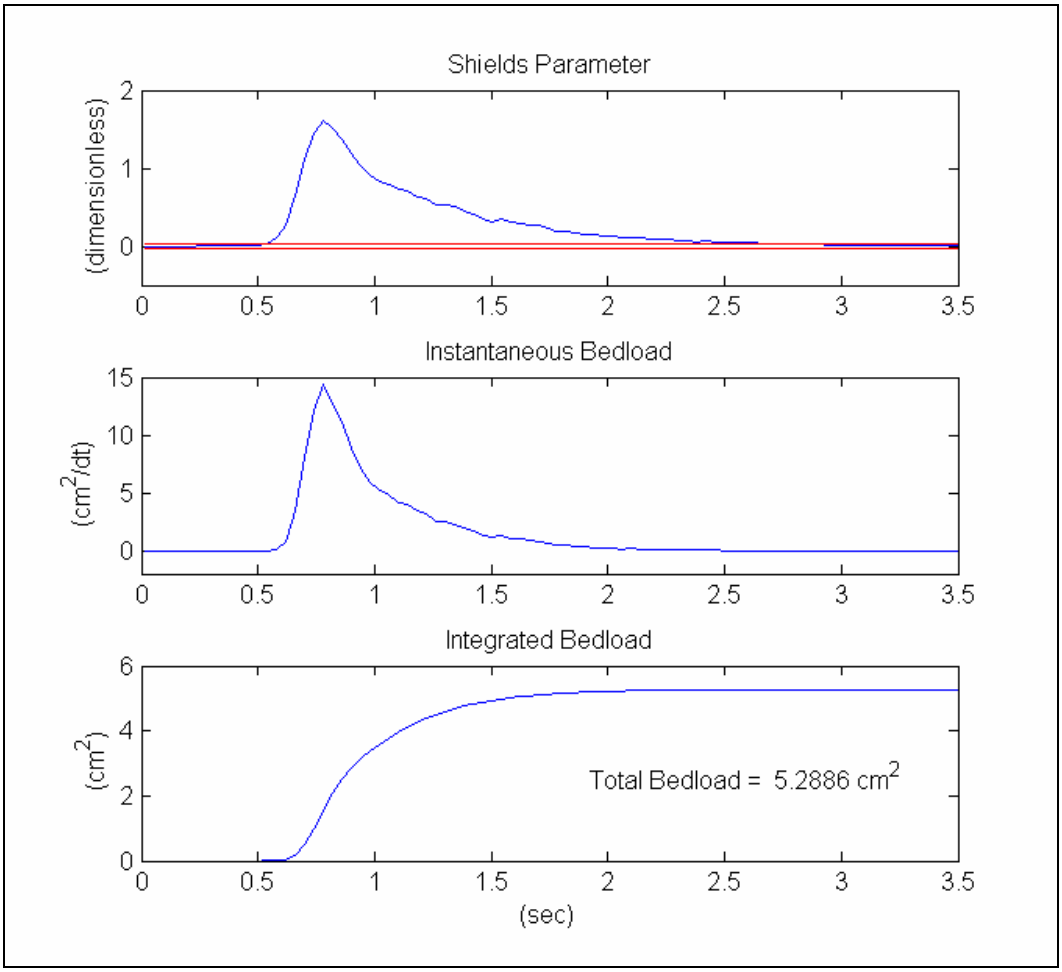

Figure 20 – Theoretical Bedload Measurements at Station 50

Methods 1 and 2 yield very similar results (within 10% of one another).

4.2.2.2 Periodic Wave

In order to account for the positive and negative velocities in the periodic wave case the negative and positive velocities are analyzed separately. Because the boundary layer that forms underneath a crest is separate and distinct from the boundary layer that develops under the trough, separate friction factors are developed for positive and negative velocities. A method analogous to Method 2 is used to determine A_{bmc}, the equivalent bottom excursion amplitude for the velocity rise under the crest, and A_{bmt}, the equivalent bottom excursion amplitude for the

trough. Figure 21 shows the intervals of the velocity record that is integrated to obtain A_{bmc} (in blue) and A_{bmt} (in red).

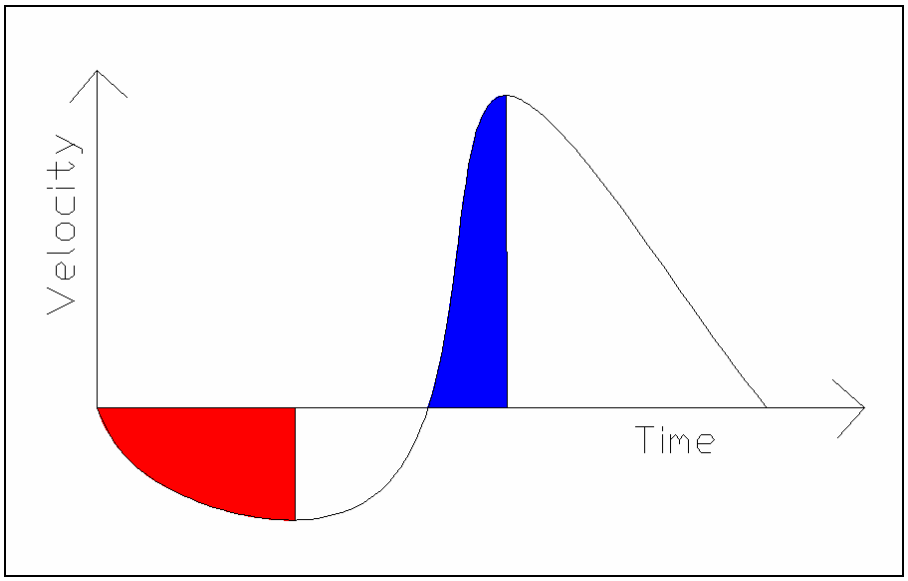

Figure 21 – Calculation of Friction Factors for an Assymetric Periodic Wave

For the velocities below zero, the equivalent amplitude is obtained by integrating from the velocity zero crossing to the maximum magnitude of negative velocity. To obtain the equivalent amplitude for the velocity rise, the record is integrated from the zero crossing to the maximum positive velocity.

After A_{bmc} and A_{bmt} have been obtained, the methodology to obtain the theoretical bedload transport is equivalent to that of Method 2. Two friction factors are determined with each of the amplitudes using (51). Using these friction factors the bedload transport is calculated for the negative and positive velocities separately. The seaward and shoreward directed instantaneous transport quantities are then integrated over the complete wave record to determine the total theoretical bedload transport. The transport beneath multiple crests and troughs can be estimated with this method.

4.2.3 Calculation of Bead Excursion Lengths

To roughly approximate the average distance a sediment particle would travel under a wave the critical velocity, u_{cr}, equivalent to the critical Shields parameter, ψ_{cr}, is found. If this velocity is exceeded sediment movement can be expected. The critical velocity is obtained from:

$$u_{cr} = \sqrt{\frac{2\psi_{cr}(s-1)gd}{f_w}} \tag{60}$$

If it is assumed that the sediment particles move at the same velocity of as the fluid the following expression will yield the instantaneous velocity of the sediment particles, u_b:

$$u_b = \begin{cases} u & \text{if } |u| > u_{cr} \\ 0 & \text{if } |u| < u_{cr} \end{cases} \tag{61}$$

By integrating the instantaneous velocity, the bead excursion length, ζ_b, can be obtained by:

$$\zeta_b = \int u_b \, dt \tag{62}$$

where the integral is evaluated over the entire duration of the wave. Since the particles are assumed to instantaneously accelerate from rest to the instantaneous fluid velocity and advect at the velocity of the fluid, estimates of the bead excursion length using the aforementioned method are conservatively high.

4.2.4 Modeling Subsurface Transport

This section outlines the methodology used to calculate the subsurface transport under a breaking wave. The theoretical model presented in *Madsen* (1974) is extended to account for dynamic effects.

4.2.4.1 Determination of the Bottom Pressure Distribution

Instead of assuming a linear pressure distribution, the actual pressure distribution of a breaking wave is estimated from velocity data. Utilizing an Acoustic Doppler Velocimeter (ADV), a velocity time series is obtained from the water column directly above the colored bead column of the sediment bed. Neglecting viscous effects, the momentum equation reads:

$$-\rho\frac{\partial p}{\partial x}=\frac{\partial u}{\partial t}+u\frac{\partial u}{\partial x}+w\frac{\partial u}{\partial z} \tag{63}$$

where u is x-orbital velocity, and w is z-orbital velocity. For the shallow water waves used in this study, the orbital wave velocities are nearly one dimensional, a fluid particle moves only in the plane of wave propagation. With this approximation, the last term in (63) can be neglected. See section 4.2.1 for more details about the shallow water wave approximation.

The phase velocity, c, of a breaking wave is not constant (see section 4.2.1). To make the following transformation the wave is assumed to be of permanent form as it passes over the test section. However, as the waves presented in this study are breaking and dissipating energy as they pass over the test section, this assumption is not entirely correct. However, we will assume change in phase velocity as the waveform passes the ADV to be negligible. With a constant phase velocity, the partial derivative with respect to x can be expressed in terms of the partial derivative with respect to t.

$$\frac{\partial u}{\partial x}=-\frac{1}{c}\frac{\partial u}{\partial t} \tag{64}$$

Substitution in Eqn. (63) yields:

$$-\rho\frac{\partial p}{\partial x}\approx\frac{\partial u}{\partial t}\left(1-\frac{u}{c}\right) \tag{65}$$

Using (65), an estimate of the pressure gradient can be obtained without the knowledge of the x and z velocities' spatial gradients. In the study presented by *Henderson et. al.* (2003), a mass conservation equation was used to approximate *w* and obtain an estimate for the last term in (63). However, the waves used in this study have a much larger equivalent wavelength than local water depth and therefore it is assumed that the shallow water approximation can be safely made.

Because the derivative of velocity is used, noise in the ADV's signal and turbulent fluctuations can lead to substantial errors when (65) is used to solve for the pressure gradient. In this study, the velocity time records are smoothed using *Matlab*'s built-in smoothing spline function utilizing a cubic spline interpolant to eliminate the high frequency variation in the data. A smoothing level of 0.999 was chosen to capture most of the main features of the velocity record while eliminating high frequency variations. Figure 22 depicts the smoothing level of a single realization of velocity for the solitary wave condition.

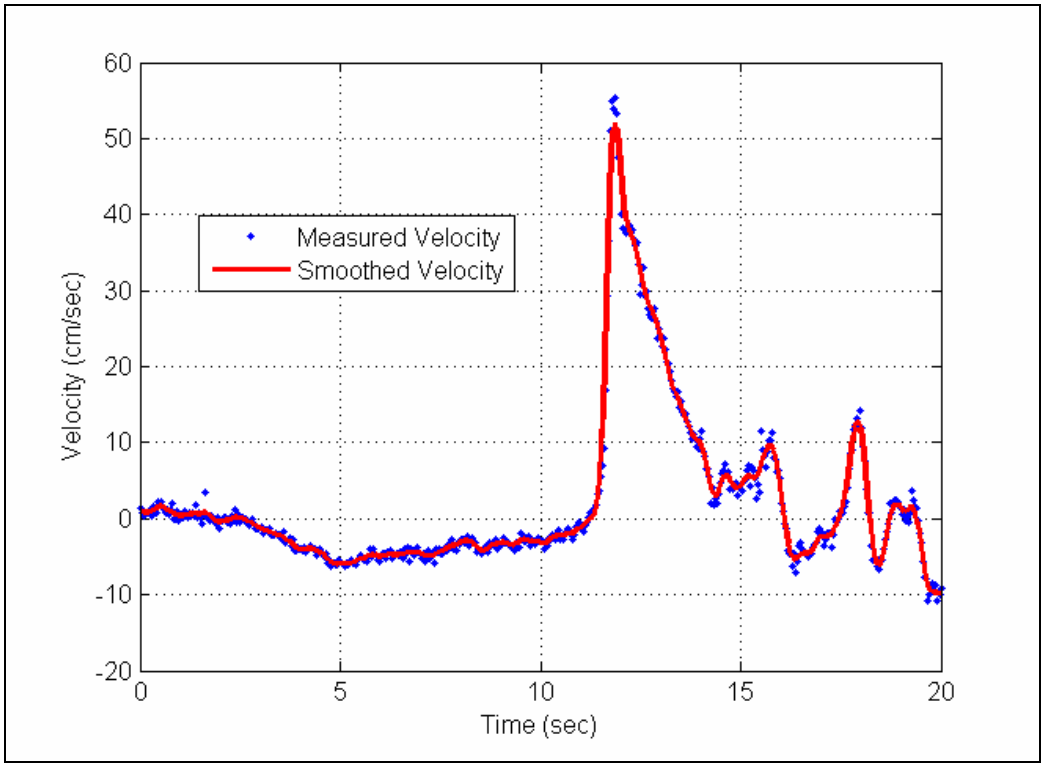

Figure 22 - Comparison of Measured and Smoothed Velocity Time Records

This process is repeated to obtain ten realizations of the same wave form. Next, each smoothed velocity record is differentiated with respect to time. The pressure gradient is estimated from the velocity record through the use of (65). The phase velocities used in (65) are obtained through a combination of measurement and theory. The ten pressure gradient realizations are then ensemble averaged using the highest point of the positive pressure gradient spike as a reference point.

It is noted that the peak velocity is somewhat diminished during the smoothing process, however, this smoothing level is necessary to obtain a reasonable measure of the velocity record's slope. Additionally, the smoothing is necessary to provide a consistent (uninfluenced by noise) point of reference by which the records can be ensemble averaged.

In Figure 23, the average of ten realizations of the pressure gradient for the solitary wave condition is shown by the solid line. The dashed lines above and below show one standard deviation from the average. A phase velocity of c = 148 cm/s is used to obtain the pressure gradient.

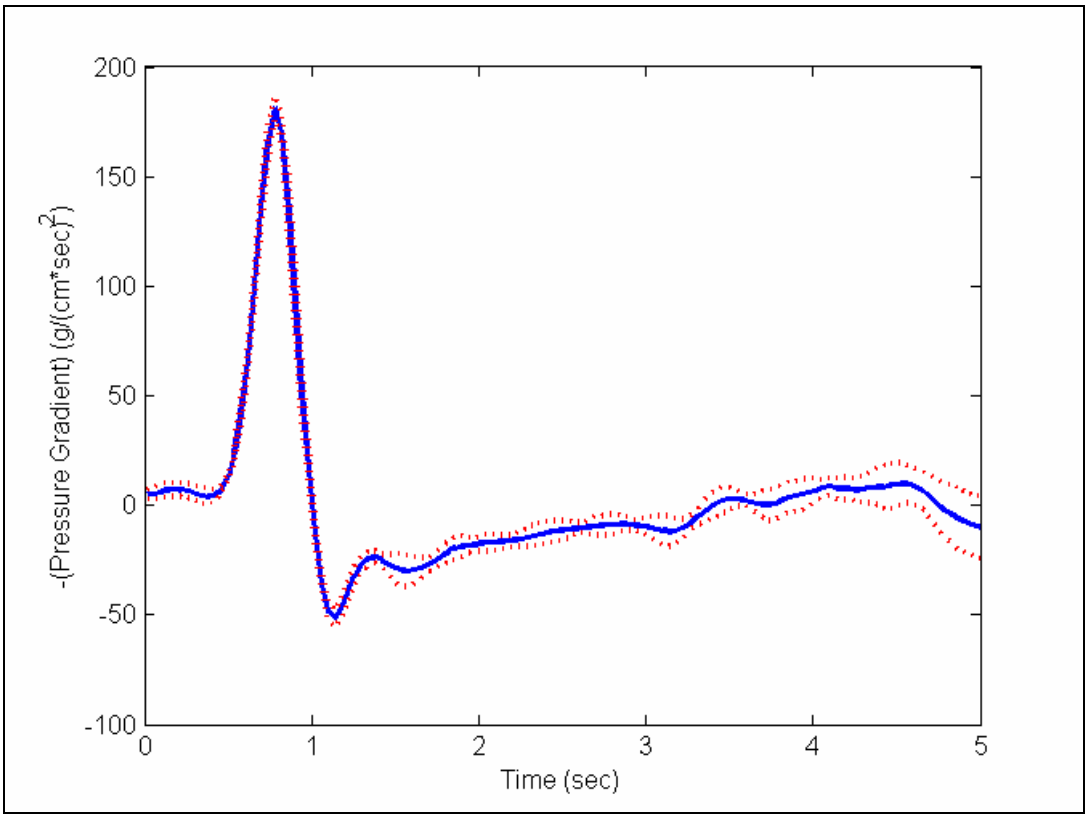

Figure 23 - Average Pressure Gradient Record with Standard Deviations

After the wave passage some choppiness is present in the signal, which can be seen by the increase in the standard deviation of the pressure gradient after the spike. Close to the spike there is little variation across the different realizations. Subsurface transport occurs at large values of the pressure gradient; the average pressure gradient represents an individual realization very well during this crucial period.

Analogous to Eqn. (64), the pressure gradient can expressed in terms of the partial derivative with respect to time:

$$\frac{\partial p}{\partial t} = -c\frac{\partial p}{\partial x} \tag{66}$$

This expression can then be integrated with respect to time to obtain the instantaneous pressure as a function of time.

$$p(t) = \int_0^t \frac{\partial p}{\partial t} dt \tag{67}$$

Integration is accomplished numerically using *Matlab*. The temporal domain is then transferred to the spatial domain using the transformation:

$$x = ct \tag{68}$$

such that the spatial pressure variation is obtained.

In Figure 24, the ensemble averaged pressure gradient and pressure distribution are plotted corresponding to the data presented in Figure 23. A phase velocity of c = 148 cm/s was used to generate these graphs.

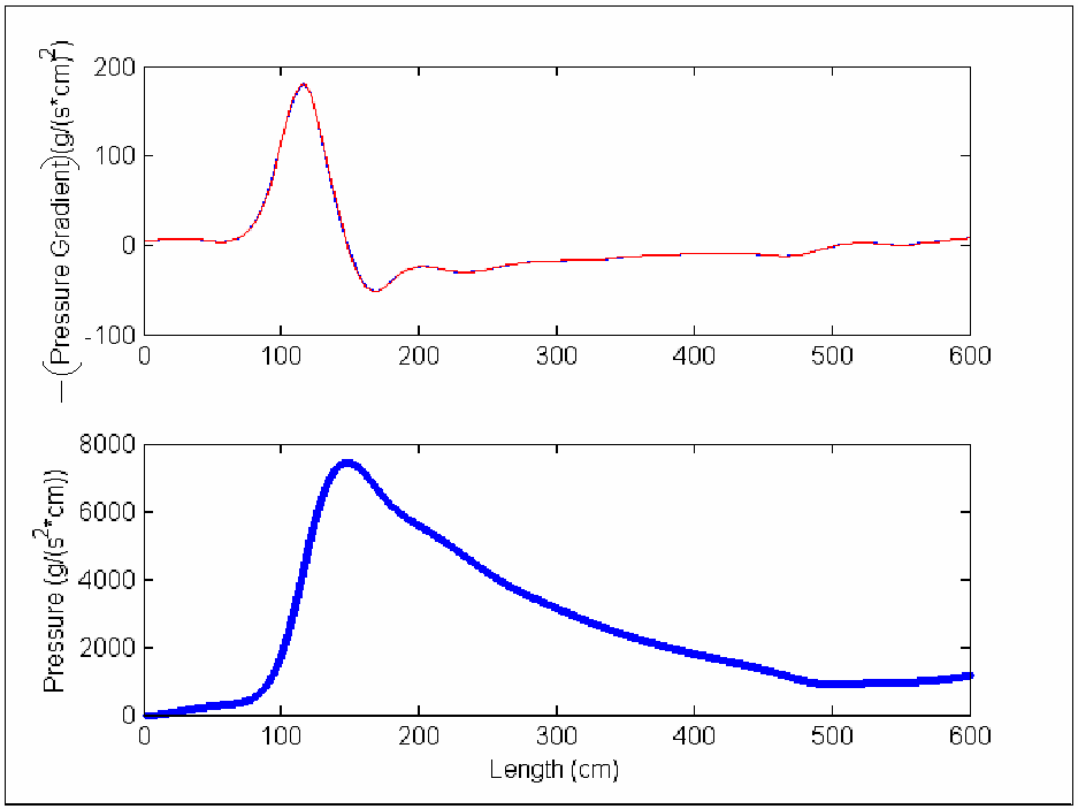

Figure 24 - Pressure Gradient and Pressure Distribution

4.2.4.2 Limiting Slip Circle Geometry

The ensemble-averaged pressure gradient is used to calculate the length over which failure occurs, $\ell_{s\max}$. The critical pressure gradient, above which a failure occurs in the sediment bed, is given by (2).

In Figure 25 the average pressure gradient is presented with the critical pressure gradient indicated by the dashed line. The record exceeding critical is shown in black. A friction angle of $\phi = 33^{\circ}$ and density of $\rho_t = 1.17$ g/cm^3 were used for the calculation of the critical pressure gradient.

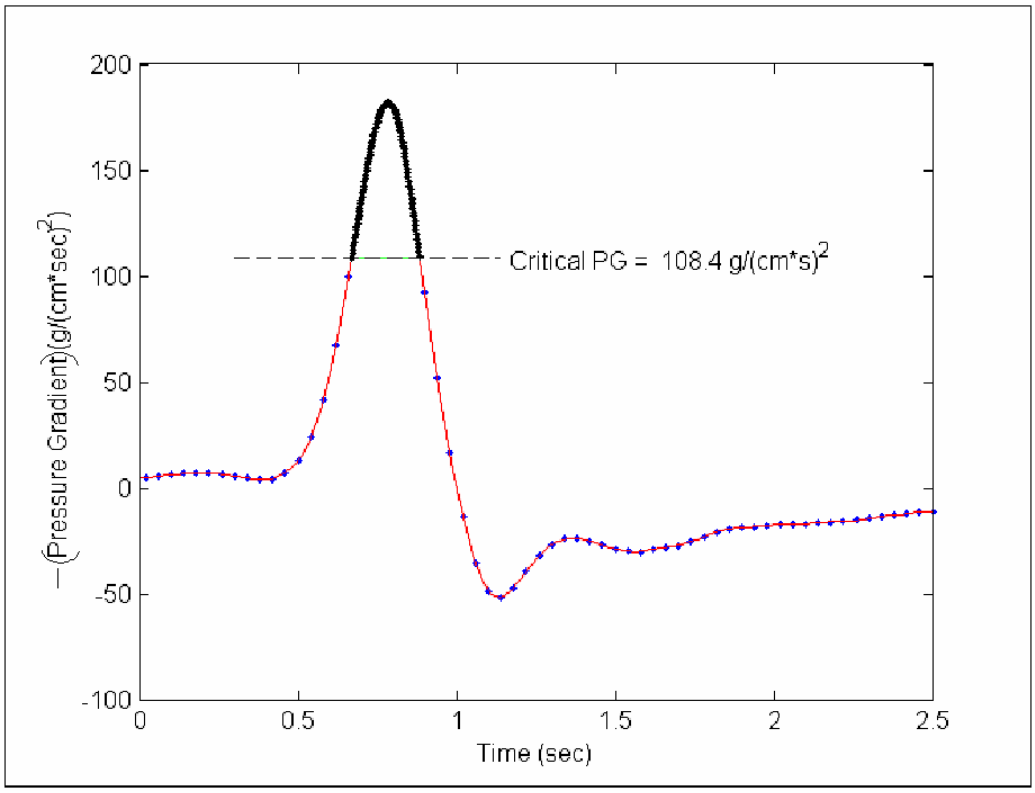

Figure 25 - Average Pressure Gradient

The amount of time which the critical pressure gradient is exceeded is multiplied by the phase velocity to obtain an estimate of $\ell_{s\max}$, the horizontal extent of the limiting slip circle. Figure 26 shows the notation used to denote the dimensions of the limiting slip circle.

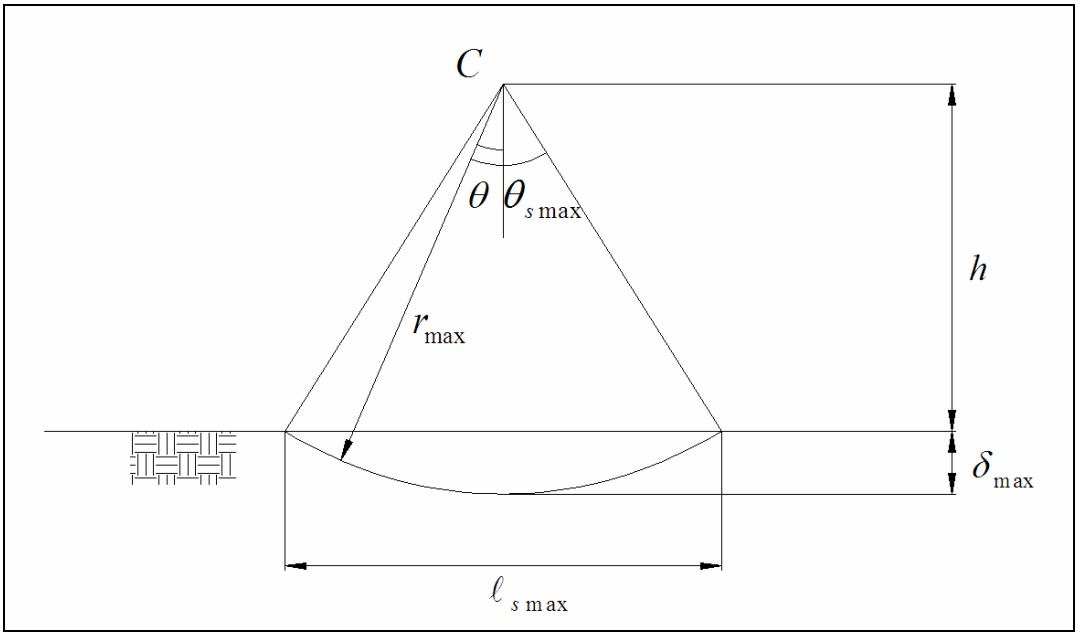

Figure 26 - Limiting Slip Circle Notation

The limiting slip circle defined as the bottom-most slip circle that models the failure plane below which no movement occurs. By definition, the limiting slip circle extends down to δ_{max} within the sediment bed. To find the maximum depth of disturbance, δ_{max}, the limiting slip circle's geometry must be found. The procedure is similar to that presented in *Madsen* (1974) except the driving moment about *C* is calculated using the measured bottom pressure distribution, instead of assuming a linear pressure distribution. In the limiting slip circle, the frictional moment about *C*, *Ms*, is equal to the maximum pressure induced driving moment about *C*, Md_{max}. With this relationship δ_{max} can be determined.

The wave pressure distribution, shown in Figure 24, is used along with $\ell_{s\,max}$ to resolve the driving moment record of the limiting slip circle using the following equation:

$$M(x_0) = \int_{-\ell_{s\,max}/2}^{\ell_{s\,max}/2} (x - x_0)\, p(x)\, dx \tag{69}$$

where x_0 is the coordinate of the midpoint of $\ell_{s\max}$. The convention for a right-handed coordinate system is used, where a positive moment is in the counter-clockwise direction.

To convert the moment record into a temporal domain, the moment record's spatial values are divided by the phase velocity to obtain the temporal discretization, *i.e.*

$$t = \frac{x_0}{c} \tag{70}$$

Figure 27 shows an example of a driving moment record in the temporal domain:

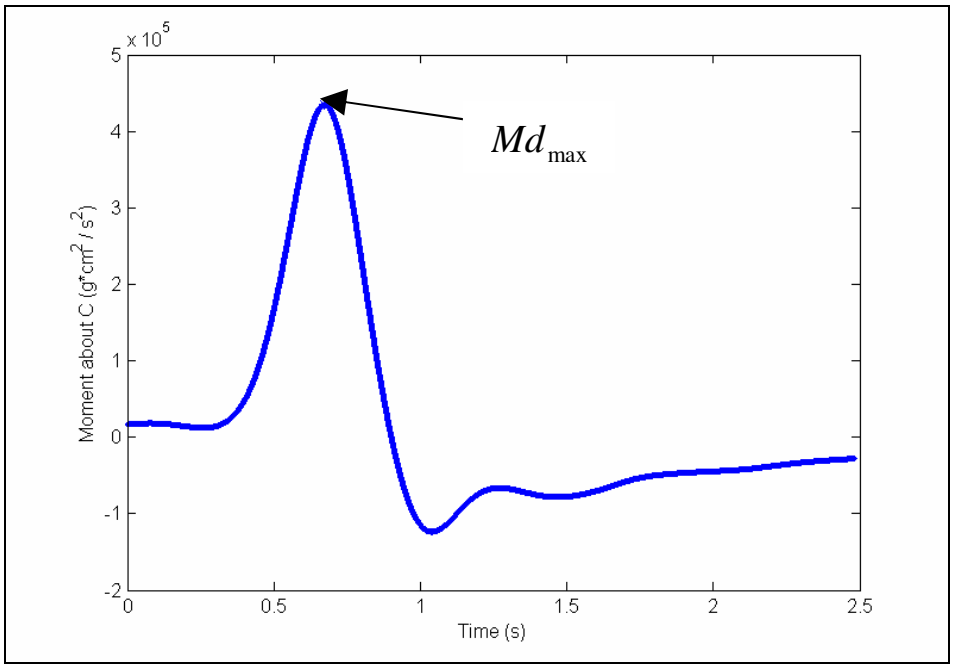

Figure 27 - Limiting Slip Moment Record

From this record the maximum driving moment, $Md_{\max}$, can be obtained. This value is equated to the frictional moment, Ms, using the formulation given in *Madsen* (1974). The angle, $\theta_{s\max}$, of the limiting slip circle is determined iteratively from (71) .

$$Md_{\max} = Ms = 2g(\rho_t - \rho)\tan\phi r_{\max}^{\ 3}\sin\theta_{s\max}(1 - \theta_{s\max}\cot\theta_{s\max}) \tag{71}$$

where r_{max} is given by (10).

The maximum depth of displacement is found using (11).

The height of *C* above the sediment bed, *h*, is calculated using:

$$h = \frac{\ell_{s\max}}{2\tan(\theta_{s\max})} \tag{72}$$

4.2.4.3 Slip Circle Geometry

To determine the movement of the sediment above the limiting slip circle a series of concentric slip circles are used. A pictorial description of the concentric slip circles is shown in Figure 28:

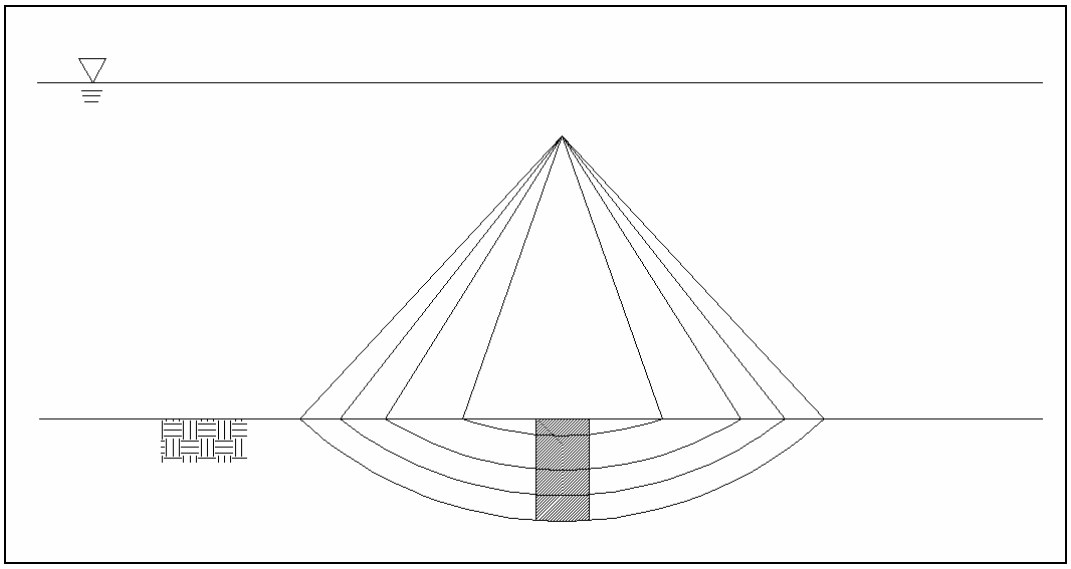

Figure 28 - Slip Circle Geometry

The geometry of the concentric slip circles above the limiting circle retain the *h* dimension of the limiting slip circle; or in other words, all slip circles rotate about C. The failure planes do not intersect and maintain a parallel alignment when rotating and hence, are kinematically allowable. Figure 29 shows the notation used to define the dimensions of a slip circle.

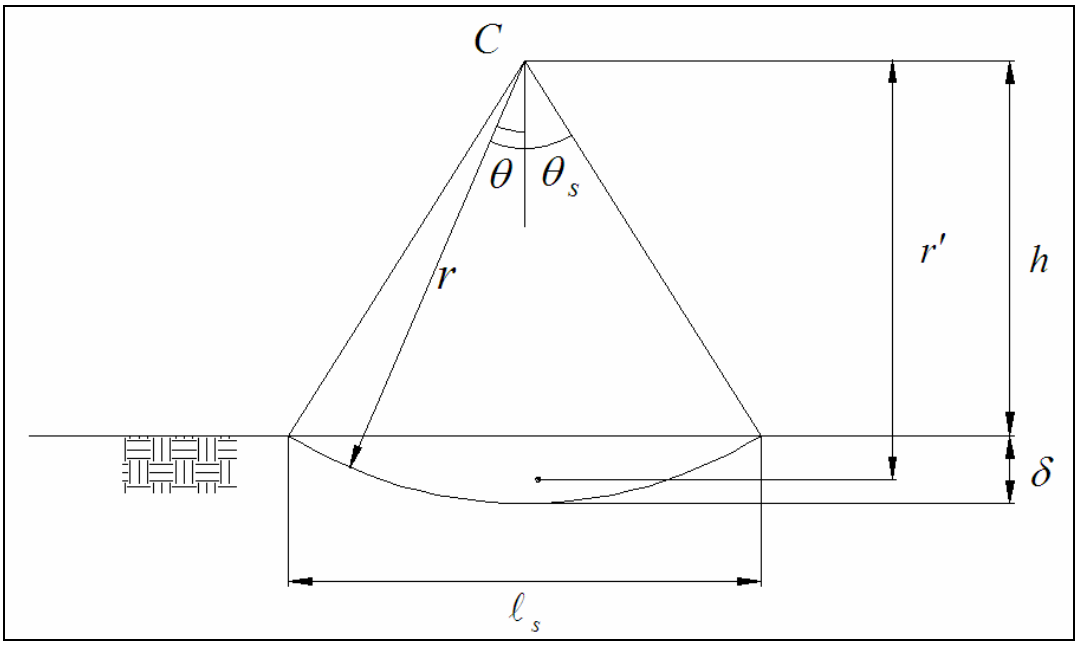

Figure 29 - Slip Circle Notation

Each slip circle models a failure plane located at *r*. The failure planes are spaced evenly by choosing depths, δ, between 0 and $\delta_{\max}$ at equal increments. Using the chosen δ, a slip circle's radius can be found using:

$$r = h + \delta \tag{73}$$

Additionally the angle, θ_s, horizontal extent, ℓ_s, the distance of the center of mass from the point of rotation, *r'*, the mass, *m*, and the radial mass moment of inertia, *I*, can be found using the following:

$$\theta_s = \arccos\left(\frac{h}{r}\right) \tag{74}$$

$$\ell_s = \frac{2\delta \sin\theta_s}{1-\cos\theta_s} \tag{75}$$

$$r' = \frac{4}{3}\frac{r\sin^3\theta_s}{(2\theta_s - \sin 2\theta_s)} \tag{76}$$

$$m = \frac{r^2\rho_t}{2}(2\theta_s - \sin 2\theta_s) \tag{77}$$

$$I = \frac{\mathrm{r}^4}{4}\left(2\theta_{\mathrm{s}}\text{-}\sin(2\theta_{\mathrm{s}}) + \frac{2}{3}\sin(2\theta_{\mathrm{s}})\sin^2\theta_{\mathrm{s}}\right)\rho_{\mathrm{t}} \tag{78}$$

The formulae for Eqns. (77) and (78) were obtained from Efunda (2006). The frictional moment is calculated using (8).

The temporal driving moment record is obtained for each slip circle using a method analogous to that of the limiting slip circle, using Eqn (69). The driving moment (solid lines) and frictional moment (dotted lines) records for 4 equally-spaced concentric slip circles are shown in Figure 30:

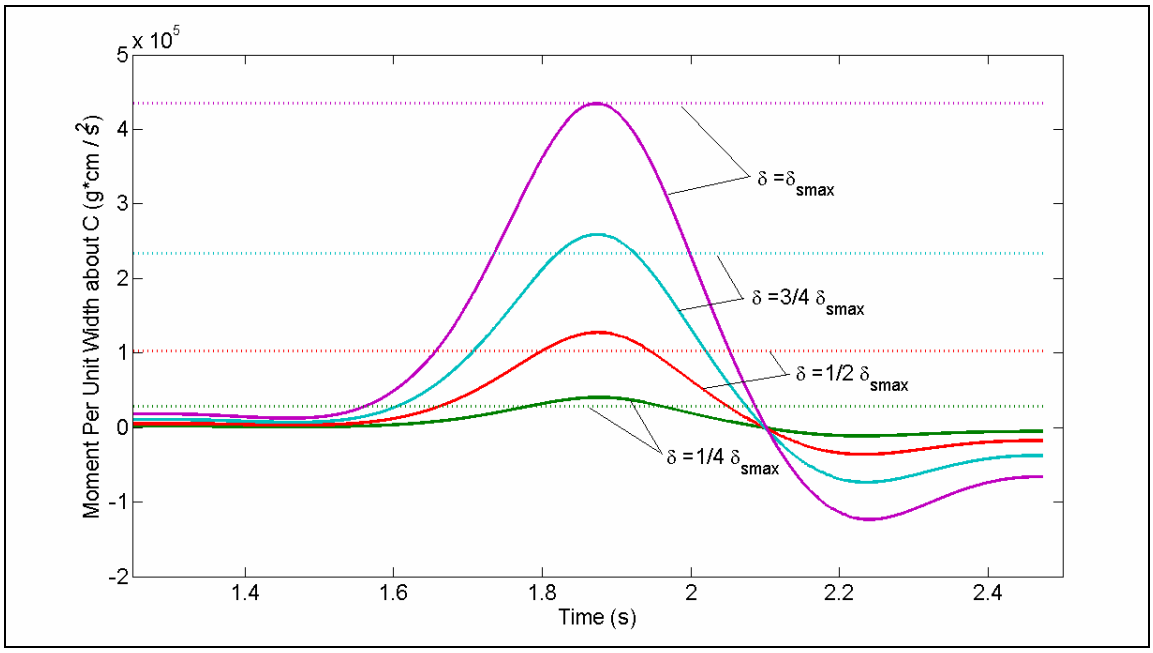

Figure 30 - Moments of Concentric Slip Circles

The first intersection of the driving moment and the frictional moment denotes the time at which the slip circles' begin to rotate. Note that in the limiting case the frictional moment is equal to the maximum driving moment. It can be seen that smaller slip circles initiate motion earlier than their larger counterparts.

To consider all the forcings that act upon a slipcircle, the moment produced by shear forces along the sediment-water interface, M_t, must be considered. These shear forces are responsible for surficial sediment transport. From the analysis provided in 4.2.2, the maximum shear stress that the sediment bed can sustain without surficial transport being initiated is related to the critical Shields parameter, ψ_{cr}. It is assumed that the maximum shear stress acting on the stationary sediment water interface is equivalent to the critical shear stress, τ_{cr}:

$$\tau_{cr} = \psi_{cr}(s-1)\rho g d \tag{79}$$

The maximum moment, $M_{t\max}$, that can be produced by this shear stress about *C*, is given by the expression:

$$M_{t\max} = \tau_{cr}\ell_s h \tag{80}$$

If the surficial shear stress is below critical, $(\tau < \tau_{cr})$, a moment smaller that $M_{t\max}$ will be generated. Neglect of M_t in the calculation a slipcircle's subsurface movement can be justified if:

$$M_{t\max} \ll Md_{\max} \tag{81}$$

where $Md_{\max}$ is the maximum driving moment induced by pressure. Because of differences in the way the two moments scale, the proportion, $\frac{M_{t\max}}{Md_{\max}}$, gets larger as the depth of the

slipcircles' failure plane goes to zero. However, $M_{t\max}$ remains small relative to $Md_{\max}$ for depths on the same order of magnitude as a bead diameter. For the conditions present in experiments with the solitary wave and PET beads ($\psi_{cr} = 0.0334$, d = 0.11cm, s = 1.27, $\phi = 33^{\circ}$), a slipcircle with failure plane that extends $\delta = 0.17\text{cm}$, less than two bead diameters, beneath the sediment water interface yields :

$$\frac{M_{t\max}}{Md_{\max}}(100\%) \simeq 5\% \tag{82}$$

Clearly, even at depths for which the calculation of the subsurface sediment movement is not practical, the pressure driven moment, Md, dominates the shear stress driven moment M_t. In this study the effects of the shear stress induced moment is neglected.

4.2.4.4 Calculation of Subsurface Transport

To model the rotation of each slip circle we will use the same formulation used to describe the motion of a pendulum. The governing equation of a pendulum with small amplitude oscillations is:

$$I\ddot{\Theta}(t) + mgr'\Theta(t) = F(t) \tag{83}$$

where $\ddot{\Theta}$ is the pendulum's angular acceleration, Θ is the pendulum's angular position, and F is the forcing moment.

To find a governing equation that effectively relates pendulum motion (83) to the motion of an individual slip circle it must be taken into account that the slip circles' movements are coupled. When solving a slip circle's motion, the motion of the slip circle above it must be considered.

Figure 31 depicts two concentric slip circles and the notation used for the relative motion analysis.

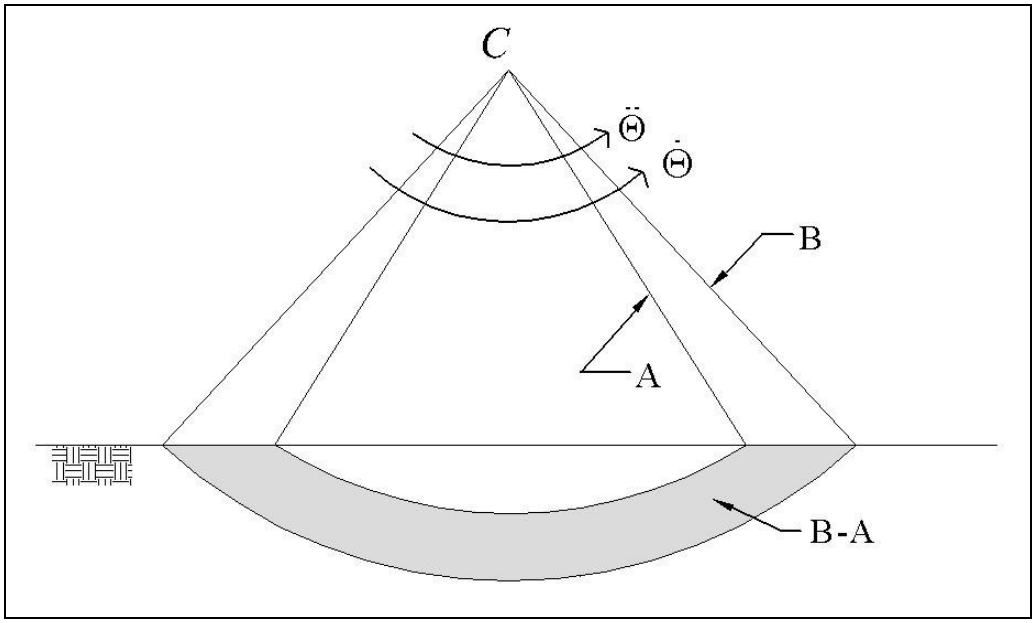

Figure 31 - Relative Slip Circle Motion Analysis

To determine the motion of slip circle B, the equation of motion of slip circle A is first formulated. Slip circle A is considered the uppermost slip circle in this idealized scenario. The governing equation for slip circle A is:

$$I_A\ddot{\Theta}_A(t) + m_A g r'_A \Theta_A(t) = Md_A(t) - Ms_A \tag{84}$$

where the two terms on the right hand side are the forcing.

To determine the governing equation for slip circle B, the motion of A relative to B must be accounted for. A formulation similar to that used for slip circle A is used with the addition of two terms that incorporate the moment produced by the movement of A relative to B. For segment B:

$$I_B\ddot{\Theta}_B(t)+I_A\left(\ddot{\Theta}_A(t)-\ddot{\Theta}_B(t)\right)+m_Bgr_B'\Theta_B(t)$$
$$+m_Agr_A'\left(\Theta_A(t)-\Theta_B(t)\right)=Md_B(t)-Ms_B \tag{85}$$

which can be rearranged to read:

$$\left(I_B-I_A\right)\ddot{\Theta}_B(t)+m_Bgr_B'\Theta_B(t)+g\left(m_Br_B'-m_Ar_A'\right)\Theta_B(t)$$
$$+I_A\ddot{\Theta}_B(t)+m_Agr_A'\Theta_A(t)=Md_B(t)-Ms_B \tag{86}$$

The last two terms on the right hand side can be substituted for using (84) to yield:

$$\left(I_B-I_A\right)\ddot{\Theta}_B(t)+g\left(m_Br_B'-m_Ar_A'\right)\Theta_B(t)$$
$$=\left[Md_B(t)-Md_A(t)\right]-\left[Ms_B-Ms_A\right] \tag{87}$$

which can easily be verified as the equation of motion for the annulus labeled B-A in Figure 31.

If the relative movements of the two slip circles are small compared to B's absolute movements:

$$\left|\ddot{\Theta}_A-\ddot{\Theta}_B\right|\ll\left|\ddot{\Theta}_B\right| \tag{88}$$

$$\left|\Theta_A-\Theta_B\right|\ll\left|\Theta_B\right| \tag{89}$$

and the characteristics of the two slip circles are approximately equal:

$$I_A\simeq I_B \tag{90}$$

$$m_A\simeq m_B \tag{91}$$

$$r_A'\simeq r_B' \tag{92}$$

then Eqn. (85) reduces to:

$$I_B\ddot{\Theta}_B(t)+m_Bgr_B'\Theta_B(t)=Md_B(t)-Ms_B \tag{93}$$

The last term, the frictional moment, will always have a sign opposite to that of the relative velocity between slip circle B and the slip circle directly beneath. This is because the friction

occurs on the failure plane between the two concentric slip circles. Figure 32 shows the slip circles' motion as a wave passes overhead:

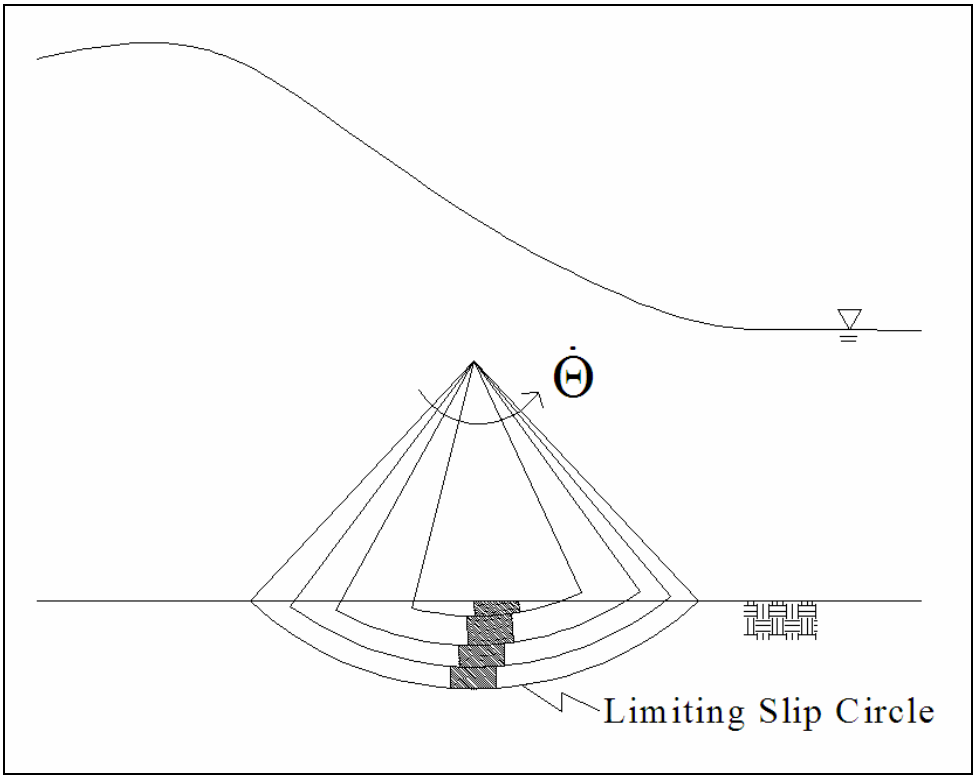

Figure 32 - Displacements of Slip Circles

To solve (93) for each slip circle, two methods were utilized. One method uses *Matlab*'s suite of numerical ODE solvers. The second method fits the driving moment with a polynomial and solves the expression analytically.

4.2.4.4.1 Solving for Subsurface Displacement Numerically

Solving (93) numerically is a difficult task. With Coulomb friction, the frictional moment changes sign when the relative angular velocity changes sign. This leads to a very stiff condition when the slip circle comes to a stop. Compared to the other solvers in the suite, the script *ode15s.m* was found to yield the best results because of its ability to handle stiff systems with

good efficiency. Since this solver is only designed to handle first order ODEs, a reduction of order technique was utilized.

Numerical ODE solvers such as *ode15s* use an adaptive time step that decreases the time step whenever a large change in the forcing is encountered. It will attempt to resolve the system's response to the discontinuity by solving the ODE on either side of the discontinuity. When the velocity of the slip circle changes direction and eventually comes to rest the solver has a difficult time resolving the zero angular velocity due to the discontinuity in the frictional moment. The solver shortens the time step to a very small quantity and the computation no longer becomes effective. When the solver reduces the time step to a specified quantity without achieving the desired tolerances the computation is ceased. By reducing the order of *ode15s* from five to one, the solver can sometimes actualize a zero velocity, but produces results nearly identical results to the 5^{th} order solver whose computation was terminated.

A series of logic gates were developed to pass the correct forcing to the *ode15s* program for each time step. Two different techniques were used to calculate the sign of the frictional moment. The first technique begins solving for the motion of the slip circle above the limiting slip circle and advances one slip circle at a time towards the sediment-water interface, using the underlying slip circle's stored velocity record to calculate the relative velocity. Using for reference slip circles (A) and (B) denoted in Figure 31, the angular velocity time series of B is fitted with a cubic spline (no smoothing) after its motion has been calculated. To determine the motion of (A), the stored velocity record of (B) is used to calculate the relative velocity $(\dot{\Theta}_A - \dot{\Theta}_B)$ at each time step. This process is repeated until the motion of the upper-most slip circle is found. A zero velocity record is stored for the limiting slip circle when calculating the motion of the slip circle

directly above it. This technique proves to be very expensive computationally and sometimes results in computational errors. This technique must be used with a 1st order solver to obtain results in reasonable amount of time.

The second technique exploits the fact that a slip circle usually moves at an angular velocity higher than that of the slip circle that encompasses it yielding a positive relative velocity. When the relative velocity becomes negative it usually has a very low magnitude compared to the absolute angular velocity of either slip circle. When the relative velocity is negative, the inner slip circle will likely just travel at the same angular velocity as the slip circle which encompasses it. Using this assumption the displacements can be found with relative ease.

4.2.4.4.2 Solving For Subsurface Displacement Analytically

The second method solves (24) by fitting the driving moment with a polynomial using a least squares regression and then evaluates the resulting equation analytically. The relative velocity, $(\dot{\Theta}_A - \dot{\Theta}_B)$, is assumed to be positive at all times. The slip circle is assumed to come to rest when its angular velocity reaches zero for the first time. To accurately represent the driving moment, a 9th order polynomial is used. The program *Maple* is used to solve equation (93) analytically for $\ddot{\Theta}, \dot{\Theta}, \text{and } \Theta$ in terms of the slip circle characteristics and polynomial coefficients of the fitted driving moment. The time values of the moment record are adjusted to begin at zero when the driving moment first exceeds the frictional moment. This is necessary in order to determine which of the angular velocity zero-crossing represents the final resting place of the slip circle.

Figure 33 shows the analytical solutions for angular velocity and angular position for a typical slip circle. The red asterisk denotes the final position of the slip circle (zero angular velocity).

Figure 34, Figure 35, and Figure 36 show the final displacements of the slip circles as a function of depth. Results are for solitary wave condition. Three different friction angles are shown. The numerical solution is presented in blue, the analytical in red.

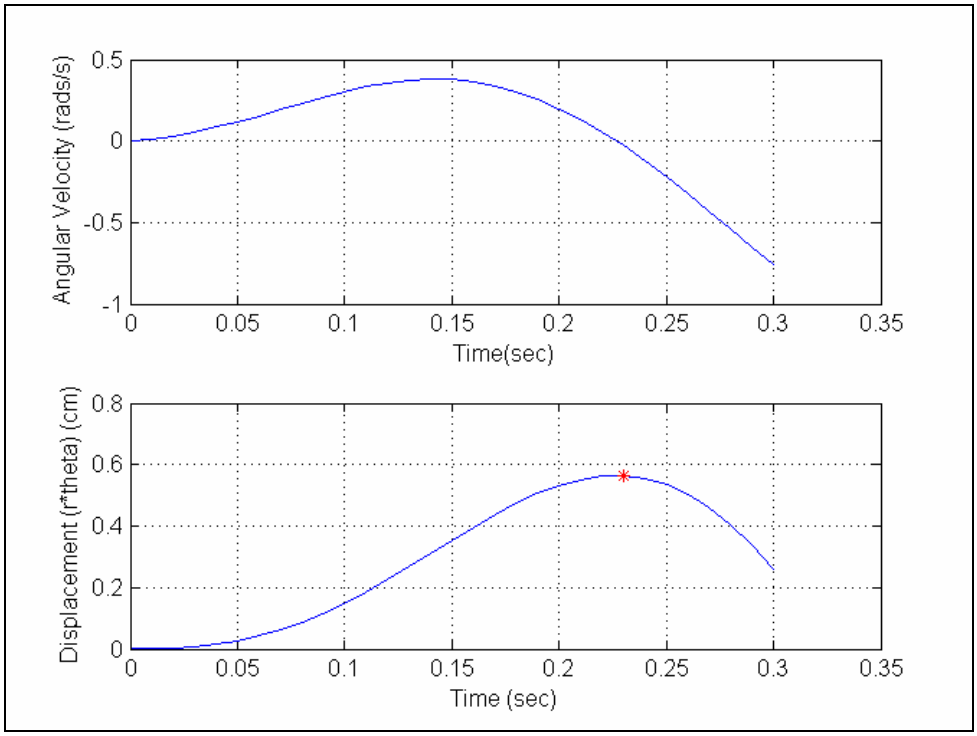

Figure 33 - Angular Velocity and Angular Position Records Obtained Analytically

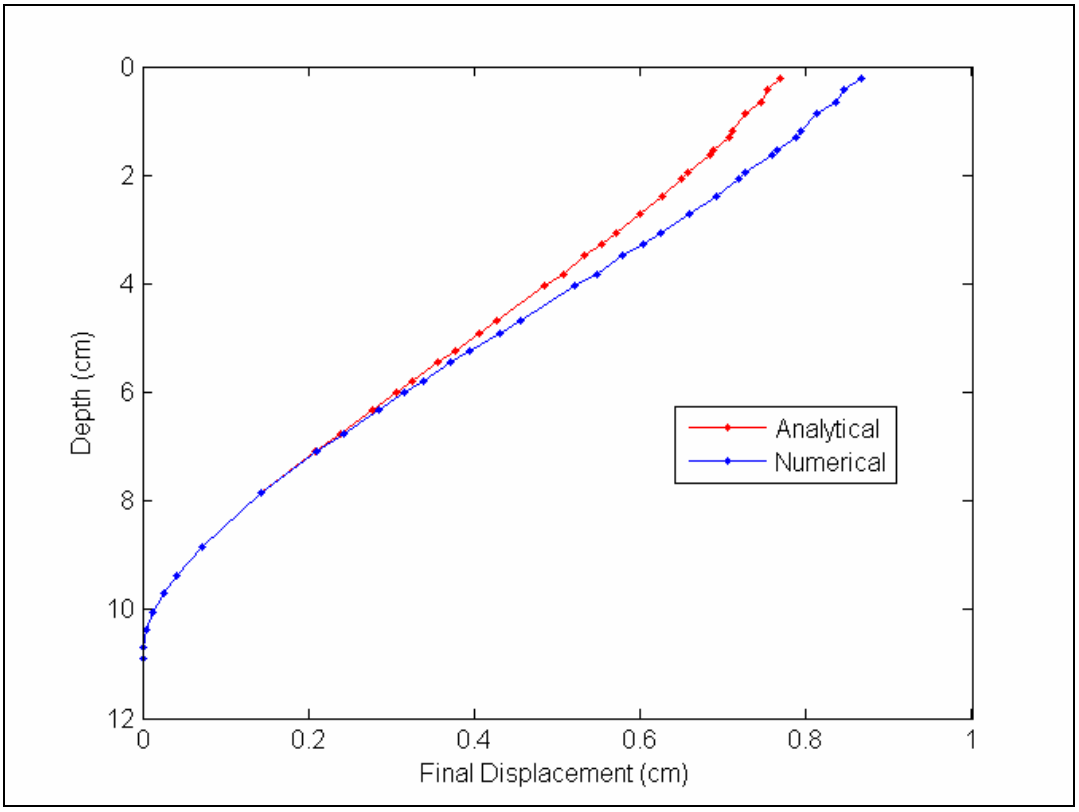

Figure 34 - Final Displacements for $\phi = 30^{\circ}$

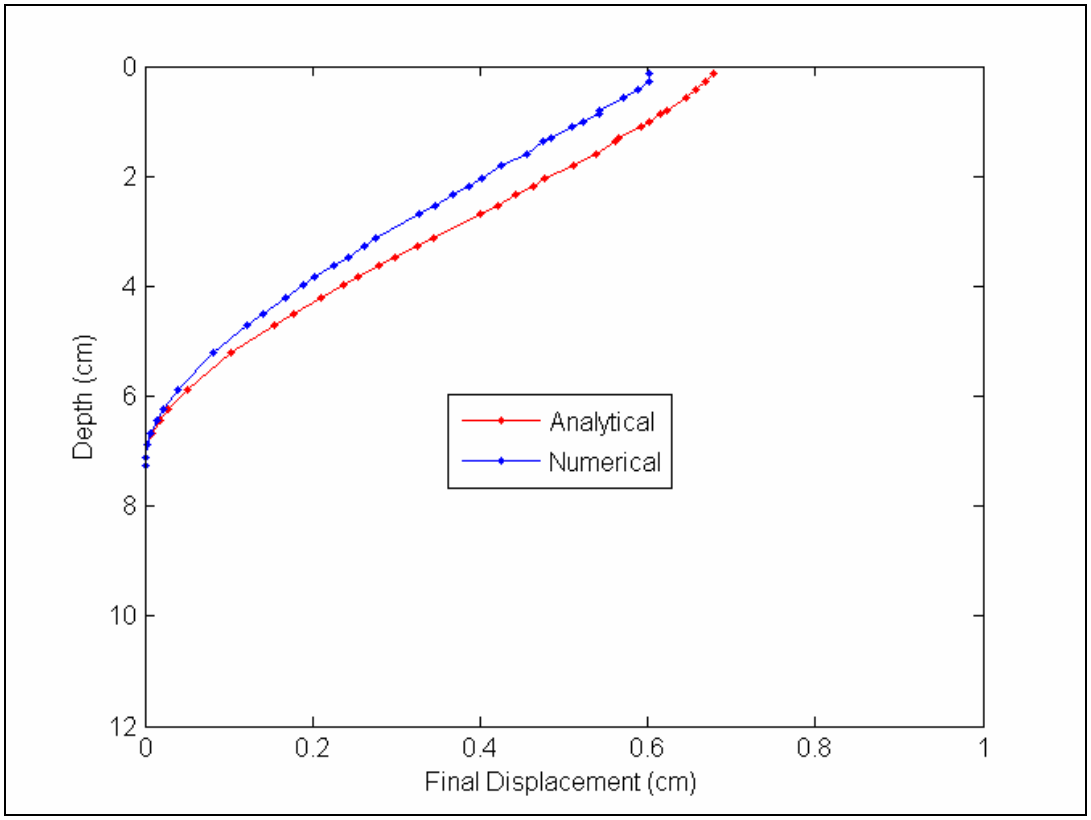

Figure 35 - Final Displacements for $\phi = 35^{\circ}$

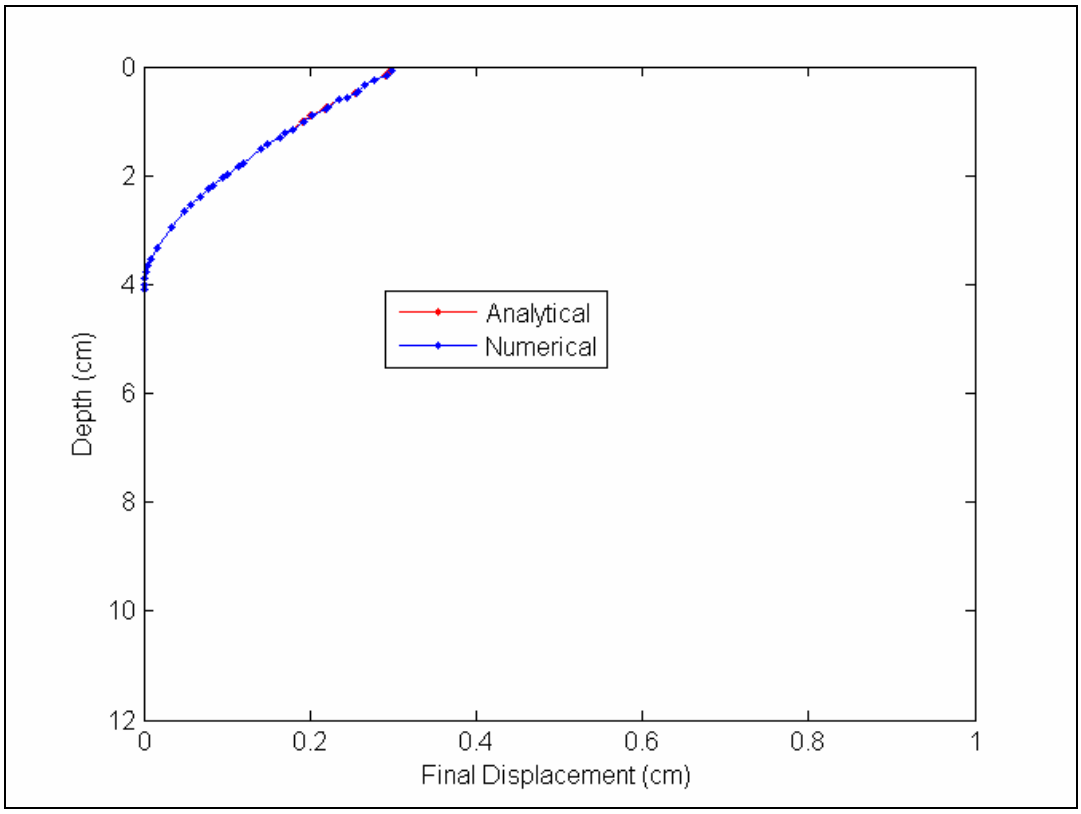

Figure 36 - Final Displacements for $\phi = 40^{\circ}$

Both the analytical and numerical solutions give similar results, but there is no clear pattern to predict which solution method will yield a higher estimate of subsurface transport.

It can be seen that an increase in the internal angle of friction leads to smaller depths of disturbances and displacements. The depth of disturbance and displacement clearly does not follow a linear trend with internal angle of friction. As a the friction angle approaches a limiting value in which the critical pressure gradient defined by (2) is equivalent to the highest pressure gradient in a given wave condition the predicted subsurface transport will decrease rapidly.

4.2.5 Predictions of Transport Using Data from *Madsen* (1974)

To properly scale laboratory wave conditions to the size of that typically found in the field the ratio of the relevant forces present in the both the model (laboratory) and prototype (typical field conditions) must be preserved. The two dominant forcings in gravity water waves are inertia and gravity. The dimensionless Froude number, *Fr*, relates these two forcings:

$$Fr = \frac{u}{\sqrt{gL}} \tag{94}$$

where *L* is the relevant length dimension. To maintain dynamic similarity, the Froude number must be equivalent in both the model and the prototype. Scaling factors are used to obtain the prototype wave condition. These scaling factors prescribe the prototype wave condition's parameters as a ratio of the model wave condition's parameters. Each variable (length, velocity, pressure, pressure gradient) has a separate scaling ratio that preserves the Froude number similarity in the model and prototype. The length scaling ratio, *Lr*, is defined as:

$$Lr = \frac{L_p}{L_m} \tag{95}$$

where L_p is the length of a prototype geometric feature and L_m is the length of a model geometric feature. Essentially, the geometric dimensions of the model wave (wave height, wavelength, etc.) are multiplied by the scaling factor to obtain the respective prototype wave dimension. The velocity scaling factor, *Vr*, is:

$$Vr = \frac{V_p(t)}{V_m(t)} = \sqrt{Lr} \tag{96}$$

where $V_p(t)$ is the prototype velocity record and $V_m(t)$ is the model velocity record. The pressure gradient scaling factor, PGr, is given as:

$$PGr = \frac{PG_p(t)}{PG_m(t)} = 1 \tag{97}$$

where $PG_p(t)$ is the pressure gradient record of the prototype and $PG_m(t)$ is the pressure gradient record of the model. The pressure gradient record of the model is the equal to the pressure gradient record of the prototype. The time scaling factor, *Tr*, is:

$$Tr = \frac{T_p}{T_m} = \sqrt{Lr} \tag{98}$$

where T_p is the prototype's temporal record and T_m is the model's temporal record. The time scaling factor is used in this study to correlate the time domain of the velocity and pressure gradient record of the model to the time domain of the prototype.

For a typical sand sediment bed in the ocean ($\rho_s = 2.65$ g/cm^3, $\rho = 1.03$ g/cm^3, $\phi = 32^\circ$, n = 0.35) equation (2) gives a critical pressure gradient of $\left(\frac{\partial p}{\partial x}\right)_{cr} = 645$ g/(cm s)^2. Because the pressure gradient scales by one, the pressure gradient records of the solitary and three wave burst wave conditions (both with a maximum pressure gradient of $\left(\frac{\partial p}{\partial x}\right)_{\max} < 200$ g/(cm s)^2) will not induce failure for typical sandy sediment beds at any length scale.

Madsen (1974) presents a differential pressure record for the wave condition used in his experimental investigation. An estimate of the pressure gradient record can be found by dividing the differential pressure record by the distance between the two pressure taps. A maximum pressure gradient of $\left(\frac{\partial p}{\partial x}\right)_{\max} \approx 770$ g/(cm s)^2 is obtained, sufficient to induce a failure over a sandy bed. It is likely that *Madsen* (1974) was able to achieve larger pressure gradient because

his wave condition breaks on a 1:10 slope. For the wave conditions presented in this study, breaking is triggered by a slope but actually occurs in the constant depth portion of the test section.

Madsen (1974) made measurements of the water surface level concurrently with the measurements of the bottom pressure difference between the two taps . Measurements were made at a still water depth of 13 cm. A long period surge of roughly T = 5.2s developed in the flume after steady state conditions were reached. This slowly-varying surge caused the waves to break in different manners. Both spilling and plunging waves were observed. Figure 37 shows diagrams of both spilling and plunging waves.

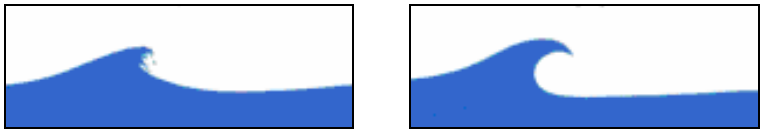

Figure 37 – Types of Breaking Waves
diagrams from: Surf Lifesaving Queensland (2004)

Spilling waves are characterized by a steep front face which the fluid "spills" down during breaking, creating a turbulent crest. Plunging waves are characterized a tongue which curls over and falls forward. *Madsen* (1974) found that spilling waves produced the largest pressure gradient.

To calculate subsurface transport using the methods described in section 4.2.4, the pressure gradient record presented in *Madsen* (1974) must be smoothed to eliminate high frequency noise. Figure 38 shows the smoothing level used to obtain a reasonable estimate of the pressure gradient. The pressure gradient obtained from *Madsen* (1974) is shown in blue and the smoothed record is shown in red. The breaking wave is of the spilling type. A critical pressure gradient

typical for sandy sediment beds ($\left(\frac{\partial p}{\partial x}\right)_{cr} = 645$ g/(cm s)^2) is shown in green. The smoothed record exceeding critical is shown in black.

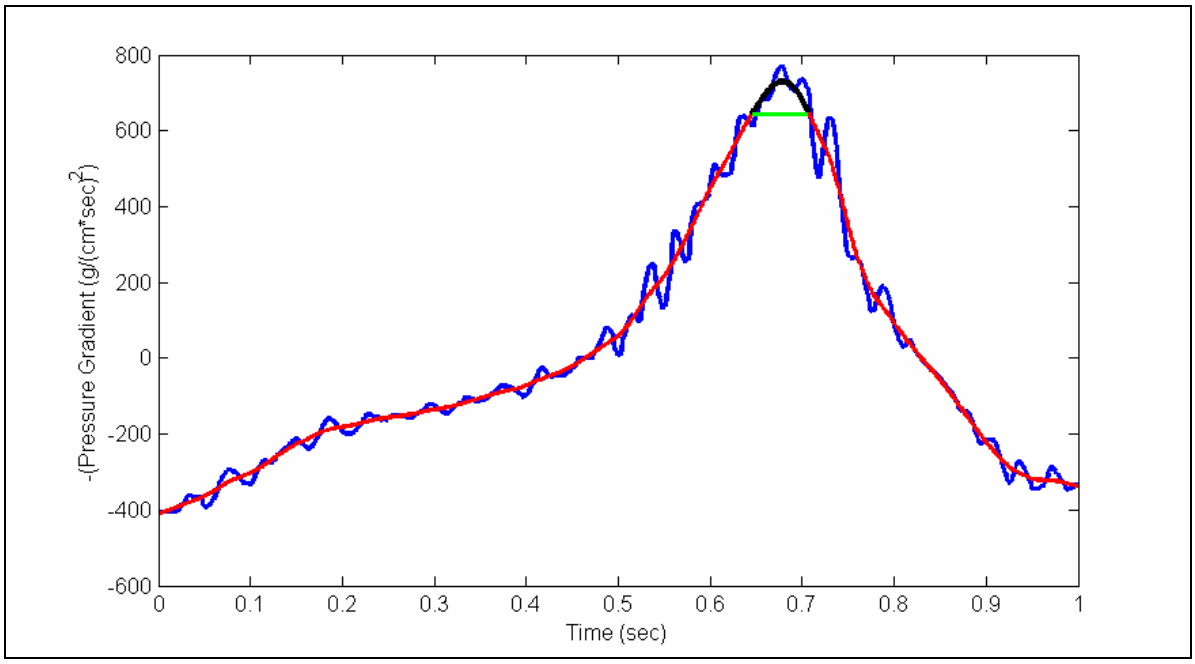

Figure 38 – Smoothed Pressure Gradient Obtained from *Madsen* (1974)

The critical pressure gradient is only exceeded for a short period (~ 0.1s). If the friction angle is increased from $\phi = 32^\circ$ to approximately $\phi = 37^\circ$ (keeping the other variables constant) no subsurface sediment failure would occur.

Madsen (1974) provides a record which contains both a spilling and plunging wave, in succession. The long period surge (T = 5.2s) must be accounted for in the determination of the water depth at the location which measurements are made. By integrating the water surface deviation from the mean water level over two complete wave periods (T = 0.95s), the approximate effect of the long period surge can be estimated. To satisfy mass conservation the integrated value over the two wave periods must be zero. It was found that adding an offset of +1.8cm to the wave gauge record allows continuity to be satisfied. This offset is essentially the

deviation of the average mean water level during the two wave periods from the still water level (h = 13cm). This adjustment is approximate as the duration of the two wave periods (1.9s) is not a small quantity compared to the long period surge (T = 5.2s).

Madsen (1974) estimated a phase velocity of c = 44 cm/s for this wave condition using the bottom pressure records, however, this measurement appears very low. Using a recalibrated water depth of h = 11.2cm, linear theory yields a phase velocity of $c_l = 96.7$ cm/s and wavelength of L = 91.9cm. This wave does not meet the shallow water criterion:

$$\frac{h}{L} = \frac{11.2\text{cm}}{91.9\text{cm}} = 0.122 > 0.05 \tag{99}$$

Madsen (1974) related spatial and temporal derivatives of pressure to obtain the phase velocity of c = 44 cm/s, however, pressure records for a breaking wave are expected to be highly erratic. This estimate of the phase velocity is likely to contain some error. To obtain the subsurface transport, a range of phase velocities will be used to account for the variability in the theoretical and experimental estimates.

The pressure gradient record shown in Figure 38 is scaled to provide estimates of the subsurface transport for a variety of different length ratios. The methodology described in section 4.2.4 is used to calculate subsurface transport with one exception. The pressure gradient data is obtained directly from differential pressure transducer data, instead of estimating from velocity records.

Water surface elevation records, measured concurrently with pressure difference record, are used to obtain estimates of the spilling wave's velocity record. The following relationship relates the water surface deviation from mean water level, $\eta(t)$, to the wave's horizontal velocity, $u(t)$:

$$u(t) = \frac{\eta(t)}{(h(t)+\eta(t))}c \tag{100}$$

Unlike the pressure gradient data record, wave gauge data contains little high frequency noise, very little smoothing is required. The upper graph in Figure 39 shows the water surface record, $\eta(t)$, for the spilling wave from *Madsen* (1974). The data has been adjusted to satisfy mass continuity by adding an offset of +1.8cm. The lower graph in Figure 39 shows the velocity record, *u*(*t*), obtained through the use of (100) with a phase velocity of $c_l = 96.7$ cm/s.

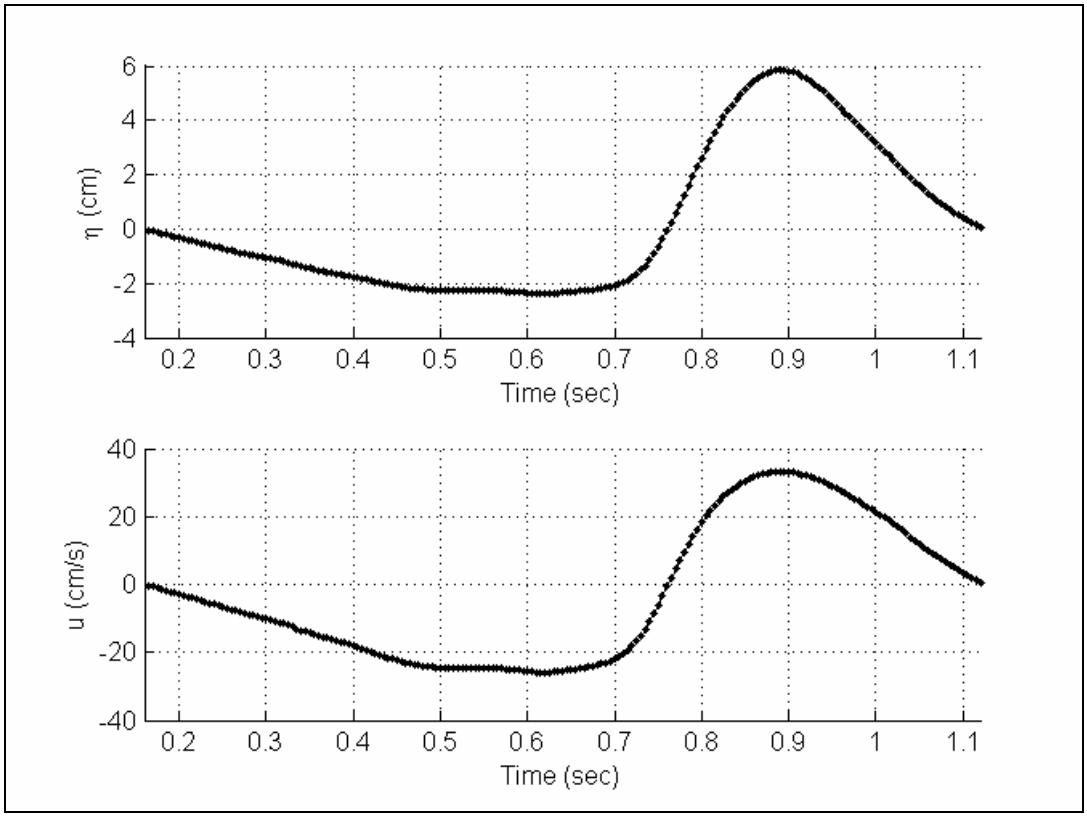

Figure 39 – Wave Gauge Data from *Madsen* (1974) and Velocity Record Obtained from (100)

It can be easily seen from these records that the model wave is both asymmetric and skewed. Using the methodology outlined in section 4.2.2.2 the theoretical surficial transport can be estimated.

5 - RESULTS

5.1 PHASE VELOCITY

5.1.1 Three Wave Burst

The following results were obtained experimentally for the three wave burst condition. The two wave gauges are separated by a distance of $\Delta L =$ 96.5 cm. The midpoint between the two wave gauges was placed at the center of the test section. The phase velocity for each of the waves was calculated using both the maximum wave height and the maximum water surface slope as reference points. The results are presented in Table 7.

The first of the three waves yields relatively similar phase velocities for both reference points. The second wave yields a phase velocity ~ 7% larger when using the maximum water surface slope as a reference. This discrepancy can be expected as the wave is not of permanent form, each part of the breaking wave is traveling at a different speed. The third wave's record is somewhat erratic. It is believed that reflections within the wave flume affect the third wave as it propagates over the test section. For transport calculations the first of the three waves' record will be used.

Table 8 shows the maximum wave height recorded for each of the three waves. The wave heights were measured with two wave gauges in the same positions as during the measurement of the phase velocities. Both the upwave and downwave measurements are shown.

Table 7 – Experimentally Measured Three Wave Burst Phase Velocities

Using Maximum Water Surface Slope	
Δt (sec)	c (cm/s)
First Wave in Burst	
0.64	150.8
0.6	160.8
0.68	141.9
Average	151.2
Std Dev	9.5
Second Wave in Burst	
0.56	172.3
0.56	172.3
0.56	172.3
Average	172.3
Std Dev	0.0
Third Wave in Burst	
0.52	185.6
0.8	120.6
0.48	201.0
Average	169.1
Std Dev	42.7

Using Maximum Wave Height	
Δt (sec)	c (cm/s)
First Wave in Burst	
0.64	150.8
0.64	150.8
0.64	150.8
0.68	141.9
Average	148.6
Std Dev	4.4
Second Wave in Burst	
0.6	160.8
0.6	160.8
0.6	160.8
0.64	150.8
Average	158.3
Std Dev	5.0
Third Wave in Burst	
0.68	141.9
0.72	134.0
0.68	141.9
Average	139.3
Std Dev	4.6

Table 8 – Experimentally Measured Three Wave Heights

	Downwave of Test Section		Upwave of Test Section
	H (cm)		*H* (cm)
	First Wave in Burst		First Wave in Burst
	9.8		10.4
	9.8		10.1
	9.8		10.3
	9.8		9.5
Average	9.8	Average	10.1
Std Dev	0.0	Std Dev	0.4
	Second Wave in Burst		Second Wave in Burst
	9.8		9.1
	9.8		9.0
	9.8		9.7
	9.8		10.4
Average	9.8	Average	9.5
Std Dev	0.0	Std Dev	0.6
	Third Wave in Burst		Third Wave in Burst
	3.4		2.3
	3.8		2.5
	3.8		2.6
Average	3.7	Average	2.5
Std Dev	0.2	Std Dev	0.1

The downwave measurements are very consistent for the first two waves. The first wave shows some deterioration of wave height as it passes over the test section; however this trend is not repeated for the second wave which shows a slight increase in wave height. The third wave's height is much smaller than the first two waves and shows an increase in wave height after propagating over the test section.

The phase velocity is approximated using theory for the first of the three waves using a wave height of H = 9.9cm. After several iterations, cnoidal wave theory gives an Ursell number of U = *1020*, wave length of L = 910cm, and phase velocity of c_c=165 cm/s. This wave is well within the criteria for a shallow water wave, $\frac{h}{L} = 0.02 < 0.05$. Using linear shallow water wave theory a phase velocity of $c_{ls} = \sqrt{gh} = 140$ cm/s is obtained.

5.1.2 Solitary Wave

From measurements utilizing two wave gauges, phase velocities presented in Table 9 were obtained by measuring the time that it took for a wave feature to travel from one wave gauge to the next wave gauge position ΔL = 96.4 cm downwave. The phase velocity is approximately 15% higher when using the maximum water surface slope as a reference.

The wave height of the solitary wave was measured in the center of the test section by a single wave gauge. These measurements are shown in Table 10.

Table 9 – Experimental Phase Velocity for Solitary Wave

Wave	Using Maximum Water Surface Slope		Using Maximum Wave Height	
	Change In Time	Phase Velocity	Change In Time	Phase Velocity
	(sec)	(cm/s)	(sec)	(cm/s)
1	0.48	200.8	0.6	160.7
2	0.52	185.4	0.6	160.7
3	0.52	185.4	0.64	150.6
4	0.52	185.4	0.6	160.7
5	0.52	185.4	0.6	160.7
6	0.48	200.8	0.6	160.7
7	0.56	172.1	0.56	172.1
8	0.52	185.4	0.56	172.1
9	0.52	185.4	0.64	150.6
10	0.52	185.4	0.6	160.7
	Average	187.2	Average	161.0
	Std Dev	8.3	Std Dev	7.2

Table 10 – Experimental Wave Heights for Solitary Wave

Wave	Maximum Height
	(cm)
1	9.7
2	9.6
3	9.8
4	9.5
5	9.7
6	9.2
7	9.7
8	9.2
9	9.3
Average	9.5
Std. Dev.	0.2

The measurements of the wave height produced consistent results.

Using (44), the theoretical solitary wave phase velocity is:

$$c_s = \sqrt{g(h+H)} = \sqrt{981(9.3+9.5)} = 136\,\text{cm/s} \tag{101}$$

Using (40), the linear shallow water wave theory phase velocity is:

$$c_{ls} = \sqrt{gh} = \sqrt{981(9.3)} = 96 \text{ cm/s} \tag{102}$$

The experimental data yield phase velocities higher than those obtained through theory. It should be noted that this wave condition is not a true solitary wave of permanent form either in the constant depth portion of the flume or on top of the test section.

5.2 SURFICIAL TRANSPORT

5.2.1 Solitary Wave

5.2.1.1 Theoretical Surficial Transport – Solitary Wave

For the PET beads, the critical Shields number was found to be $\psi_{cr} = 0.0334$. Table 11 shows the results of theoretical calculations of surficial transport for the solitary wave condition. The fitted parameters (u_{bmf} and T_f) , bottom excursion amplitude, friction factor, and total integrated bedload transport are given. The total bedload was calculated at three different locations using ensemble averaged velocity records collected at three points along the length of the sediment tray with (59).

Table 11 – Surficial Sediment Transport Using Method 1 (Solitary Wave)

Station (cm)	u_{bmf} (cm/sec)	T_f (sec)	A_{bm} (cm)	f_w	q_b (cm^2/wave)
35	67.24	1.05	11.22	0.0202	5.65
50	63.50	1.05	10.64	0.0206	5.15
65	60.59	1.06	10.20	0.0211	4.86
				Average	5.22
				Std. Dev.	0.40

It can be seen that the wave friction factor increases as the wave progresses over the test section while the maximum fitted bottom velocity decreases. This can be attributed to the wave increasing in steepness, but dissipating energy as it breaks. From the upwave to the downwave side of the sediment tray there is a clear trend of decreasing total surficial transport; the total bedload decreases by approximately 15% from Station 35 to Station 65.

Table 12 shows estimates of bedload induced by the solitary wave using Method 2.

Table 12 – Surficial Sediment Transport Using Method 2 (Solitary Wave)

Station (cm)	A_{bm} (cm)	f_w	q_b (cm^2/wave)
35	11.37	0.0201	5.61
50	10.17	0.0210	5.29
65	10.06	0.0211	4.86
		Average	5.25
		Std Dev	0.38

The differences between the results obtained by Method 1 and Method 2 can be considered negligible.

Table 13 shows the bead excursion lengths for the solitary wave condition and PET beads. The theoretical excursion lengths should correlate with the distance from the up wave end of the sediment box required achieve a constant experimental surficial transport. The critical velocity, u_{cr}, was calculated using friction factors from both Method 1 and Method 2.

Table 13 – Bead Excursion Lengths (Solitary Wave)

Station (cm)	Method 1 (cm)	Method 2 (cm)
20	32.57	31.81
35	41.95	41.20
50	46.11	45.74
65	43.26	43.63
80	42.92	43.28
Average	41.36	41.13

The differences between Method 1 and Method 2 are negligible. The calculated excursion length reaches a maximum in the middle of the tray at station 50 and decreases at the upwave and downwave ends of the tray. However, the excursion length calculated at a particular station does not necessarily indicate the excursion length of an individual bead within the sediment tray. However, the average excursion length should give a reasonable estimate for a typical bead at any position along the sediment tray. Both methods predict that the experimental transport should increase over the first ~40cm of the sediment tray. Due to the inherent inaccuracies associated with theoretical calculations of sediment transport an advanced analysis is not warranted.

5.2.1.2 Experimental Surficial Transport – Solitary Wave

Surficial transports results were obtained by measuring the elevations of the smoothed sediment bed, passing two solitary waves over the test section, and then re-measuring the elevations of the sediment bed. Transport quantities were obtained by integrating (32) which incorporates the number of waves passed over the test section between elevation measurements.

Three two-wave pairs (6 solitary waves) were completed before the sediment bags were removed to measure the beads within them. Nine two-wave pairs (18 solitary waves) were passed over the test section, to obtain nine realizations of surficial sediment transport. The first wave pair

over a newly smoothed bed yielded a larger transport than the subsequent waves; transport decreased as every wave pair was passed over the bed. The nine realizations of transport were divided into groups by the number of wave pairs that had been passed previously over the newly smoothed bed.

A minimum of twenty-five waves passed over the test section before measurements were taken. The subsurface transport's contribution to the total transport measured by this method is considered negligible. See section (5.3.1) for an analysis of the relative subsurface and surficial transport quantities.

Figure 40, Figure 41, and Figure 42 show the average of three realizations of surficial transport of the first, second, and third wave pairs passed over a newly smoothed sediment bed, respectively. The error bars denote one standard deviation from the mean transport. The transport under a single wave is shown.

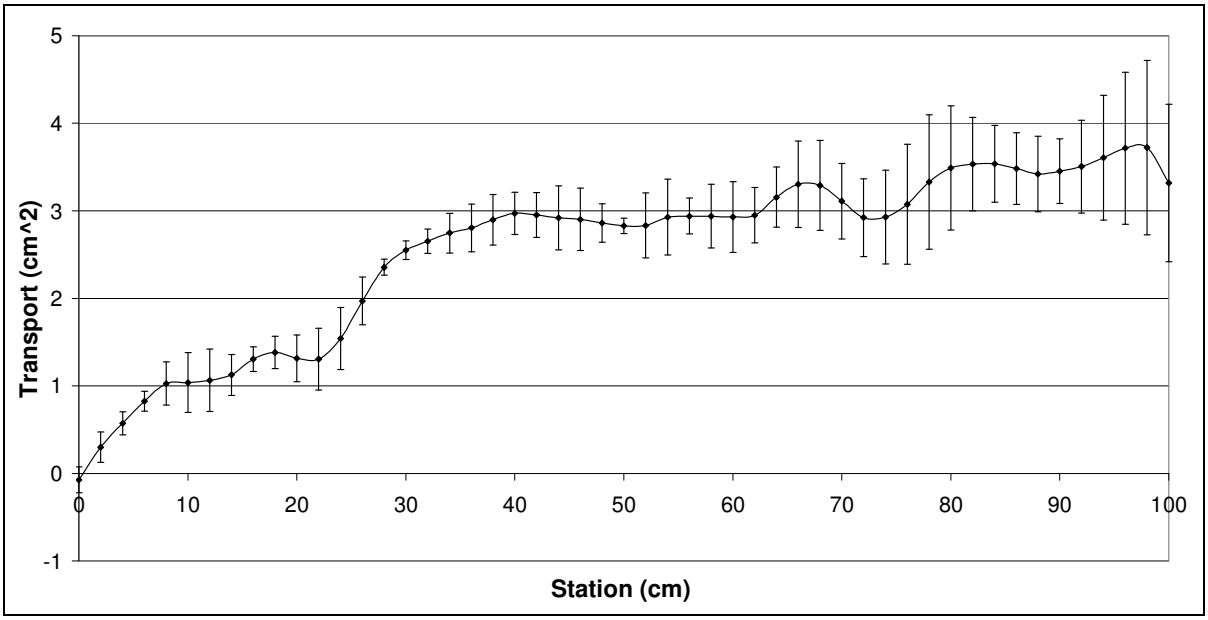

Figure 40 – Average Surficial Transport of First Wave Cycle Passed Over a Smoothed Bed

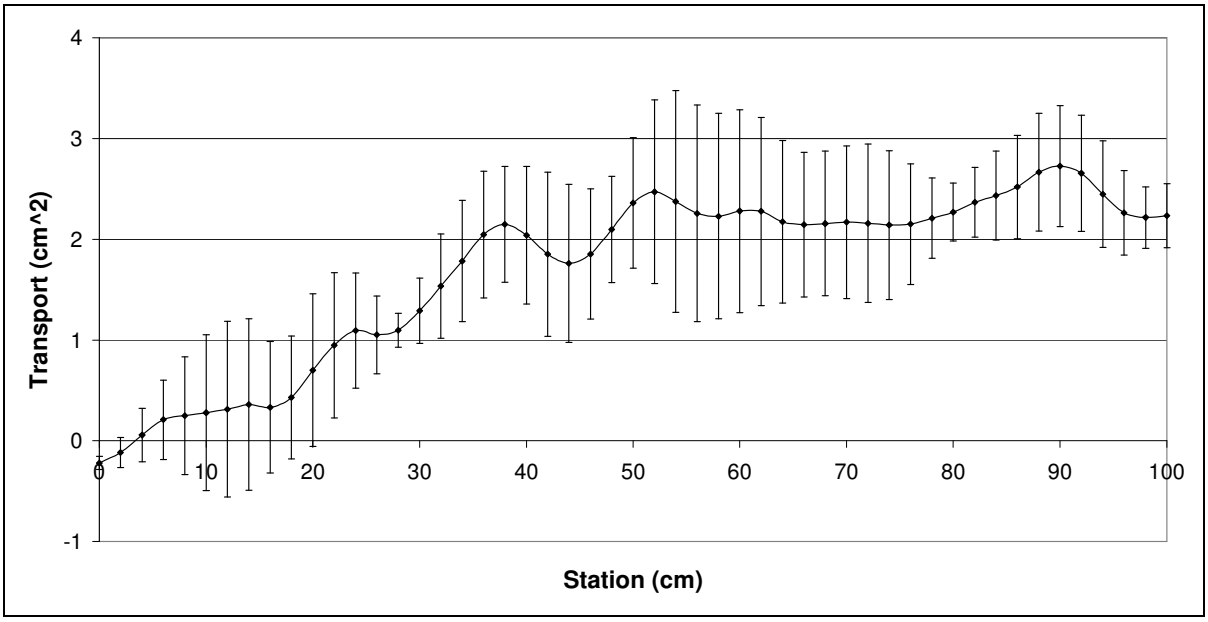

Figure 41 - Average Surficial Transport of Second Wave Cycle Passed Over a Smoothed Bed

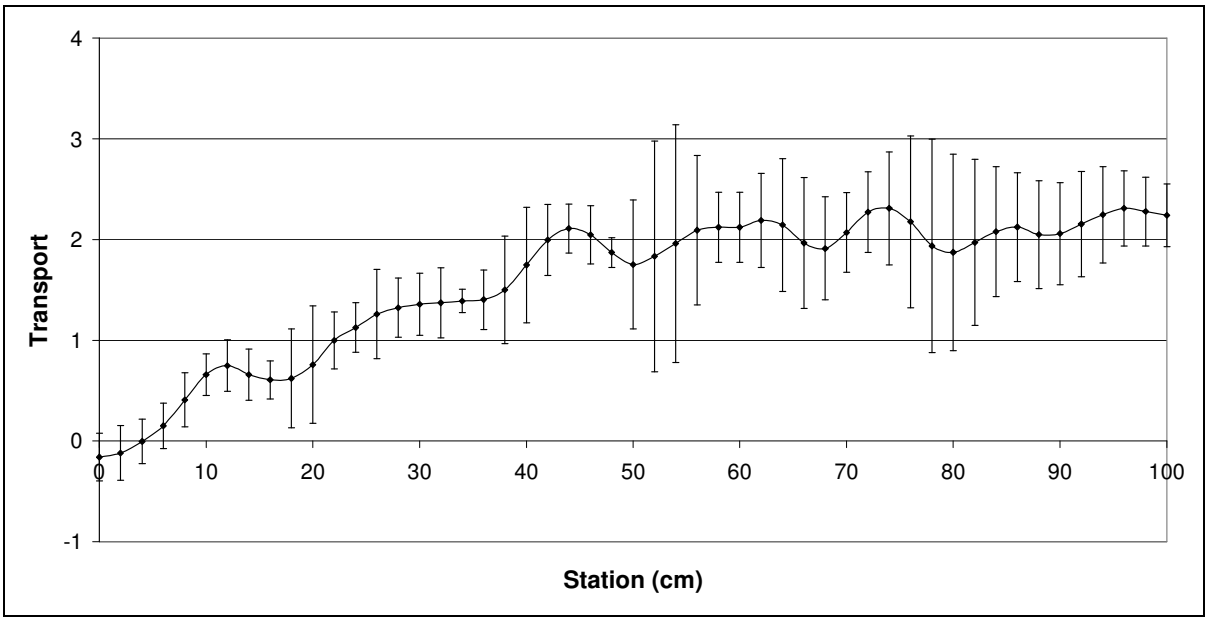

Figure 42 - Average Surficial Transport of Third Wave Cycle Passed Over a Smoothed Bed

Although, a significant amount of scatter is present between the realizations, a clear increase in transport is noted for the first ~40cm of the sediment tray, approximately the excursion length predicted in 5.2.1.1. After this initial increase, the surficial transport can be estimated from the values between Station 40 and 60. The first wave pair over a newly smoothed bed yields a

transport of roughly $q_b = 3\text{cm}^2$ per wave, the second pair a transport of roughly $q_b = 2.2\text{cm}^2$ per wave, and the third pair a transport of $q_b = 2\text{cm}^2$ per wave. There is evidently a decrease in transport as more wave cycles have passed over the test section.

The theoretical bedload transport of 5.2 cm^2 per wave is approximately double that of each of the experimental measurements. A conservatively high theoretical estimate is to be expected, as the friction factor used throughout the entire wave record was calculated using the rapid acceleration under the leading front of the crest. Given that theoretical sediment transport predictions are typically considered successful if they within the same order of magnitude of the observations, the agreement between the theoretical and experimental results for the solitary wave condition is very good.

5.2.2 Three Wave Burst

5.2.2.1 Theoretical Surficial Transport – Three Wave Burst

The bedload transport beneath the entire three-wave burst record was estimated using the methodology presented in section 4.2.2.2. The velocity record is shown in Figure 43. The TWB record contains an initial crest followed by three major waves (each with a crest and trough), yielding a total of four crests and three troughs. Following the three major waves, some choppiness persists in the water column above the test section. Each of the ten velocity measurements used in the ensemble average were taken at station 50.

If the velocity record is averaged over the first 26 seconds, it is found that velocity record has a mean "current" of u = -3.32 cm/s, with the minus sign denoting that the current is seaward. Given the relatively short length of the TWB, a steady-state current has not had enough time to

develop; however, for simplicity the measured current will be considered constant throughout the velocity record. To formally address the presence of both waves and a current, the interaction between the waves and current could be resolved using one of the several theoretical models presented in *Sleath*, (2004). The transport induced by the current would be of crucial importance if the waves were periodic, not peaked or forward leaning, yielding an identical amount of shoreward and seaward transport. However, given that the waves in the TWB are skewed and highly asymmetric, with peak velocities (u ~ 45 and -30 cm/s), the waves will induce a net shoreward transport much larger than the current (u ~ 3cm/s) keeping in mind that the bedload transport is proportional to u^3. Therefore, the current's contribution to the total transport was neglected. The velocity record shown in Figure 43 has a mean of zero.

To determine the friction factor for each segment of positive and negative velocity, the seven colored sections (A through G as shown in Figure 43) were integrated to obtain an equivalent bottom excursion amplitude. The excursion amplitudes for each section shown along with their respective friction factors, calculated using (51), in Table 14. It can be seen that the friction factors obtained for the crests are larger than those obtained for troughs, indicative of the larger accelerations present beneath the crests.

Figure 44 shows the velocity record, wave friction factor, Shields parameter, instantaneous bedload transport, and cumulative transport for the TWB. The two horizontal lines on the Shields parameter plot denote the critical Shields parameter. The friction factor obtained for crest G is used for the remainder of the record although very little transport occurs after the third wave. It can be seen that the majority of the transport occurs beneath the crest denoted as *C*. The total net theoretical bedload transport was found to be $q_b = 2.57$ cm^2.

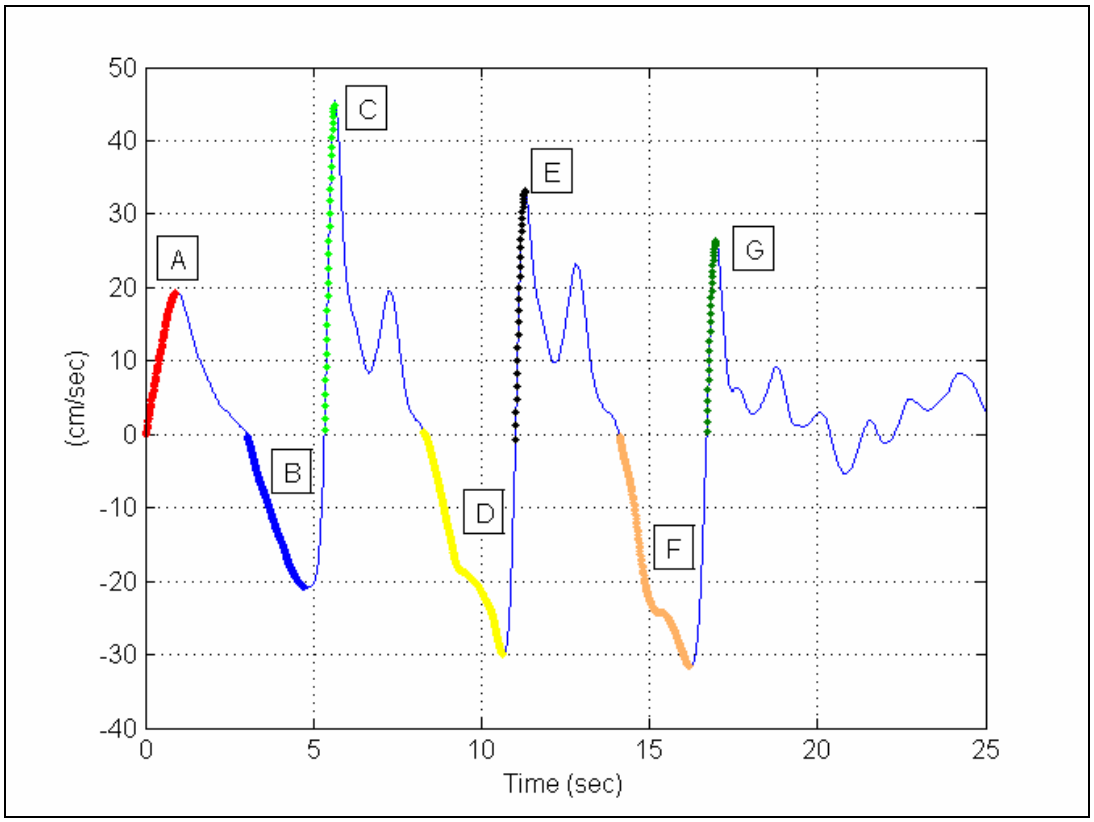

Figure 43 – TWB Ensemble-Averaged Velocity Record with Integrated Sections

Table 14 – TWB Amplitudes and Wave Friction Factors

Section	*Abm* (cm)	*fw*
A	9.47	0.022
B	-20.99	0.017
C	7.47	0.025
D	-38.39	0.014
E	5.76	0.027
F	-40.90	0.013
G	4.44	0.031

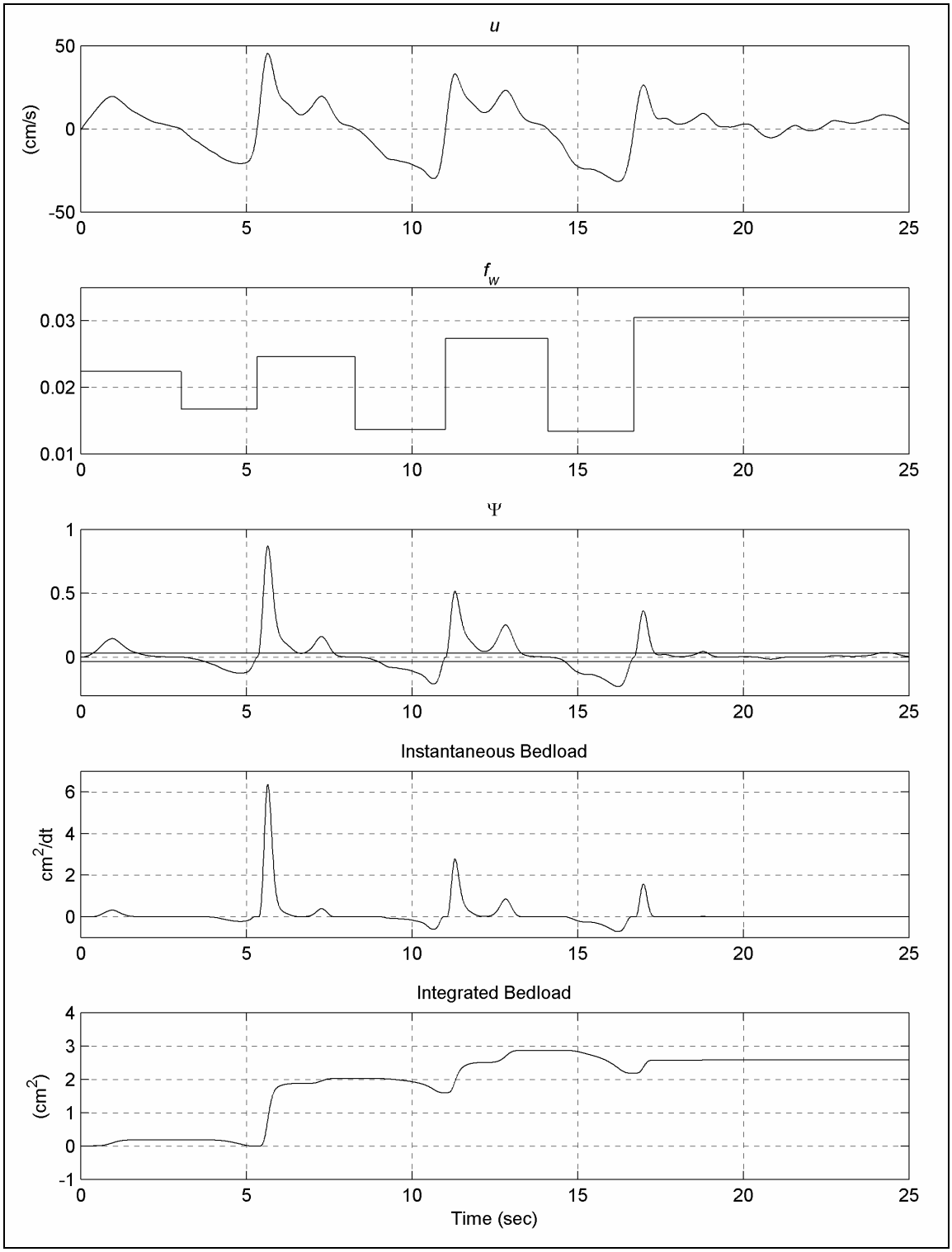

Figure 44 – TWB Theoretical Subsurface Transport

5.2.2.2 Experimental Surficial Transport – Three Wave Burst

Three separate measurements of the surficial transport beneath the TWB were taken. All measurements were made using a sediment bed that previously had at least 50 three wave bursts pass over it, minimizing the contribution of subsurface transport. See section 5.3.2.2 for a comparison of the relative magnitudes of surficial and subsurface transport.

Figure 45 shows the results from each experiment. From Station 30 to 50 the three measurements have nearly the same transport; before and after this section the three realizations differ from one another. A small peak is present in each transport measurement at approximately Station 90 likely a result of boundary effects. The transport at station 100 appears to increase after each successive resmoothing, although this trend was not evident in the solitary wave condition. This trend could be due to random occurrence.

Figure 46 shows the average of each of the three measurements with error bars denoting one standard deviation from the mean. Surficial transport increases over the first 30 cm of the sediment tray for each measurement. In the center of the sediment tray, from Station 35 to 80, the average surficial transport is nearly constant at q_b = 3cm^2. This value is in excellent agreement with the theoretical value presented in section 5.2.2.1 of q_b = 2.57 cm^2.

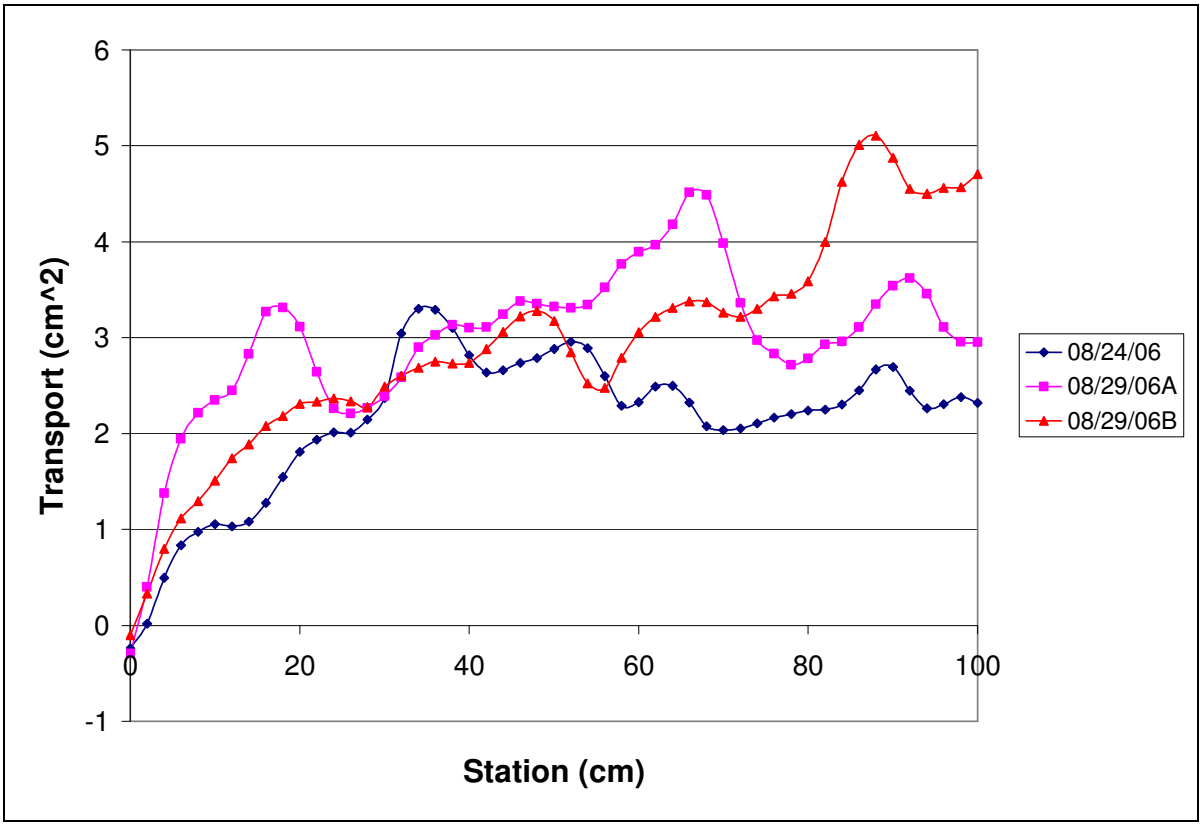

Figure 45 – Three Measurements of Experimental Surficial Transport Beneath the TWB

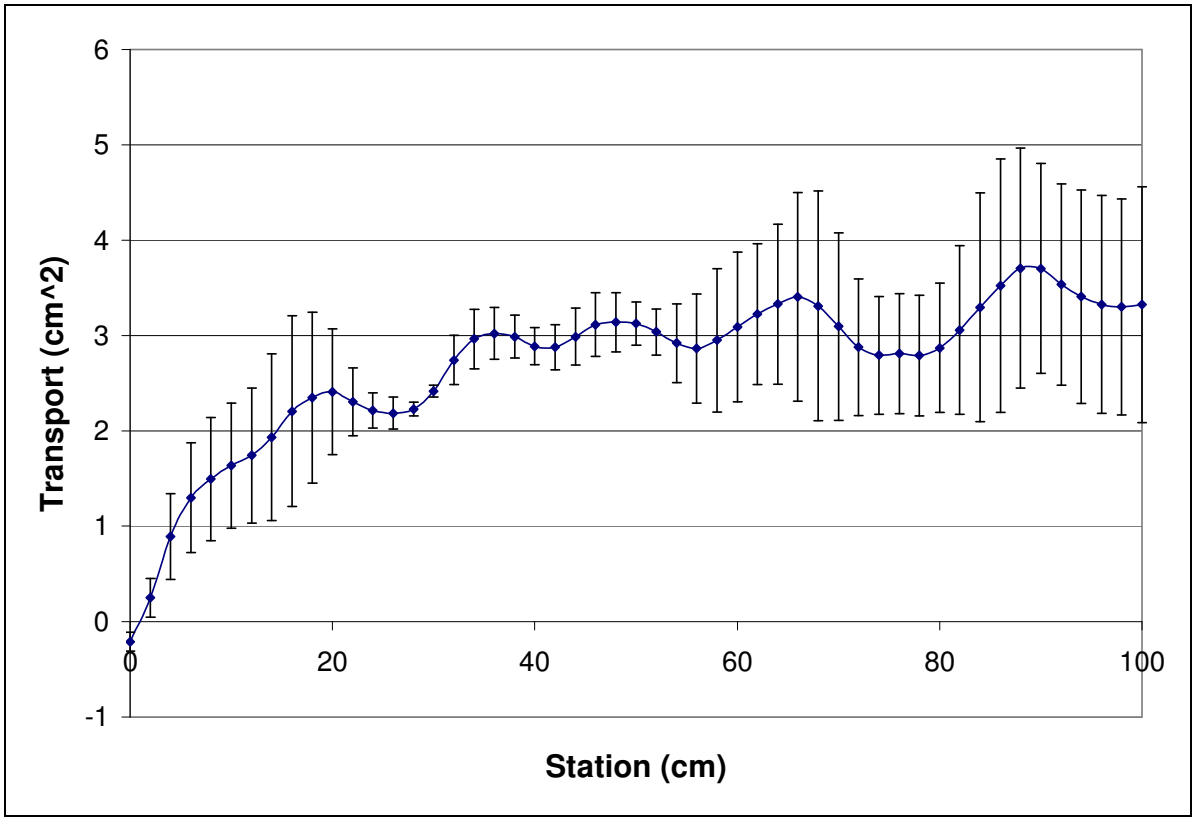

Figure 46 – Average Experimental Surficial Transport Beneath the TWB

5.3 SUBSURFACE TRANSPORT

5.3.1 Solitary Wave

5.3.1.1 Comparison of Theoretical and Experimental Results

Four experiments were conducted to measure the subsurface transport with the solitary wave condition and PET beads. In each of the experiments large movements of the colored sediment column were observed for the first wave. After the initial wave, the movements of the colored column became smaller and smaller with each passing wave. After ~100 waves the colored column's movements became almost imperceptible to the eye. This decrease in movement is likely due to a strengthening of the sediment bed. For an uncohesive material this strengthening can be characterized by an increase in the friction angle. Section 3.5.1 notes an increase in the friction angle when a sediment sample was mechanically vibrated. It is hypothesized that the wave action agitates the sediment bed in a qualitatively similar manner as the mechanical vibrations, increasing the friction angle and thereby attenuating the subsurface sediment movement.

Both forwards (in direction of the beach) and backwards (towards the wavemaker) movements of the sediment column were recorded under the passage of each wave condition in this study. The sediment column moves forward during the passage of the steep forward leaning portion of the wave, maintains its position for ~ 0.2 second, and then moves back to nearly its initial position, leaving only a slight net forward movement. Backwards movement was not expected to occur with this wave condition. See the section 6.1.2.1 for possible explanations on why this occurs. For each wave the position of the sediment column is measured in the initial position, at its maximum forward excursion, and at its final position after which the wave had passed over.

The subsurface movement was found to depend somewhat on the preparation of the sediment bed. Differences in colored sediment column width, the presence air bubbles within the colored sediment column, and initial level of sediment bed compaction all might have affected the subsurface sediment movement. Table 15 gives the colored sediment column characteristics for each experiment.

Table 15 – Colored Sediment Column Characteristics – Solitary Wave

Experiment	Approximate Width of Colored Column	Air Content
02/07/06	25mm	No air bubbles
06/06/06	10mm	No air bubbles
06/22/06	20mm	Air bubbles present
06/25/06	15mm	No air bubbles

To effectively remove air bubbles, the colored sediment particles were stirred in the sediment tray while still in the confines of the injector. This movement slightly compacts the sediment bed and makes the sediment column wider by pushing the two Plexiglas sheets of the injector further apart. The removal of the Plexiglas sheets of the injector potentially weakens the sediment bed as the beads fill in the void left by the 3mm wide Plexiglass sheets as they are removed. The sediment-water matrix along the colored-clear bead interface the sediment bed is likely weaker due to a lack of compaction experienced by the rest of the sediment bed. Smaller colored columns widths places the two weakened areas closer together, allowing the colored column to be less resistant to movement than if the weakened areas were placed further apart with a wider, “strong” compacted column of colored beads between them.

Figure 47 shows the experimental deflections of the colored sediment column (thick colored lines) of the 02/07/06 experiment along with the theoretical deflections (thin lines). The experimental deflections are obtained by subtracting the colored column's maximum forward position from its position before the wave reached the test section. In other words, the plotted deflection is the forwards movement the column undergoes during the passage of the wave crest. For each experimental deflection the number of the wave that generated the deflection is noted. The waves are numbered such that "20 Waves" denotes the subsurface deflection of the 20^{th} wave that has passed over the virgin sediment bed. Each theoretical line notes the friction angle used to calculate the deflection. A phase velocity of c = 190 cm/s is used for each of the theoretical deflection calculations, corresponding to the experimentally measured phase velocity using the maximum water surface slope as a reference point. Porosity and sediment density values from section (3.3.1) were also used in the theoretical calculations.

Figure 48, Figure 49, and Figure 50 show experimental and theoretical deflections for the 06/06/06, 06/22/06, and 06/25/06 experiments respectively. Because of the visualization techniques used to calculate deflections, (described in section 4.1.1), the thick colored lines representing experimental observations are jagged, appearing to show discontinuities in the colored sediment column's deflections. Actual deflections encountered in laboratory were much smoother than what the following figures suggest.

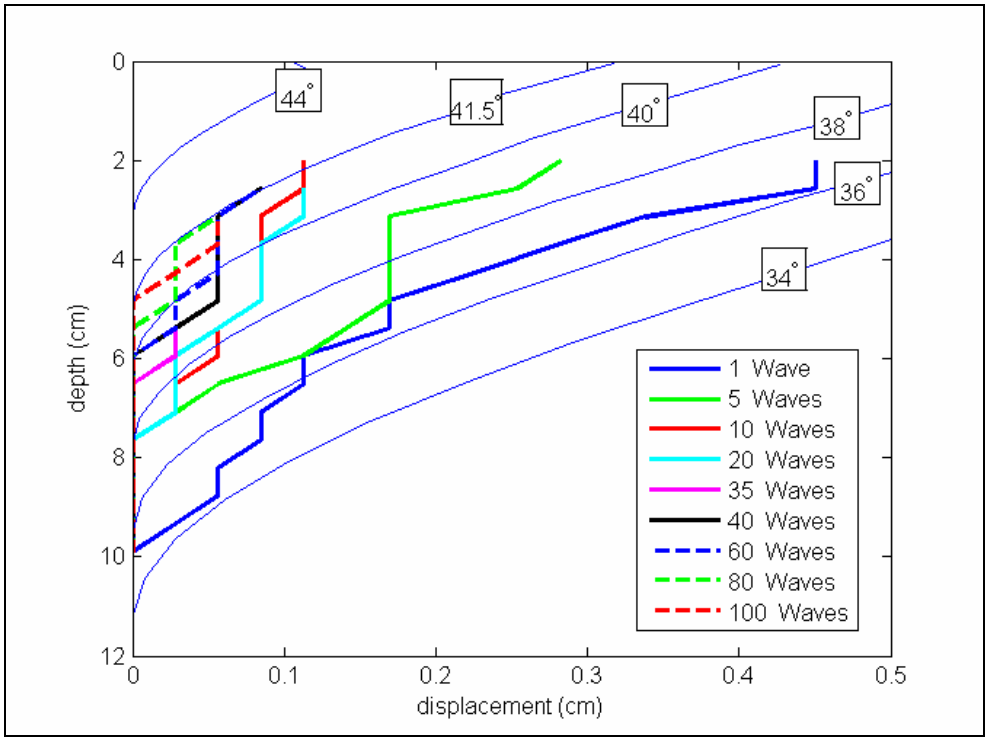

Figure 47 – 02/07/06 Solitary Wave Displacements using c=190 cm/sec

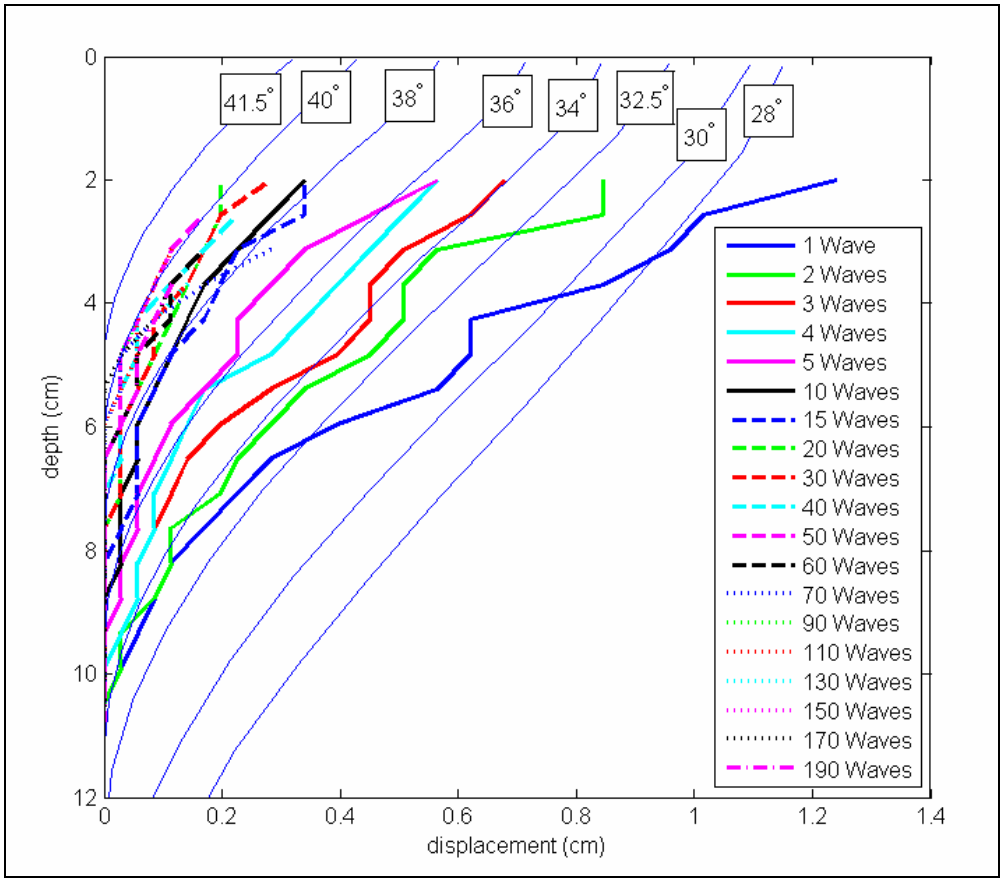

Figure 48 – 06/06/06 Solitary Wave Displacements using c=190 cm/sec

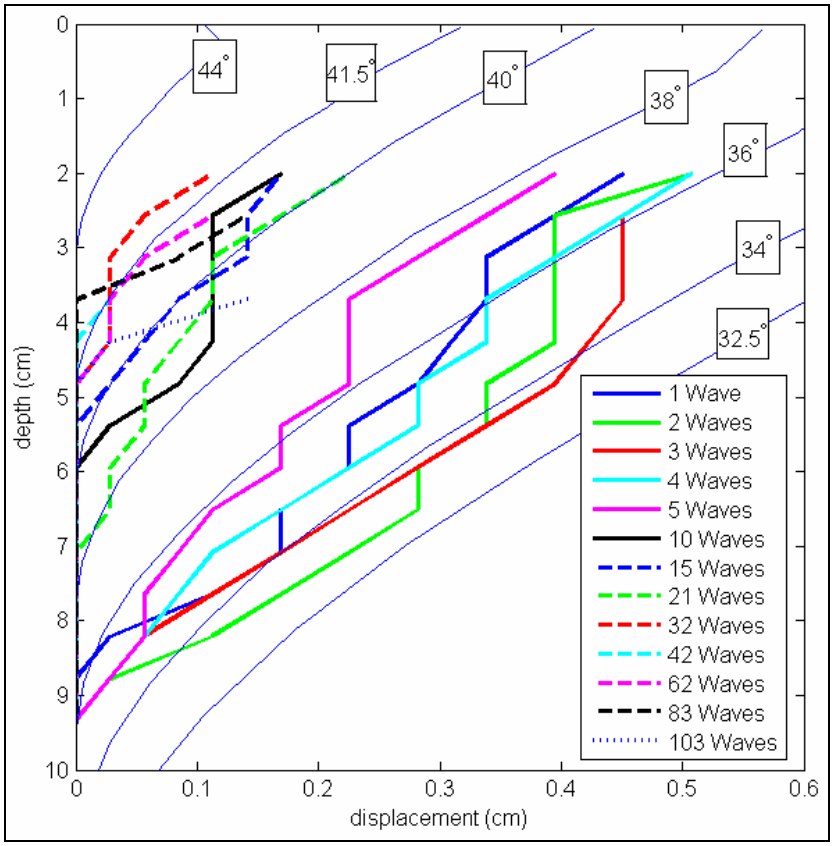

Figure 49 – 06/22/06 Solitary Wave Displacements using c=190 cm/sec

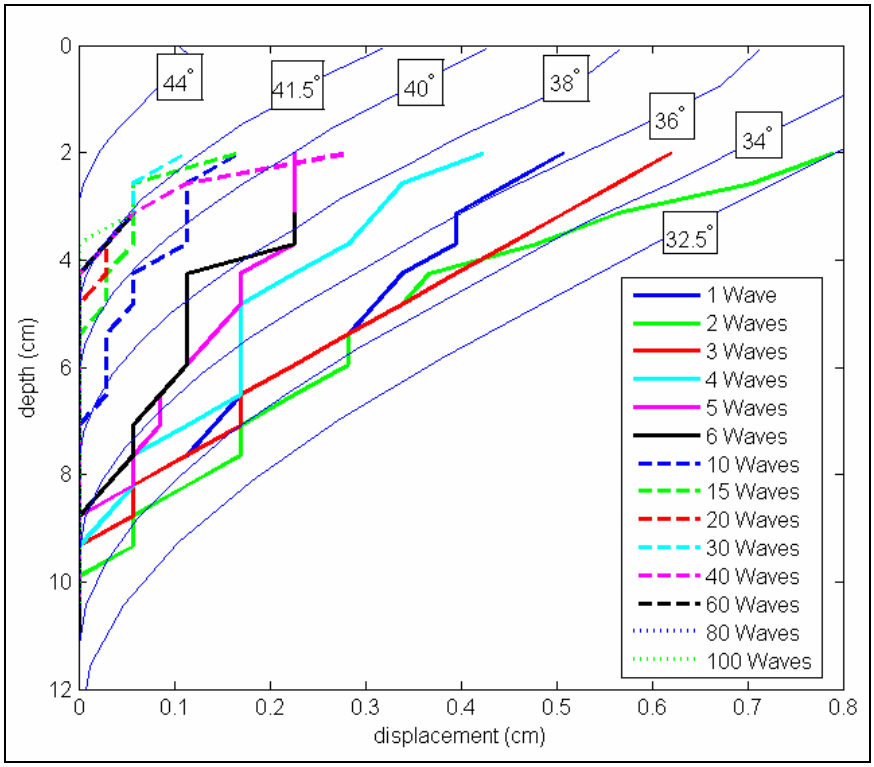

Figure 50 – 06/25/06 Theoretical Solitary Wave Displacements using c=190 cm/sec

In each experiment, an attenuation of subsurface sediment movement can be seen as the number of waves passed over the virgin bed is increased. The 02/07/06 experiment shows the smallest deflections, which is probably correlated with its large colored column width. The 06/06/06 experiment shows the largest deflections, which could be correlated to the small colored column width. In this experiment, the first wave's subsurface deflection is uncharacteristically large, probably due to very loose initial sediment bed conditions. This deflection will be considered an anomaly and will be omitted from future analyses. The air bubbles in the 06/22/06 experiment do to not seem to dramatically affect the subsurface movements; its deflections are quite similar to that of the 06/25/06 experiment.

Although the experimental deflections have some variability, each deflection exhibits some correlation with a theoretical deflection using a reasonable value of the friction angle. This correlation can be seen in both the maximum depth of displacement and the excursion lengths of the subsurface beads. The friction angles plotted are similar to those measured in section 3.3.3 for the PET beads. Slight differences between the measured and insitu friction angles of the beads are to be expected due the inherent difficulties of maintaining a uniform level of compaction when injecting the colored column.

Figure 51 shows the average experimental deflections of the four experiments. The deflection from the four experiments is averaged for each depth. For experiments that did not have a measurement taken at a particular number of waves, the deflections are obtained by linear interpolation between the deflections that were measured. The first wave from the 06/06/06

experiment was omitted from the averaging. The theoretical results use a phase velocity of c = 190cm/s. Figure 52, Figure 53, and Figure 54 show the same average experimental deflections for the four experiments and the theoretical deflections using c = 180, 160, and 140 cm/s, respectively. The c = 160 cm/s phase velocity corresponds to the experimentally obtained phase velocity using the maximum wave height as a reference point. The c = 140 cm/s phase velocity corresponds to the theoretical solitary wave phase velocity.

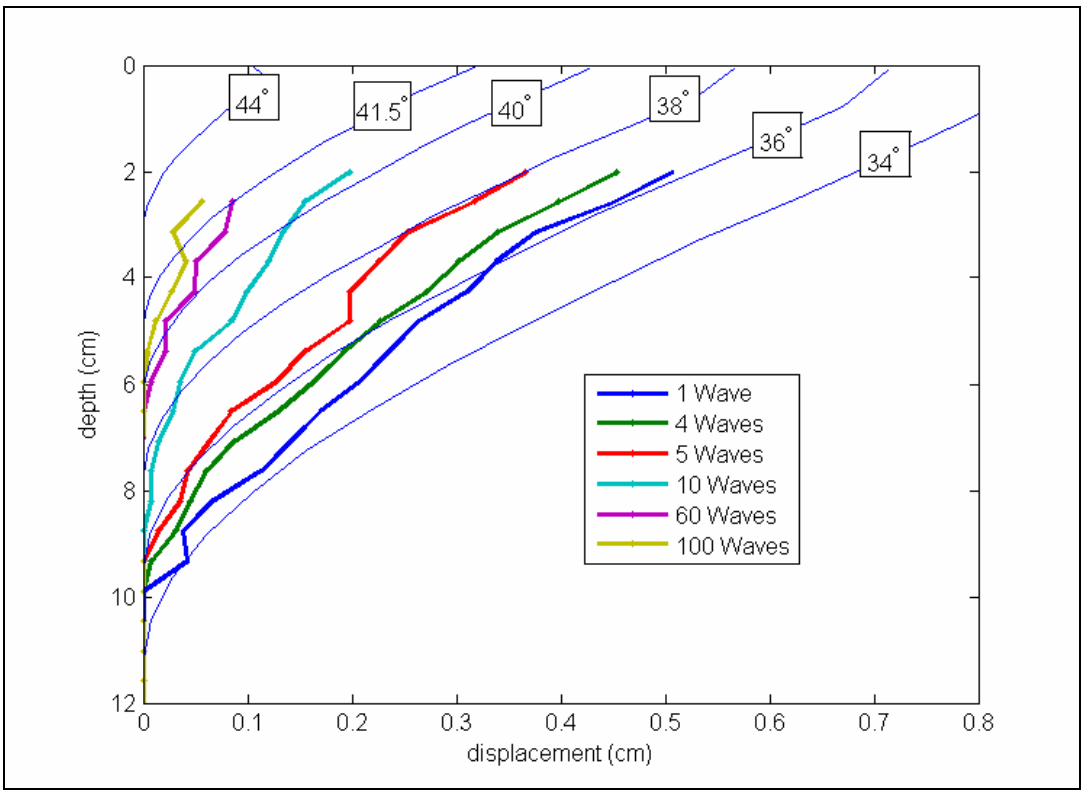

Figure 51 – Solitary Wave Average Displacements using c=190 cm/sec

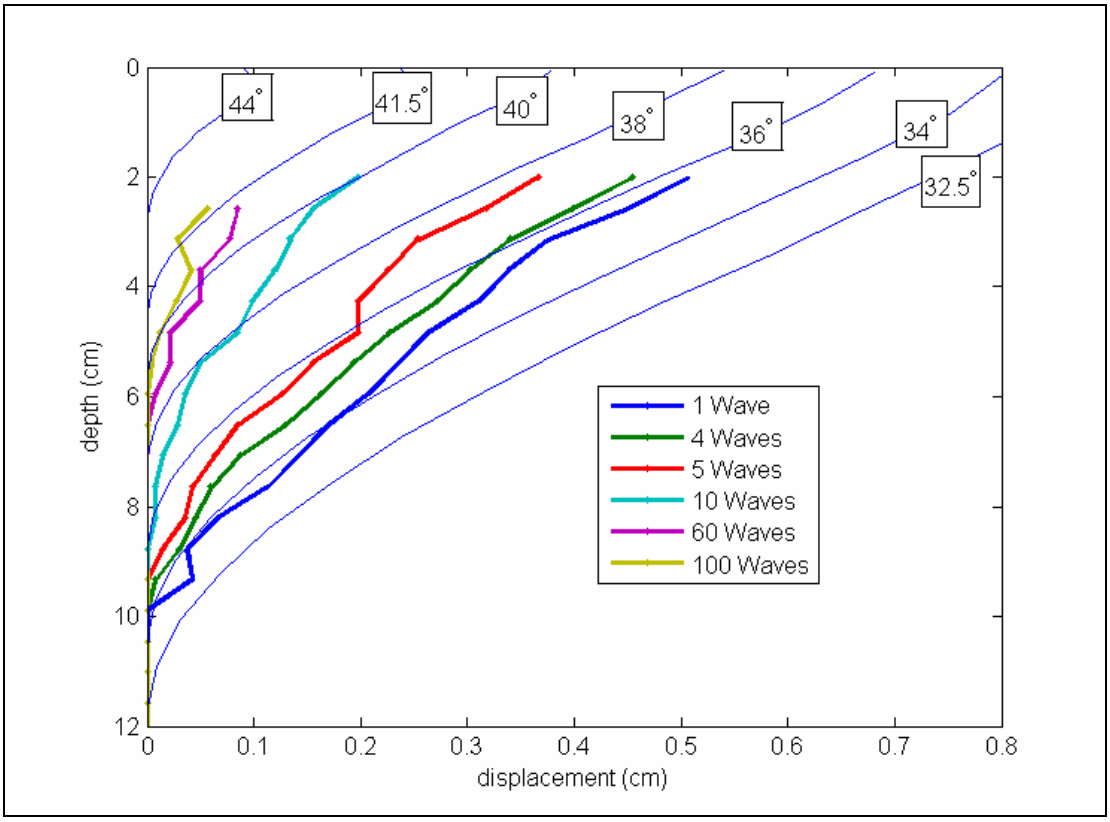

Figure 52 – Solitary Wave Average Displacements using c=180 cm/sec

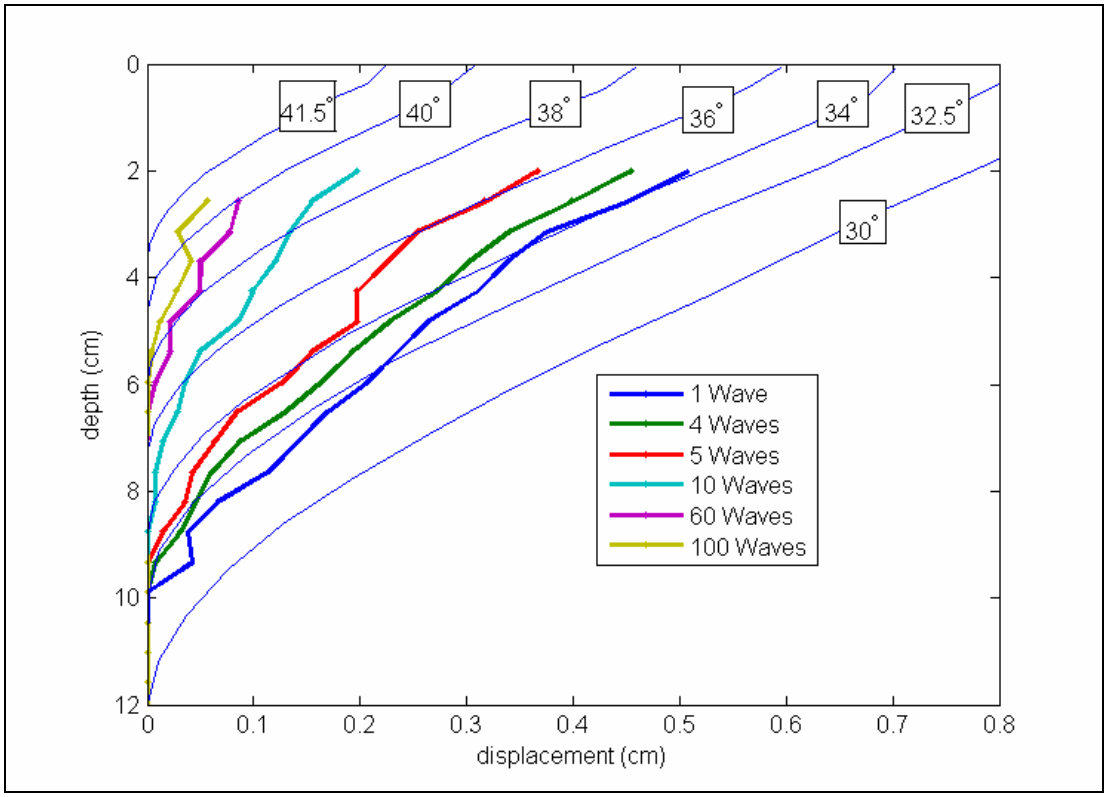

Figure 53 – Solitary Wave Average Displacements using c=160 cm/sec

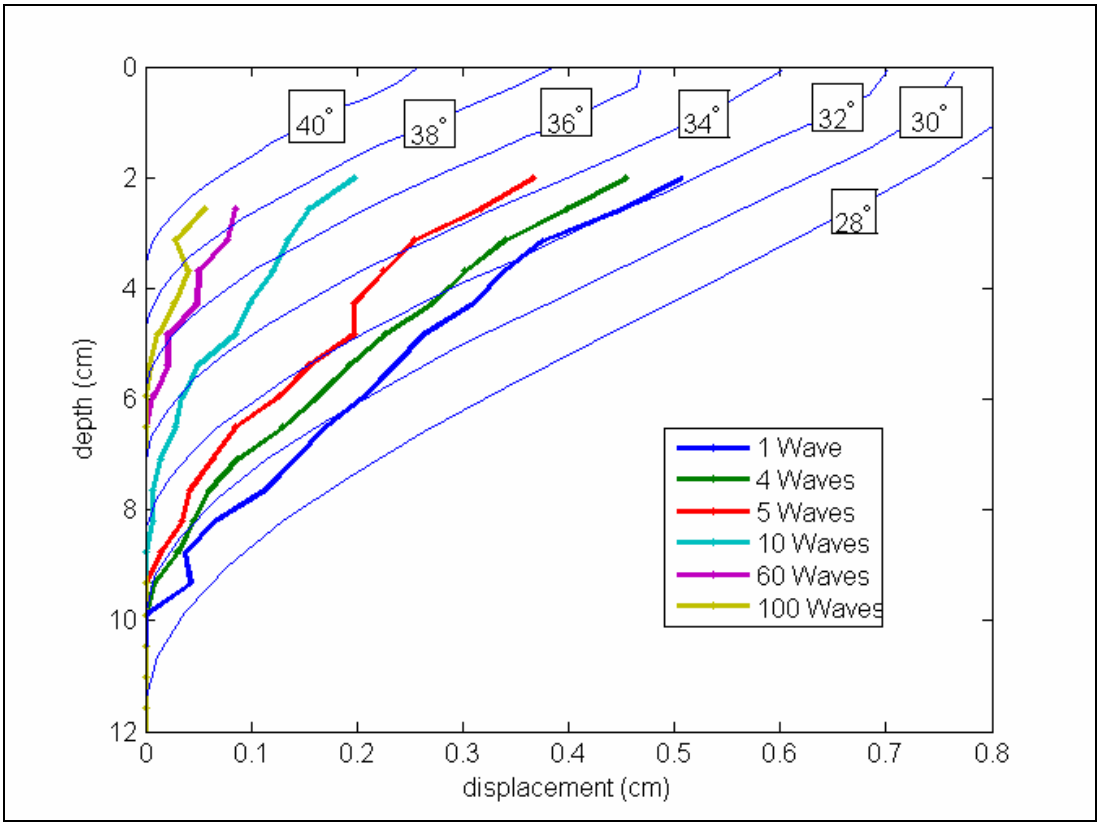

Figure 54 – Solitary Wave Average Displacements using c=140 cm/sec

For this wave condition it is apparent that increasing the phase velocity results in an increase in the theoretical subsurface deflection and maximum depth of displacement. An increase in phase velocity leads to an increase in $\ell_{s\max}$ and similarly influences the length of the subsurface sediment's deflections. If the friction angle is chosen as a parameter that is used to fit the theoretical maximum depth of displacement to the experimental maximum depth of displacement, the theoretical sediment deflections appear to slightly overestimate the experimental deflections for each phase velocity shown.

Figure 55 shows the dependency of the number of waves that have passed over a virgin bed on the maximum depth of discernable disturbance. The maximum depth of disturbance was

obtained through careful observations of videos of the subsurface movement, however, some subjectivity is present in these measurements because there is not a clear depth demarcating the transition to zero sediment movement. Theoretical maximum depths of disturbance are shown by the dotted lines for different friction angles. A phase velocity of c = 190 cm/s was used in each theoretical calculation.

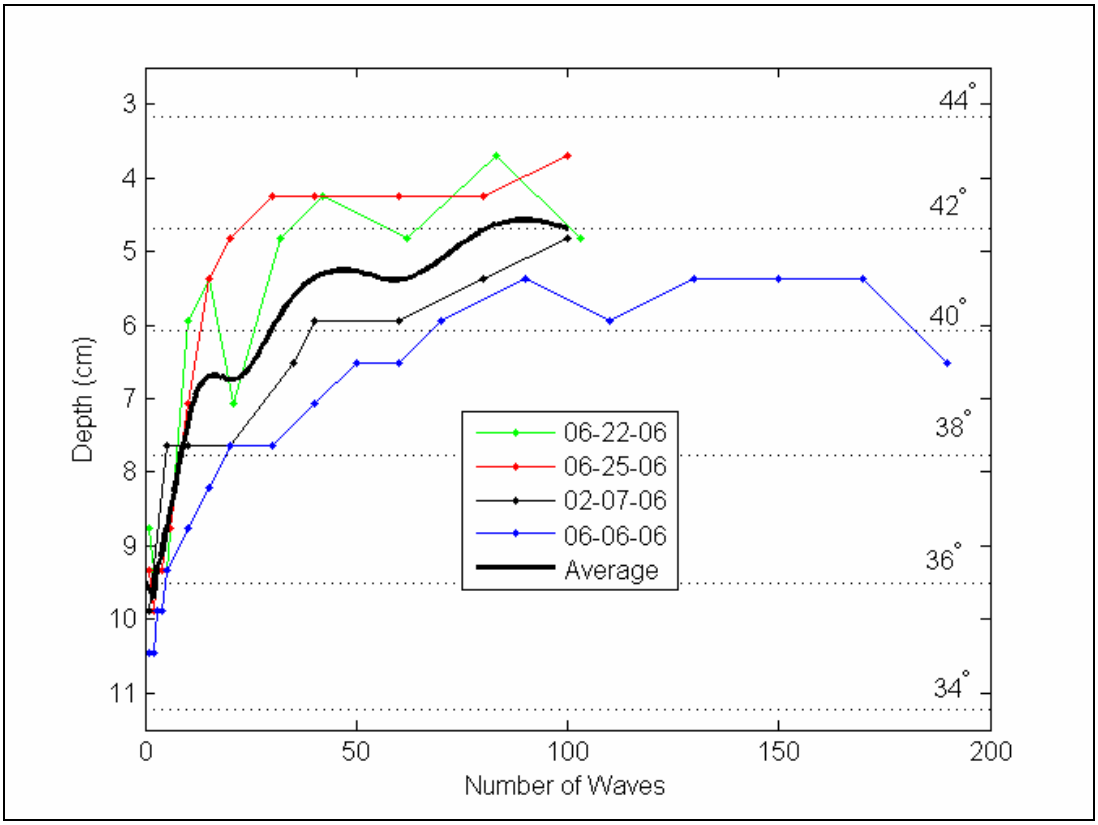

Figure 55 – Experimental Maximum Depth of Movement (Solitary Wave)

There is a clear trend of the maximum depth of disturbance becoming smaller as more waves are passed over the sediment bed. The 06/06/06 experiment has the deepest subsurface movements, followed by the 02/07/06 experiment; the effect of colored column width on the maximum depth of disturbance is not particularly striking. The experimental results correspond fairly well to theoretical estimates of the maximum depth of displacement using the friction angles measured for the submerged PET beads (presented in Table 5). For the first few waves, a friction angle of

$\phi \approx 35^{\circ}$ (corresponding to the unvibrated submerged samples) roughly matches the experimental displacements. After 100 waves, however, the experimental results correspond to theoretical estimates using a friction angle of $\phi \approx 42^{\circ}$, slightly higher than that of the friction angle measured for the vibrated submerged samples ($\phi \approx 39^{\circ}$). Since the mechanical vibrations used to obtain the friction angle measurements in 3.3.3 are not qualitatively the same as wave agitation of the sediment bed, some variation between the two cases is to be expected.

Figure 56 shows the variation of the colored sediment column's depth-integrated forward deflections, *As*, with the number of waves passed over a virgin bed. The total forward movement of the sediment column is found for each depth by subtracting the maximum forward column position from the column's position before the wave of interest perturbs the sediment bed. These values are fitted with a linear function and integrated from the maximum depth of disturbance to the sediment-water interface, using the linear fit to extrapolate subsurface movement obscured by the false bottom (as described in section 4.1.1). Theoretical values are shown by the dotted lines which were calculated using c = 190 cm/s. Figure 57 shows the experimental *As* plotted in log-log format.

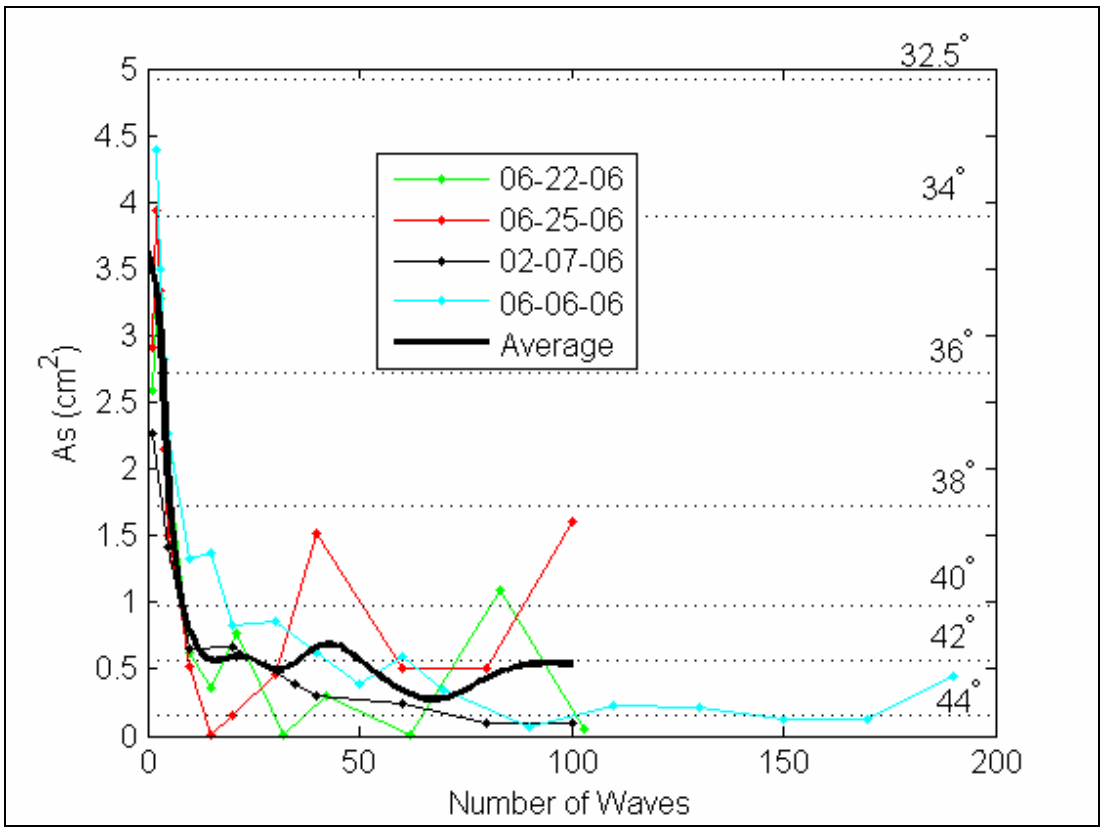

Figure 56 –Experimental Depth-Integrated Forward Excursion (Solitary Wave)

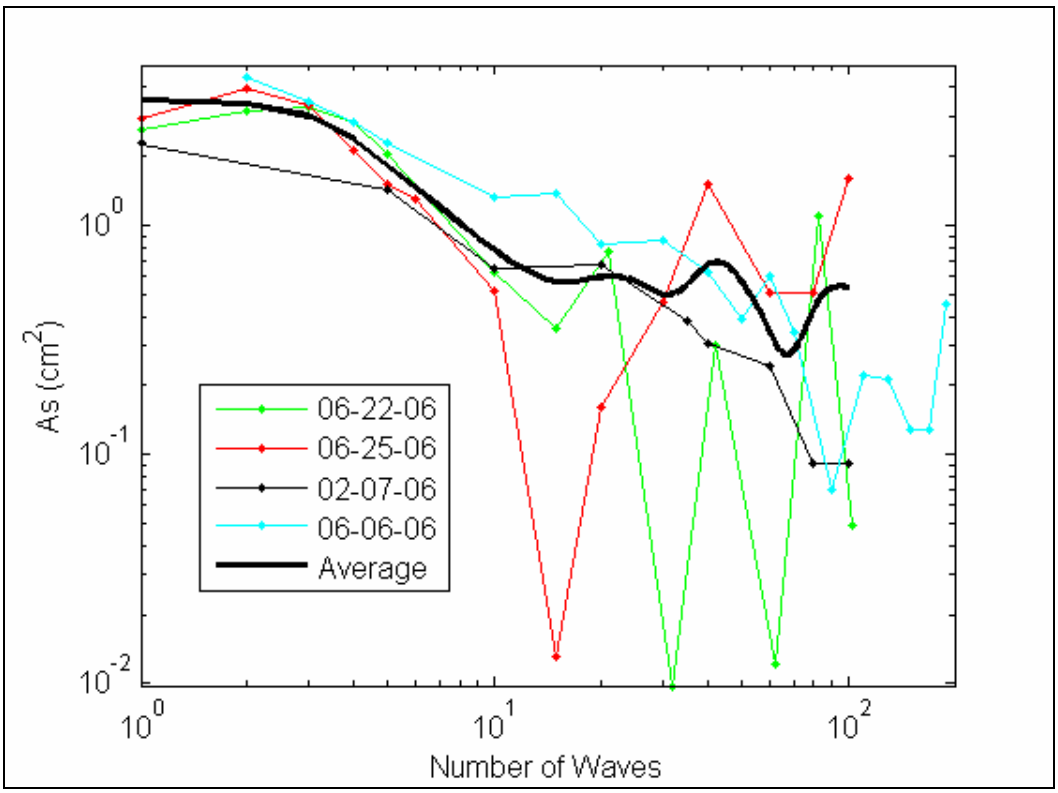

Figure 57 –Experimental Depth-Integrated Forward Excursion (Solitary Wave)

It can be seen that the depth-integrated forward subsurface movement of the sediment column experiences a sharp decrease at approximately wave 15. This decrease can be attributed to both a reduction in the maximum depth of disturbance and horizontal column movement. Aside from a few measurements, the depth-integrated forwards movement appears to reach a near constant value after the 15^{th} wave. Before the 15^{th} wave, there is relatively little variation in the four experiments. The experimental results correspond to the theoretical estimates with friction angles roughly the same as that of the maximum depth of disturbances, showing relatively good agreement with the friction angles presented in Table 5.

Figure 58 shows the effect of the number of waves that have passed over a virgin sediment bed on the total cumulative transport. The cumulative transport is obtained at each depth by subtracting the final position of the colored sediment column after undergoing forwards and backwards movements from its original position at the beginning of the experiment before any waves were passed over the tray. These quantities are fitted with a linear function and integrated from the maximum depth of displacement to the sediment-water interface. The transport induced by the first wave of the 06-06-06 experiment was removed from subsequent measures of the cumulative transport.

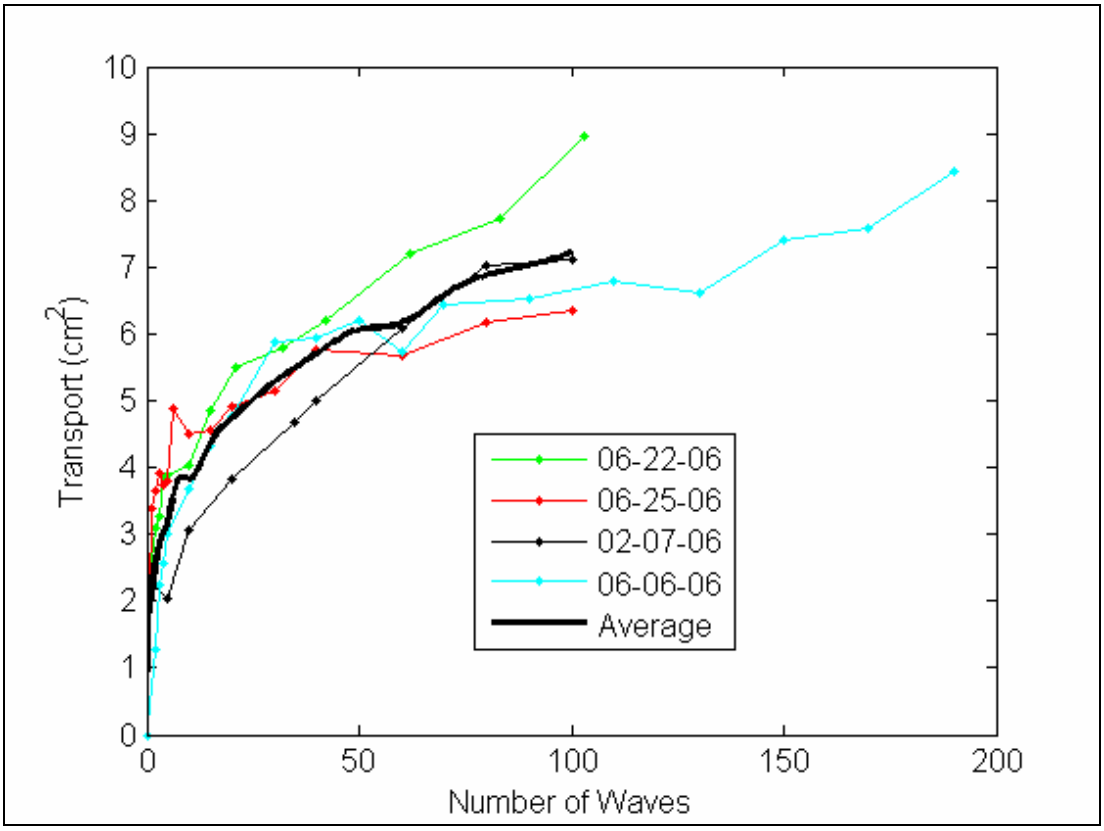

Figure 58 – Cumulative Net Subsurface Transport (Solitary Wave)

The four experiments all have similar cumulative transport records. A large cumulative transport rate is experienced for the first waves and decreases as additional waves are passed over the test section.

To determine an estimate of the subsurface transport's approximate contribution to the transport measurements presented in section 5.2.1.2, the experimental cumulative subsurface transport can be calculated for a sediment bed which has had 25 waves pass over it. The slope of the average cumulative transport between the 15th and 35th waves gives an estimate of the net subsurface

transport per wave during this period. This estimate should be conservatively high because more than 25 waves had passed over the sediment bed previous to the total transport measurements.

The average cumulative subsurface transport is 4.4cm^2 and 5.5cm^2 at wave 15 and 35, respectively. The average subsurface transport per wave, q_{sw}, between the 15th and 35th wave can be estimated from:

$$q_{sw} = \frac{5.5 - 4.4}{35 - 15} = 0.06 \text{ cm}^2/\text{wave} \tag{103}$$

The subsurface transport (order ~ 0.1 cm^2/wave) is small compared to total transport reported in section 5.2.1.2 (order ~ 2.5 cm^2/wave). The subsurface transport component of the measurements of total transport can therefore be safely neglected.

5.3.1.2 Sensitivity of Theoretical Model to Sediment Density

To determine the effect of $(\rho_t - \rho)$ on subsurface transport, the theoretical model was used to determine the maximum depth of displacement, $\delta_{\max}$, and depth-integrated displacement, *As*, for 45 different combinations of sediment density, friction angle , and phase velocity. For reference, a porosity of $n = 0.37$, fluid density of $\rho = 1$ g/cm^3, and sediment densities of ρ_s = 1.16 and 1.4 g/cm^3 yields $(\rho_t - \rho)$ values of 0.1 and 0.25 g/cm^3 respectively.

Figure 59 shows the variation of the maximum depth of displacement, $\delta_{\max}$, with $(\rho_t - \rho)$ for each combination of phase velocity and friction angle. Figure 60 shows variation of the depth-integrated subsurface displacement, *As*, with $(\rho_t - \rho)$ for each combination of phase velocity and friction angle. Clearly, if a critical sediment density is exceeded no subsurface failure will occur.

This critical sediment density can be predicted by (2) using the maximum pressure gradient of the wave condition. As $(\rho_t - \rho)$ decreases below this threshold, δ_{max} and *As* both rapidly increase in a similar manner.

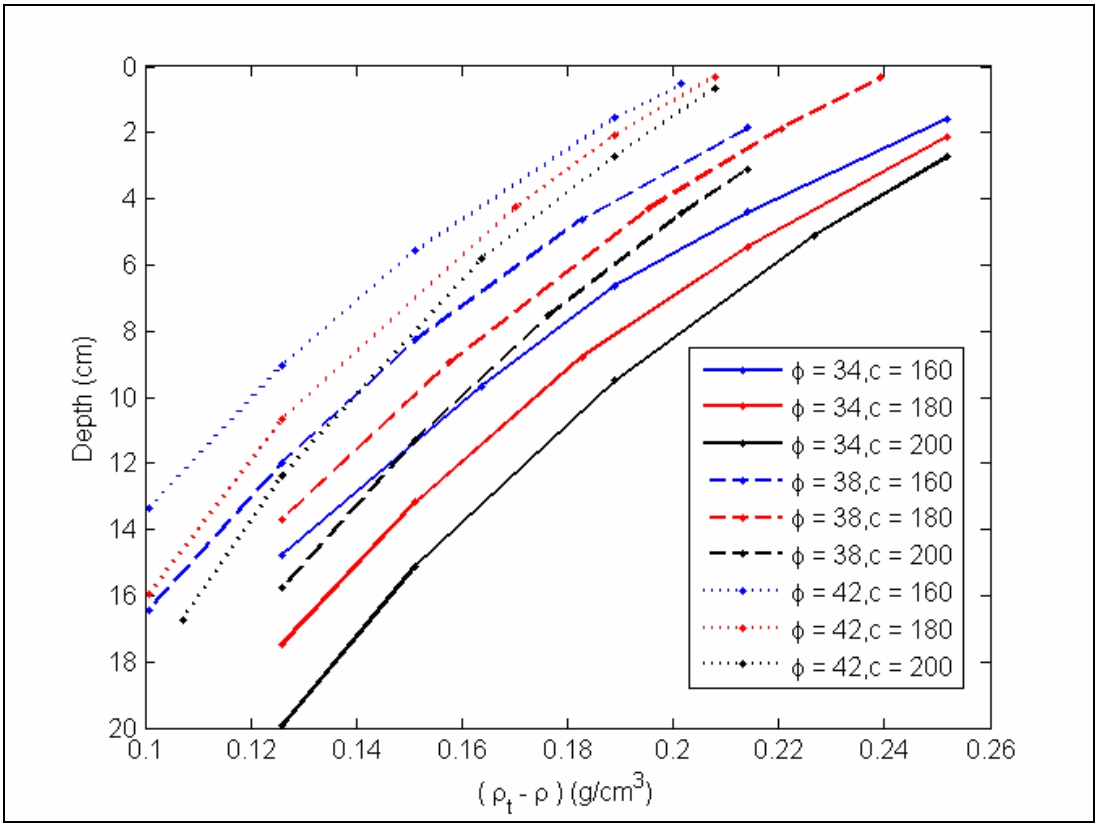

Figure 59 – Sensitivity of Theoretical Maximum Depth of Displacement to $(\rho_t - \rho)$, *c*, and ϕ

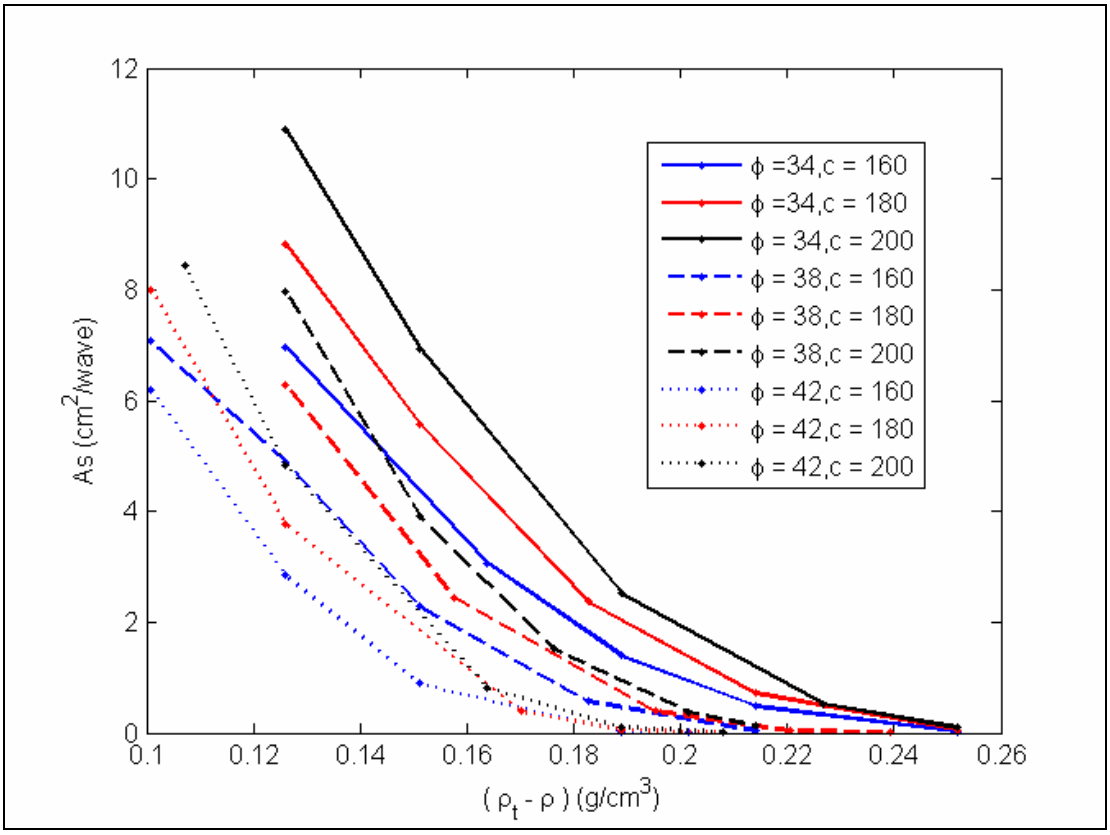

Figure 60 – Sensitivity of Theoretical Depth-Integrated Displacement to $(\rho_t - \rho)$, c, and ϕ

5.3.2 Three Wave Burst

Two experiments were conducted to determine the subsurface transport for the three-wave burst (TWB) condition. One experiment used PVC beads while the other utilized PET beads. This section shows results for both experiments.

5.3.2.1 Experiment with PVC Beads

Initial experiments measuring subsurface movement with the PVC beads showed excessive dependency on the length of time that the beads were immersed in water. In some initial experiments in which the beads had been in water for more than several hours no noticeable subsurface movements were observed. However, the experiment presented in this section was

completed soon after bead immersion, before the clear PVC beads turned opaque. The colored column width was roughly 25mm and contained no air bubbles.

Figure 61, Figure 62, and Figure 63 show the experimental deflections of the colored column along with the theoretical predictions using phase velocities of c = 140, 150, and 165cm/s respectively. The c = 140 cm/s phase velocity corresponds to the theoretical linear shallow water phase velocity, c = 150 cm/s corresponds to the experimentally measured phase velocity, and c = 165 cm/s corresponds to the theoretical cnoidal phase velocity. The experimental deflections show the forward excursion of the column during the passage of the wave crest, not incorporating backwards column movement. The experimental deflections of the first wave of the three wave burst are shown. The first wave's velocity data was also used for theoretical subsurface deflections. The measured values of porosity and sediment density for PVC beads (shown in Table 3) are also used in the theoretical calculations.

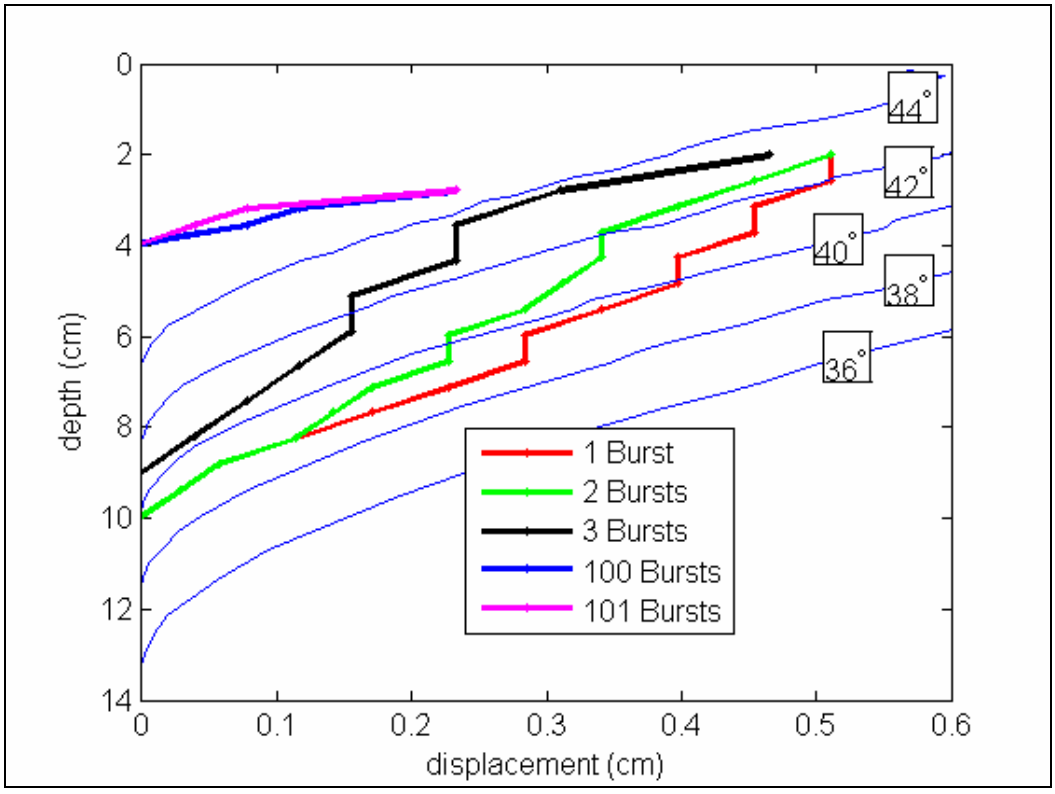

Figure 61 – TWB Displacements with PVC Beads using c=140 cm/sec

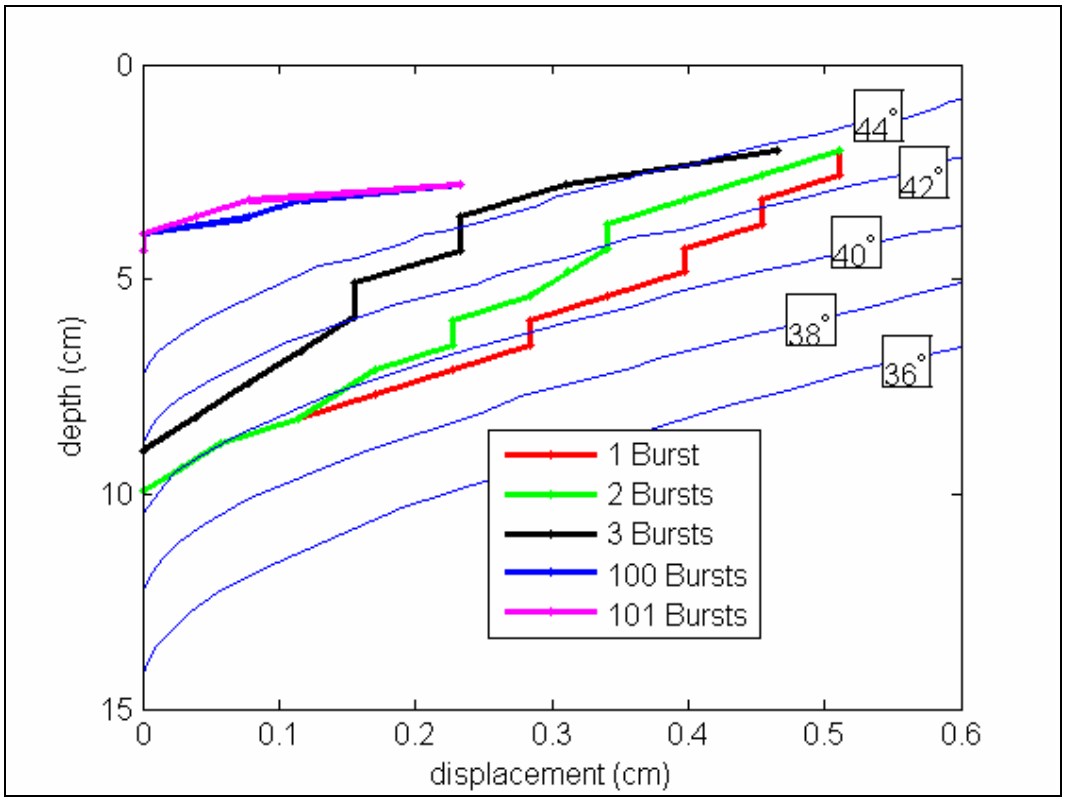

Figure 62 – TWB Displacements with PVC Beads using c=150 cm/sec

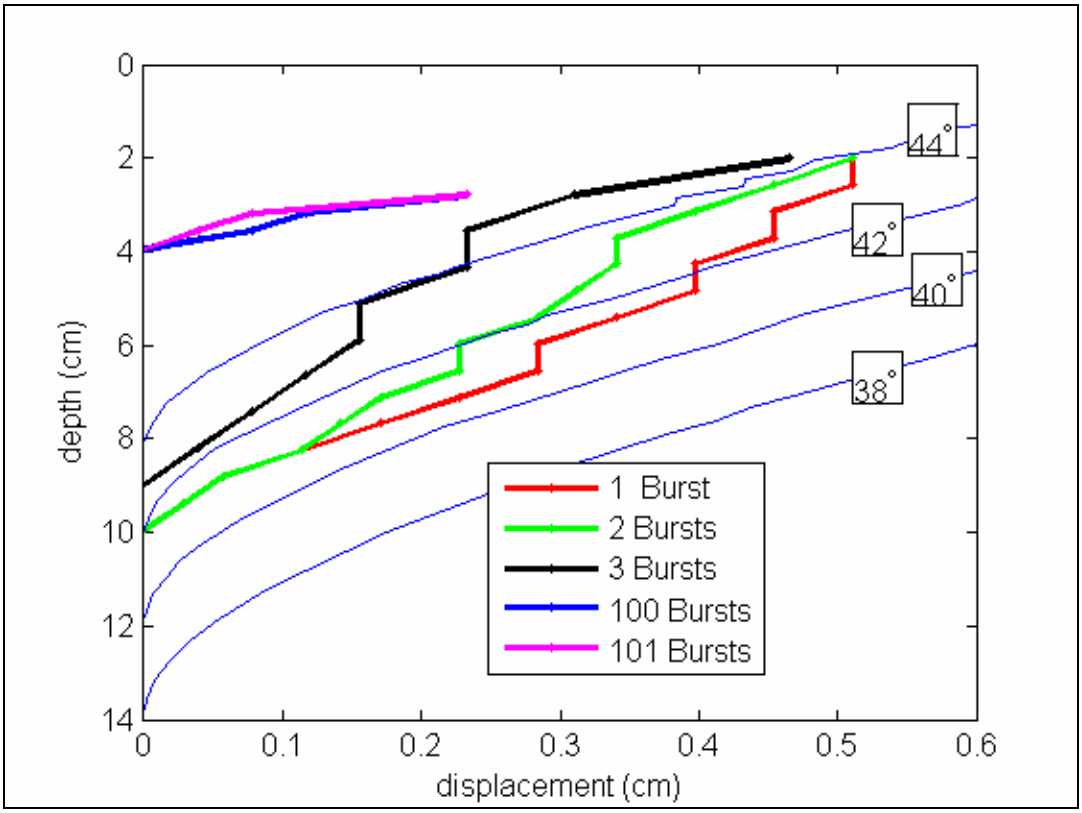

Figure 63 – TWB Displacements with PVC Beads using c=165 cm/sec

Similar to the solitary wave experiments, an attenuation of movement can be seen as the number of waves increased. The deflections after 100 waves were recorded after the beads had been immersed for several hours, it is likely that these deflections have been influenced by cohesive forces within the sediment bed. It can be seen that an increase in the phase velocity yields a rise in the theoretical maximum depth of displacement and forward displacement lengths, also similar to the solitary wave condition. However for this experiment, the friction angle of the theoretical displacements that correspond to the experimental displacements are much higher that for the solitary wave experiments using PET beads. It is suspected that the friction angle increases along with the change in bead color after submersion (noted in section 3.3.3), therefore, the results from this experiment are likely not typical of those of uncohesive sediments.

Figure 64 shows the variation of the maximum depth of displacement with the number of waves passed over a virgin sediment bed. The difference between the three waves show only a small change but by the 100^{th} wave a significant reduction in depth is noted.

Figure 65 shows the variation of the depth-integrated forward sediment movement with the number of waves passed over a virgin sediment bed. A sharp decrease in *As* is noted for the first three waves, further showing the attenuation of sediment movement for these first waves is quite dramatic. The decrease in forward movement per wave from wave 3 to wave 100 is much smaller. However, because of the relatively shallow deflections after 100 waves, it is not known if the integrated linear extrapolation provides a reasonable estimate of *As*. A large fraction of the deflection used to calculate *As* is from extrapolated data that estimates the position of the colored sediment column obscured by the false bottom.

Figure 66 shows the cumulative depth integrated transport as a function of number of waves passed over the test section. The second and third waves produced a negative net transport, moving the colored sediment column seaward. A relatively small amount of cumulative transport was recorded between the 3rd and 100th wave. This erratic behavior provides further evidence that the PVC beads do not yield predictable results.

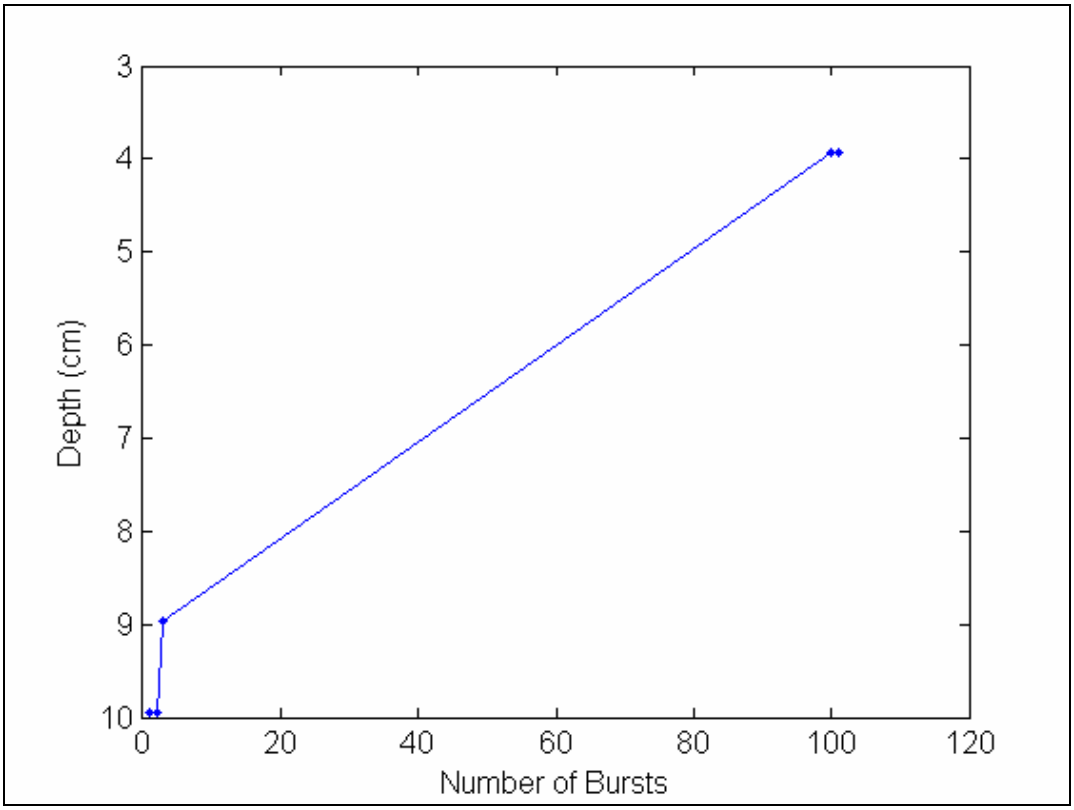

Figure 64 – Experimental Maximum Depth of Movement (TWB) with PVC Beads

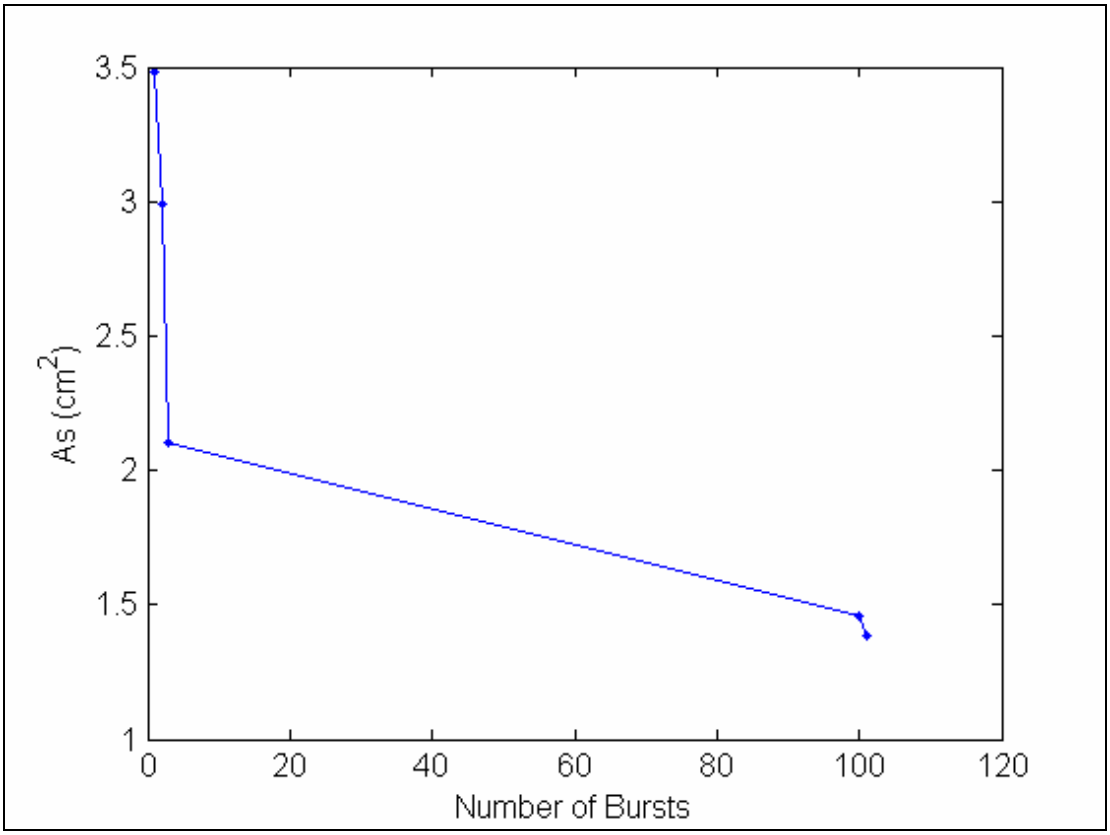

Figure 65 –Experimental Depth-Integrated Forward Excursion (TWB) with PVC Beads

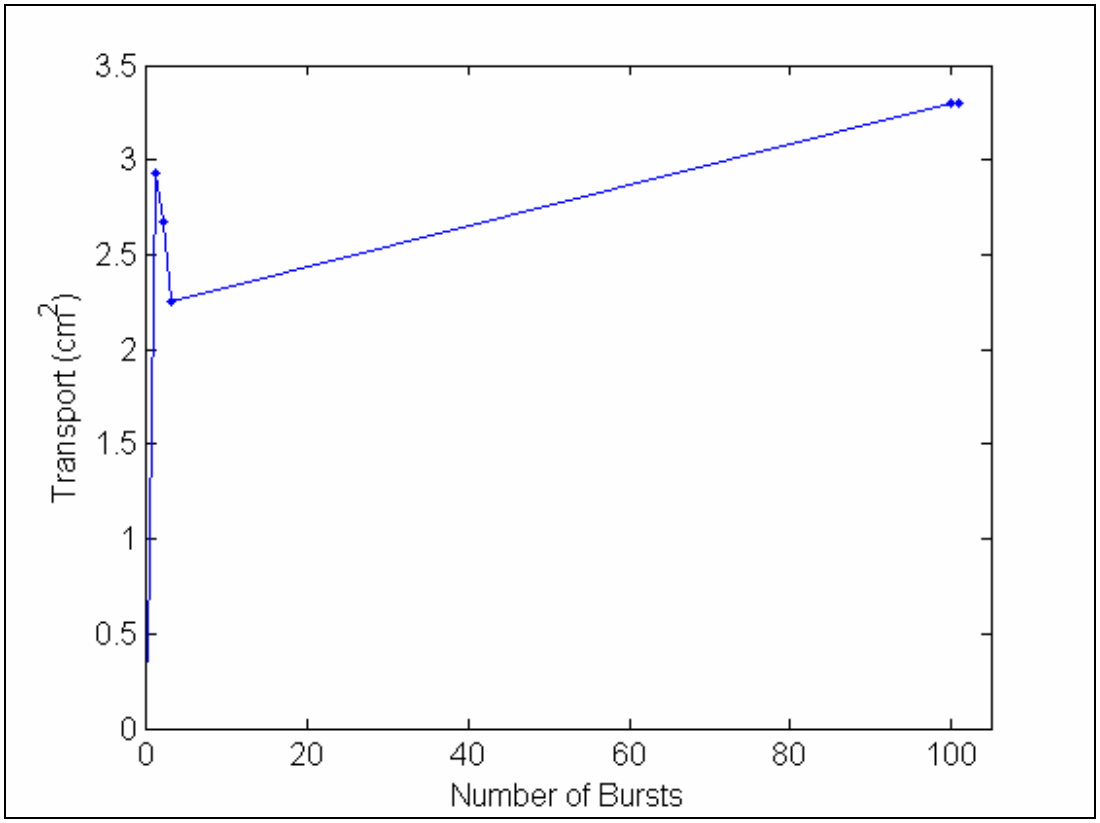

Figure 66 – Experimental Depth-Integrated Cumulative Displacements (TWB) with PVC Beads

5.3.2.2 Experiment with PET Beads

The results from the experiment using the three-wave burst wave condition with PET beads are presented in this section.

Figure 67, Figure 68 and, Figure 69 show the theoretical and experimental displacements for this experiment. Like the PVC experiment, the forward movements of the first wave of the three wave burst are shown. To calculate the theoretical subsurface displacements, the same phase velocities presented in section 5.3.2.1 were used for the theoretical calculation along with the porosity, sediment density, and diameter of the PET beads measured in section 3.3. The colored column was approximately 10mm wide and contained no air bubbles.

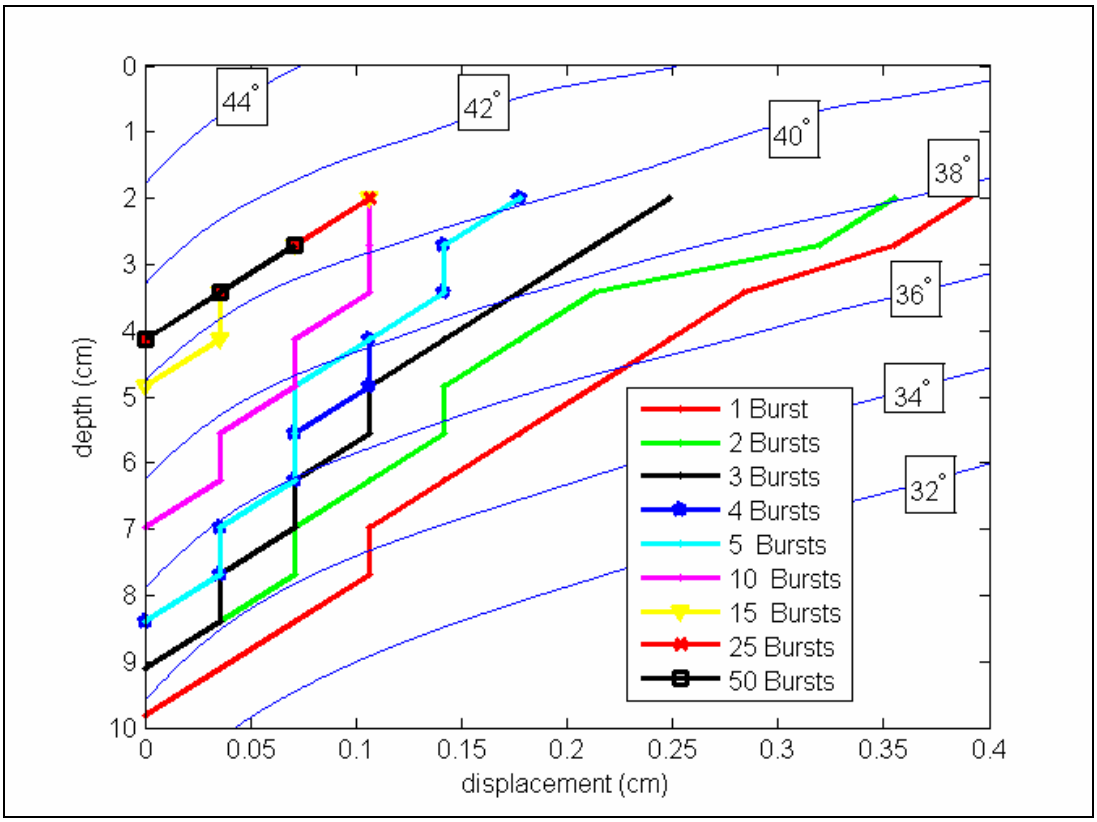

Figure 67 – TWB Displacements with PET Beads using c=140 cm/sec

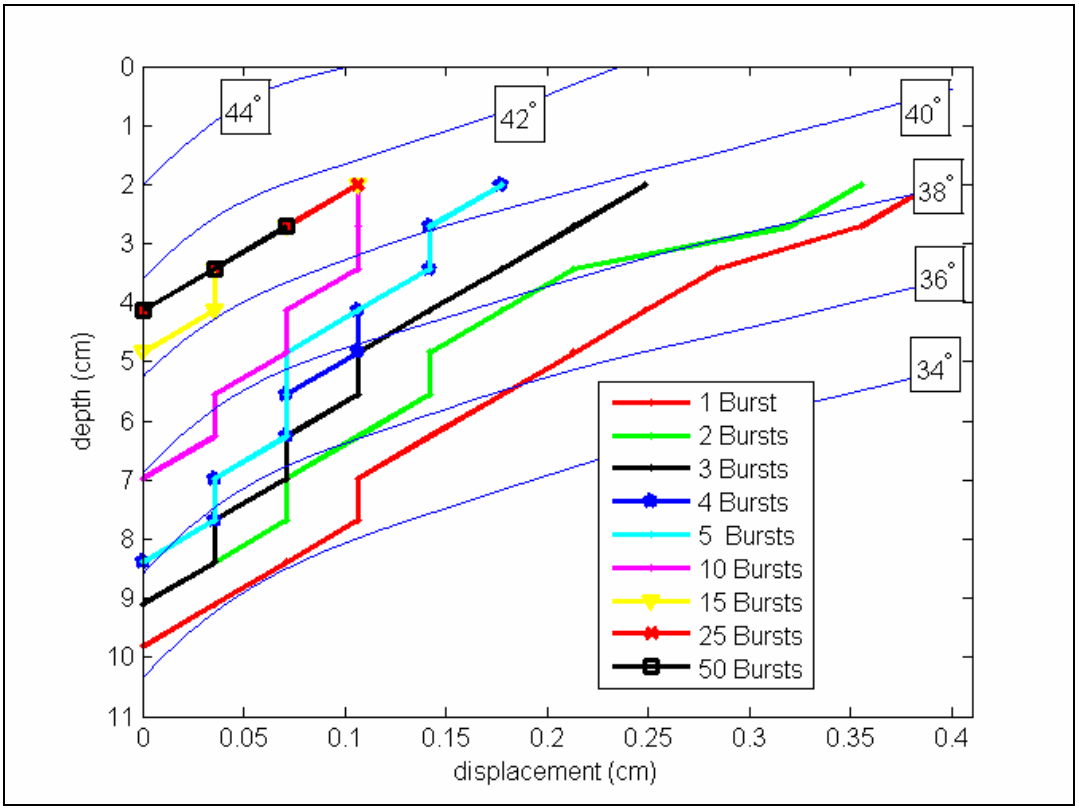

Figure 68 – TWB Displacements with PET Beads using c=150 cm/sec

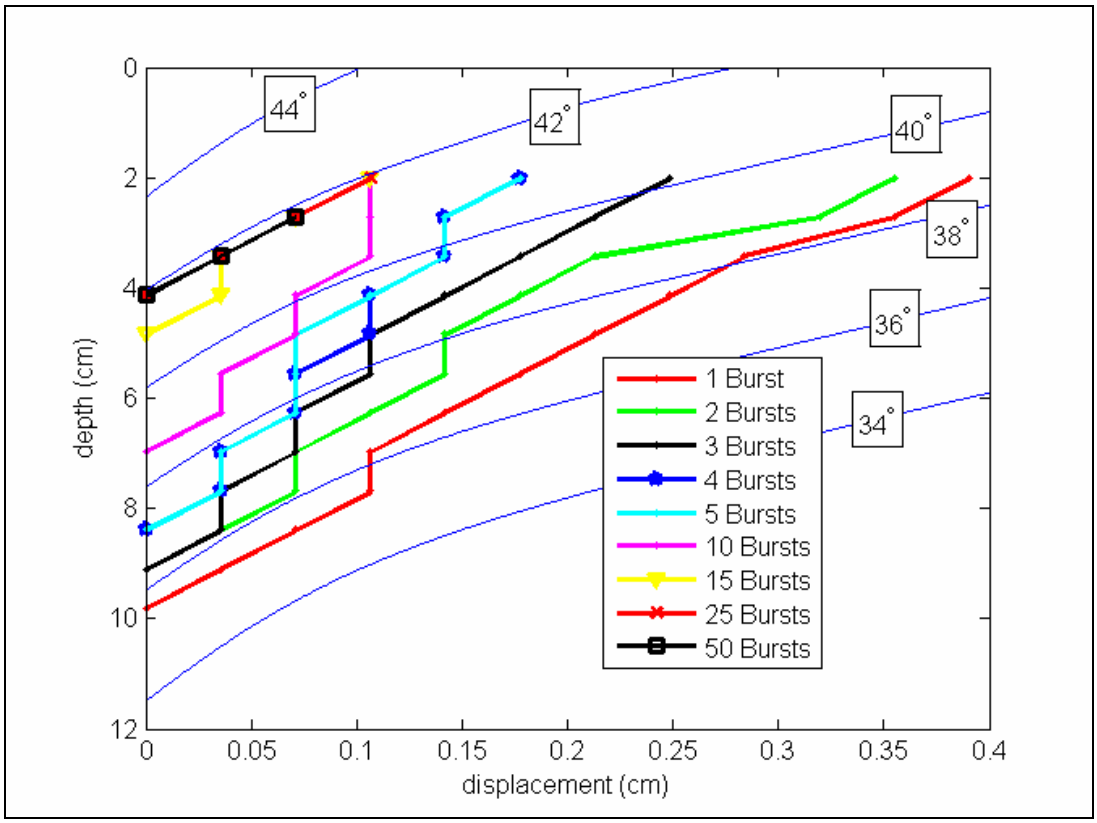

Figure 69 – TWB Displacements with PET Beads using c=165 cm/sec

The experimental displacements show attenuation as the number of waves passed over the virgin bed increases. Like the solitary wave experiments and TWB experiment with the PVC beads, the theoretical predictions seem to overestimate the experiment deflections when a friction angle is chosen such that the experimental and theoretical maximum depths of displacement are equivalent. The theoretical predictions of this experiment match the observed deflections for friction angles similar to those presented for the solitary waves in section 3.3.3 for the PET beads, unlike the TWB experiment using PVC beads.

Figure 70 shows the maximum depth of movement as a function of number of wave bursts passed over the bed. The theoretical measurements were made with a phase velocity of c = 150 cm/s. The maximum movement depth appears to get shallower until the 25th wave burst and then becomes constant, although more data points would be required to affirm this assertion. The friction angles presented Table 5 give good agreement between the theoretical and experimental results for the first ~15 waves. After ~15 waves the friction angle necessary to obtain good agreement ($\phi \sim 41.5^{\circ}$) is higher than the vibrated, submerged case presented in Table 5 ($\phi \approx 39^{\circ}$). This is very similar to what was obtained for the solitary wave condition.

Figure 71 shows the variation of the depth-integrated forward excursion, *As*, with the number of wave bursts. *As* decreases until the 15th wave burst and then is nearly constant, with similar values for the 15th, 25th, and 50th three-wave burst. The experimental results correspond with theoretical predictions using friction angles slightly higher than measured in Table 5. This can

be attributed to the theoretical model's overestimation of subsurface movements if a friction angle that matches the maximum depth of displacement is chosen.

Figure 72 shows the cumulative subsurface sediment movement. This figure shows the cumulative, depth-integrated subsurface movement, of the stationary colored column after both forwards and backwards movements. A large net movement occurs for the first burst, after which the transport per wave becomes smaller with each three-wave burst until the 10^{th} wave burst. Between 10^{th} and 50^{th} wave burst the cumulative transport per wave becomes nearly constant.

The proportion of subsurface transport occurring in the total transport measurements presented in section 5.2.2.2 can be estimated using the data in Figure 72. Fifty bursts had been passed over test section prior to the measurements. The cumulative subsurface transport after the 25^{th} and 50^{th} burst is 6.3cm^2 and 8.1cm^2 respectively. The approximate subsurface transport per burst, q_{sw}, between the 25^{th} and 50^{th} burst can be estimated from:

$$q_{sw} = \frac{8.1 - 6.3}{50 - 25} = 0.07 \text{ cm}^2/\text{TWB} \tag{104}$$

This value would give an approximation of the subsurface transport's contribution to the measurement of section 5.2.2.2 assuming that the cumulative transport rate can be extrapolated past the 50^{th} burst.

The net subsurface transport (order ~ 0.1 cm^2/TWB) is small compared to total transport presented in section 5.2.2.2 (order ~ 3 cm^2/TWB). The subsurface transport component of the measurements of total transport can therefore be safely neglected.

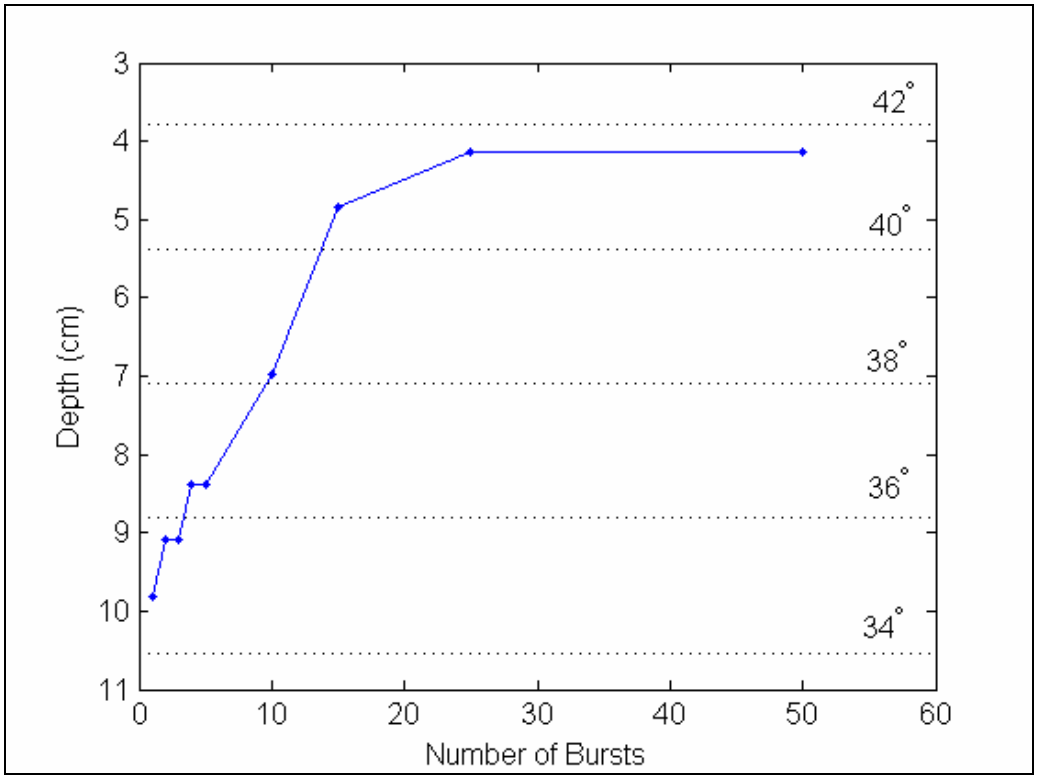

Figure 70 – Experimental Maximum Depth of Movement (TWB) with PET Beads

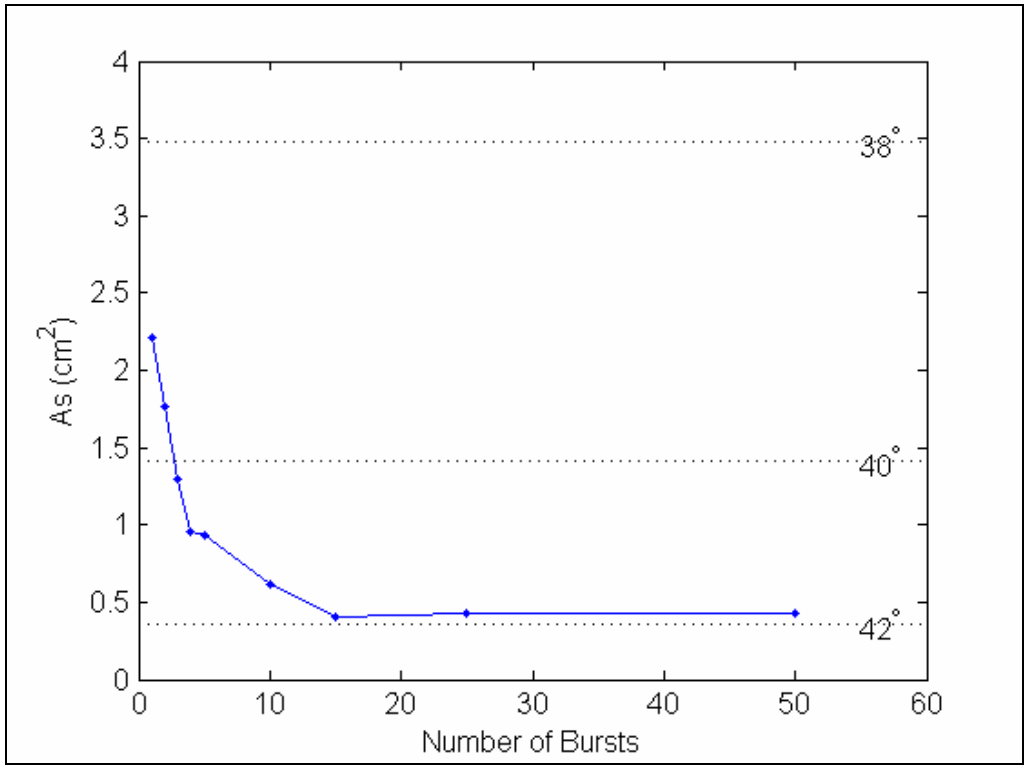

Figure 71 –Experimental Depth-Integrated Forward Excursion (TWB) with PET Beads

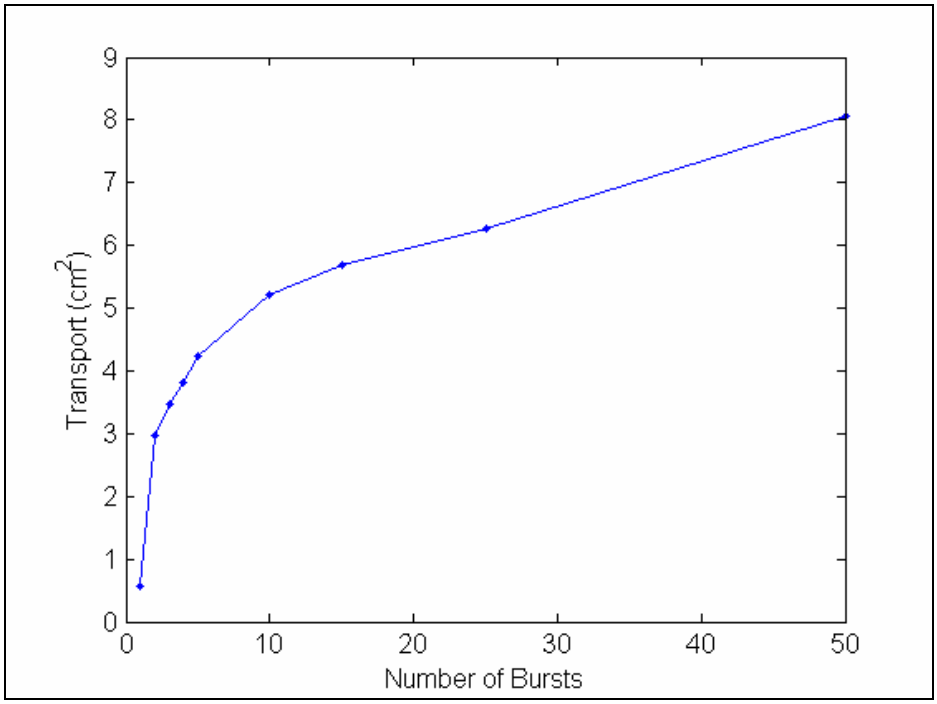

Figure 72 – Experimental Depth-Integrated Cumulative Displacements (TWB) with PVC Beads

5.4 PROTOTYPE WAVE

The wave presented in *Madsen* (1974) was scaled using three different prototype length scales to represent waves typical of calm, moderate, and stormy conditions. To account for the lack of knowledge of the model wave's phase velocity, three different model phase velocities that encompass the range of the theoretical and experimental estimates were used. The c = 50 cm/s is close to the phase velocity inferred by *Madsen* (1974), c = 100 cm/s represents the phase velocity predicted by linear theory. A phase velocity of c = 150 cm/s represents the probable upper bound for this wave condition.

The velocity and pressure gradient records for each prototype wave were developed using the relationships for a Froude scale model presented in section 4.2.5.

Table 16 shows the parameters of the model and prototype waves along with their respective length scales, *Lr*.

Table 16 – Model and Prototype Wave Parameters

	Unscaled Model Wave			Scaled Prototype Wave		
Lr	*c*	*T*	*H*	*c*	*T*	*H*
	(cm/s)	(sec)	(cm)	(cm/s)	(sec)	(cm)
8.54	50	0.95	5.9	146	2.8	50
8.54	100	0.95	5.9	292	2.8	50
8.54	150	0.95	5.9	438	2.8	50
25.6	50	0.95	5.9	253	4.8	150
25.6	100	0.95	5.9	506	4.8	150
25.6	150	0.95	5.9	759	4.8	150
68.4	50	0.95	5.9	414	7.9	400
68.4	100	0.95	5.9	827	7.9	400
68.4	150	0.95	5.9	1241	7.9	400

Table 17 – Theoretical Surficial Transport for Prototype Wave

	Scaled Prototype Wave			for Positive Velocities			for Negative Velocities			
Lr	*c*	*T*	*H*	A_{bm}	f_w	q_{b+}	A_{bm}	f_w	q_{b-}	q_b
	(cm/s)	(sec)	(cm)	(cm)		(cm^2)	(cm)		(cm^2)	(cm^2)
8.54	146	2.8	50	13	0.0127	0.19	27.2	0.0101	-0.088	0.098
8.54	292	2.8	50	25.9	0.0103	1.32	54.5	0.0084	-0.79	0.524
8.54	438	2.8	50	38.9	0.0092	3.9	81.7	0.0075	-2.47	1.42
25.6	253	4.8	150	38.9	0.0092	1.19	81.7	0.0075	-0.7	0.491
25.6	506	4.8	150	77.8	0.0076	7.88	163.4	0.0063	-5.16	2.72
25.6	759	4.8	150	116.7	0.0069	23.29	245	0.0058	-15.71	7.58
68.4	414	7.9	400	103.9	0.0071	6.16	218.2	0.0059	-3.99	2.17
68.4	827	7.9	400	207.8	0.006	40.16	436.5	0.0051	-27.59	12.6
68.4	1241	7.9	400	311.7	0.0055	119.44	654.7	0.0047	-83.66	35.8

Using the scaled velocity data, the theoretical surficial transport estimates were made using the methodology presented in section 4.2.2.2. A sediment density of ρ_s = 2.65 g/cm^3, fluid density

of ρ = 1.03 g/cm^3, sediment diameter of d = 0.03 cm, and kinematic viscosity of ν = 1.003x10^{-2} cm^2/s were used for all calculations.

Table 17 shows the equivalent excursion amplitude and wave friction factors for both the positive and negative velocities of the prototype wave as well as the total integrated bedload transport. It can be seen that both friction factors decrease as the length ratio increases. An increase in total transport can be observed for similar length ratio increases. Bedload transport occurs in both directions, therefore, the total, net transport depends in part on the difference between the wave friction factors (caused by wave asymmetry) and in part on the difference in wave velocity magnitudes under the crest and trough (wave skewness). The transport in the shoreward direction is denoted by (q_{b+}), whereas the seawards transport is given by (q_{b-}). The total, net transport is defined as $q_b = (q_{b+} + q_{b-})$. Aside from changes in the difference between the two friction factors, surficial transport is proportional to the bottom velocity cubed ($q_b \propto u^3$). From (96), the Froude velocity ratio, *Vr,* is equal to the square root of the Froude length ratio, *Lr*. Therefore, aside from changes in the difference between wave friction factors, the bedload transport should be proportional to $Lr^{3/2}$. This relationship is plotted in Figure 73. The bedload transport, q_b, appears to be nearly proportional to the length ratio raised to the power of 1.5. The effect of the change in difference between the friction factors is dominated by the proportionality of the bedload transport to the velocity record cubed.

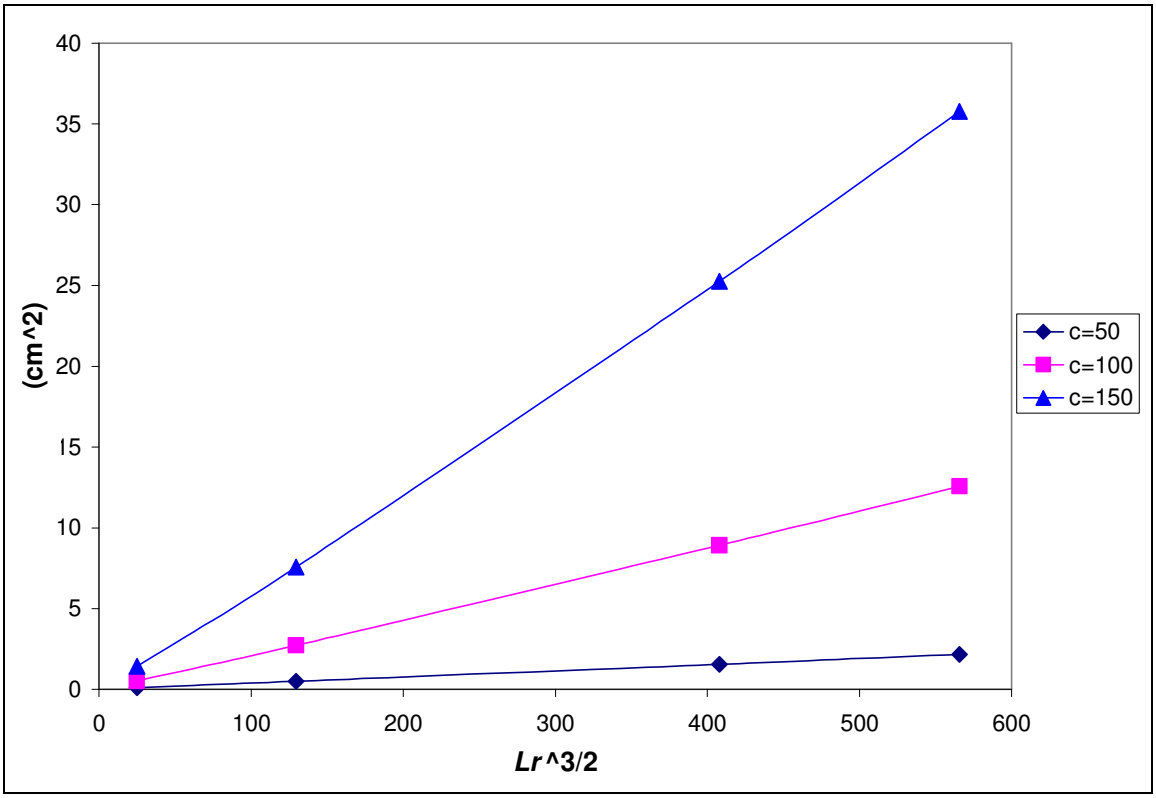

Figure 73 – Dependency of Prototype Surficial Transport on *Lr*

Using the scaled subsurface transport pressure gradient records, the subsurface displacements were calculated for the sediment and fluid characteristics one might encounter in a typical coastal environment. A sediment density of ρ_s = 2.65 g/cm^3, fluid density of ρ = 1.03 g/cm^3, and porosity of n = 0.35 was used for each of the theoretical subsurface movement simulations.

Table 18 shows the results of these simulations. To obtain the total subsurface transport, q_m, the following equation is used:

$$q_m = (1-n)As \tag{105}$$

where As is the depth integrated forward sediment movement from the maximum depth of displacement to the sediment-water interface. It should be noted that the integration of the

theoretical displacements require no extrapolation of data; the theoretical displacements are calculated from the maximum depth of displacement to the sediment-water interface.

Three different sediment friction angles were used in the simulations, ϕ = 32, 33, and 34 degrees. Because the wave condition presented in *Madsen* (1974), do not exceed the critical pressure gradient given by (2) for typical sandy sediment bed conditions by a large margin, the subsurface transport is highly dependent on the sediment's friction angle.

The ratio of subsurface sediment transport to surficial transport, q_m/q_b, is noted for each wave and sediment condition. This ratio gives a measure of the relative importance of subsurface transport. It can be seen for each combination of length scale and phase velocity the relative importance of the subsurface transport is wholly dependent on the sediment's friction angle. A friction angle of $\phi = 32^\circ$ yields a subsurface transport at least equal to that of the surficial transport. A friction angle of $\phi = 34^\circ$ yields a subsurface transport smaller than that of the surficial transport for each of the combinations shown.

To investigate how the two transport mechanisms vary with the length ratio, the proportionality of the subsurface transport parameters must to ascertained. Figure 74 shows the dependency of $\ell_{s\max}$ on *Lr*. Although some irregularities exist, the length of the limiting slip circle is nearly proportional to the length scale.

Figure 75 shows the dependency of the maximum depth of displacement with the length ratio. Again, a linear proportionality is noted.

Figure 76 shows the variation of *As* with Lr^2. It can be seen that the subsurface transport is approximately proportional to Lr^2. This is further proven by Figure 77 which shows four different subsurface deflections scaled by their respective length ratios. A friction angle of $\phi = 32^\circ$, sediment density of ρ_s = 2.65 g/cm^3, fluid density of ρ = 1.03 g/cm^3, porosity of n = 0.35 cm, and model phase velocity of c = 100cm/s was used to calculate these deflections. Both the depths and subsurface displacements have been scaled by the length ratio. Each of the scaled displacements has the same approximate size and shape. Because the surficial transport roughly scales by $Lr^{1.5}$ the subsurface transport should become more important as Lr increases. This trend is apparent in Table 18.

Table 18 – Theoretical Subsurface Transport for Prototype Wave

	Scaled Prototype Wave										
Lr	c	T	H	ϕ	h	$\ell_{s\max}$	$\delta_{\max}$	As	q_m	q_b	q_m / q_b
	(cm/s)	(sec)	(cm)	(deg)	(cm)	(cm)	(cm)	(cm^2)	(cm^2)	(cm^2)	
8.54	146	2.8	50	32	17.8	25.6	4.1	0.48	0.31	0.10	3.16
8.54	146	2.8	50	33	14.7	19.6	3.0	0.13	0.08	0.10	0.85
8.54	146	2.8	50	34	11.5	12.8	1.7	0.01	0.00	0.10	0.05
8.54	292	2.8	50	32	46.9	51.3	6.5	1.53	0.99	0.52	1.90
8.54	292	2.8	50	33	46.2	39.3	4.0	0.58	0.37	0.52	0.71
8.54	292	2.8	50	34	22.9	25.6	3.3	0.03	0.02	0.52	0.04
8.54	438	2.8	50	32	63.0	76.9	10.8	2.23	1.45	1.42	1.02
8.54	438	2.8	50	33	57.4	58.9	7.1	0.72	0.46	1.42	0.33
8.54	438	2.8	50	34	71.5	38.4	2.5	0.20	0.13	1.42	0.09
25.6	253	4.8	150	32	65.7	74.2	9.8	5.31	3.45	0.49	7.02
25.6	253	4.8	150	33	73.5	61.4	6.2	2.28	1.48	0.49	3.01
25.6	253	4.8	150	34	43.5	43.5	5.1	0.22	0.15	0.49	0.30
25.6	506	4.8	150	32	118.6	148.5	21.3	11.60	7.54	2.72	2.77
25.6	506	4.8	150	33	121.4	122.9	14.7	4.76	3.09	2.72	1.14
25.6	506	4.8	150	34	112.4	87.0	8.1	0.94	0.61	2.72	0.22
25.6	759	4.8	150	32	182.8	222.7	31.3	19.35	12.58	7.58	1.66
25.6	759	4.8	150	33	193.5	184.4	20.8	7.51	4.88	7.58	0.64
25.6	759	4.8	150	34	166.6	130.1	12.2	2.02	1.32	7.58	0.17
68.4	414	7.9	400	32	171.6	198.4	26.6	37.93	24.66	2.17	11.37
68.4	414	7.9	400	33	166.3	157.3	17.7	12.81	8.33	2.17	3.84
68.4	414	7.9	400	34	166.6	123.1	11.0	3.22	2.09	2.17	0.96
68.4	827	7.9	400	32	328.1	396.7	55.3	81.33	52.87	12.56	4.21
68.4	827	7.9	400	33	308.6	314.7	37.8	28.85	18.75	12.56	1.49
68.4	827	7.9	400	34	330.2	246.2	22.2	8.88	5.77	12.56	0.46
68.4	1241	7.9	400	32	498.6	595.1	82.0	140.31	91.20	35.78	2.55
68.4	1241	7.9	400	33	470.1	472.0	55.9	47.58	30.93	35.78	0.86
68.4	1241	7.9	400	34	493.8	369.4	33.4	14.29	9.29	35.78	0.26

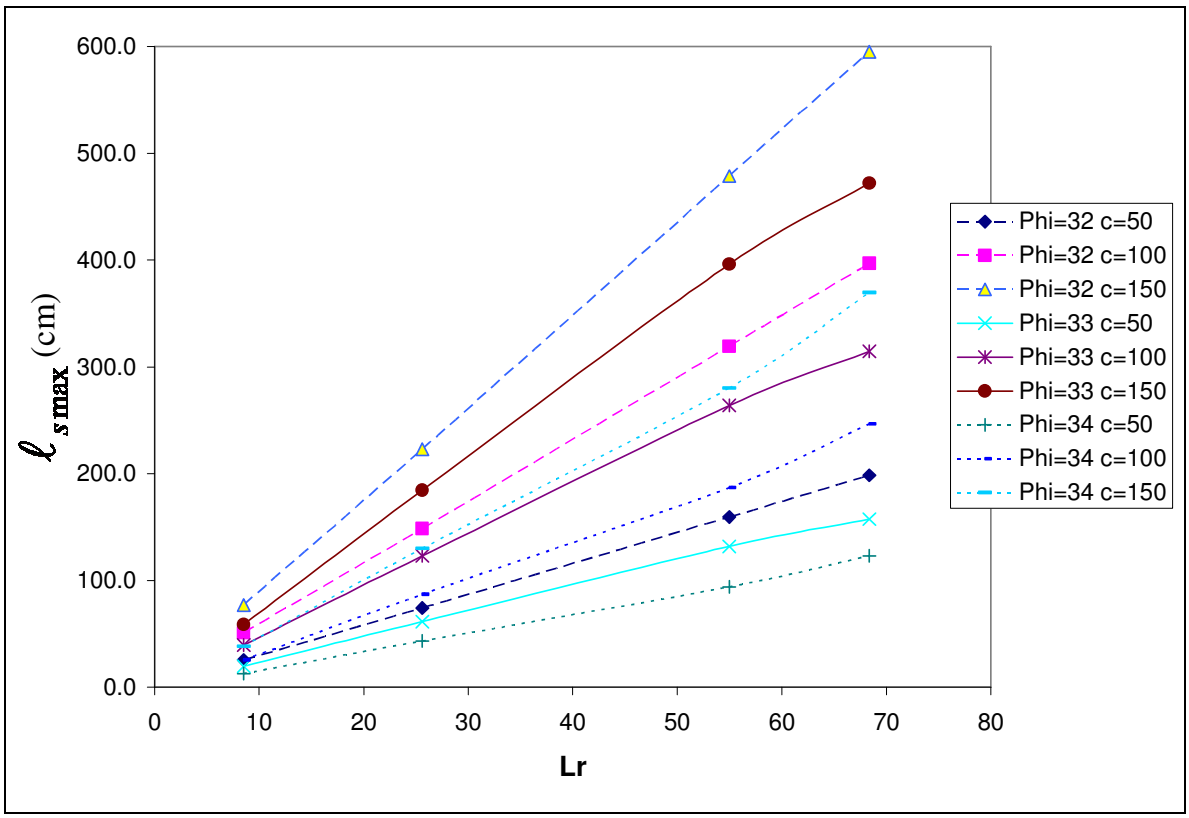

Figure 74 – Dependency of Prototype Slip Circle Length on *Lr*

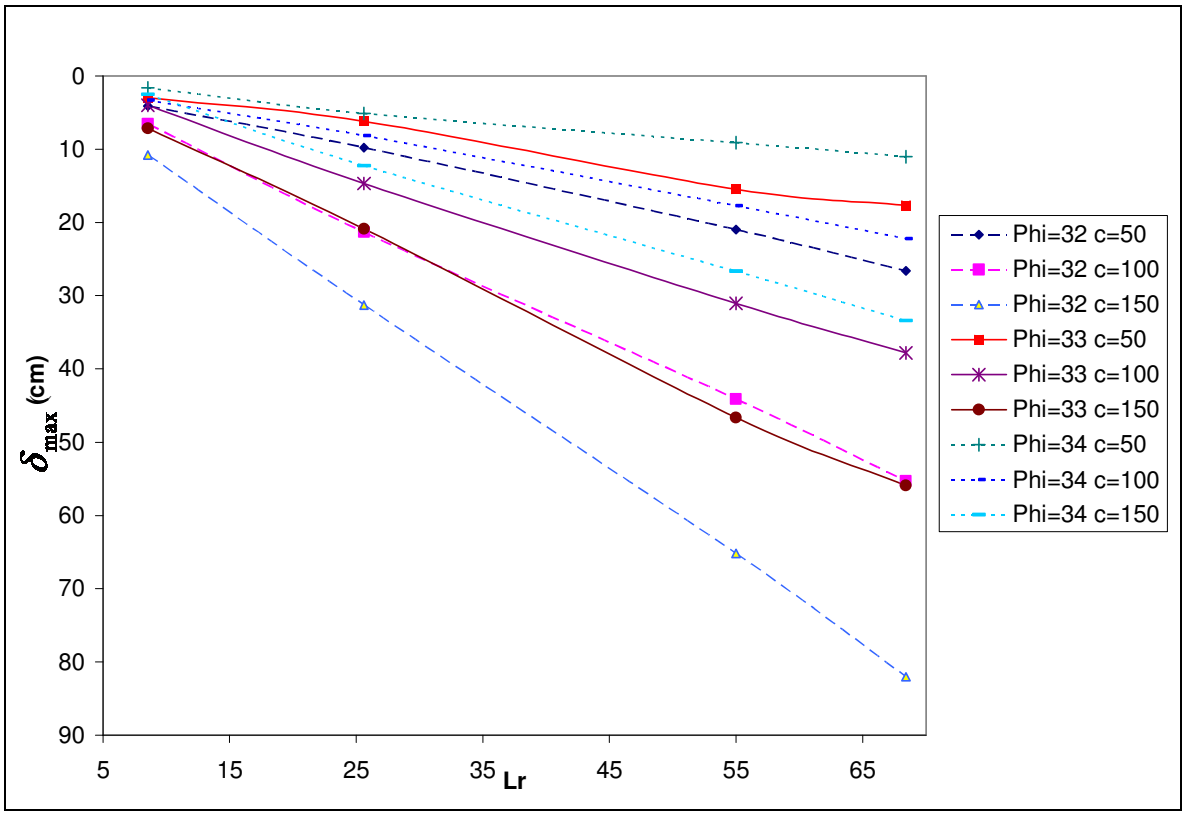

Figure 75 – Dependency of Prototype Maximum Depth of Movement on *Lr*

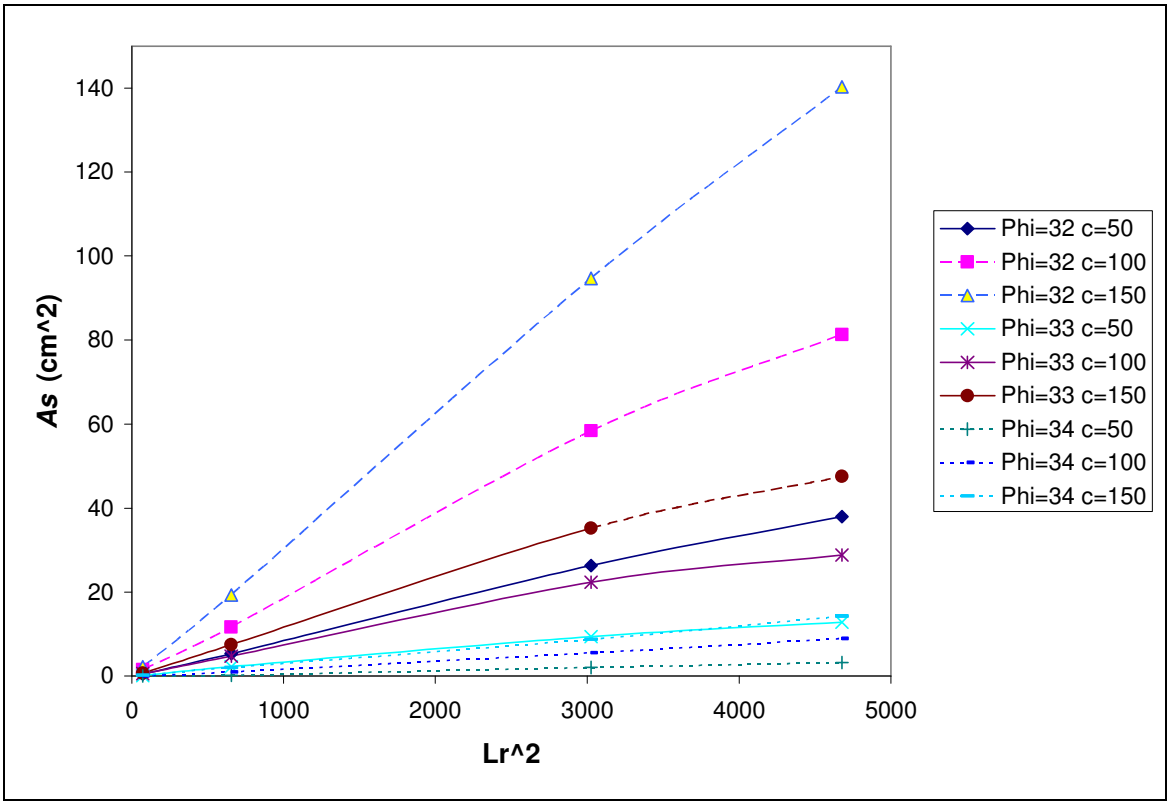

Figure 76 – Dependency of Prototype *As* on *Lr*

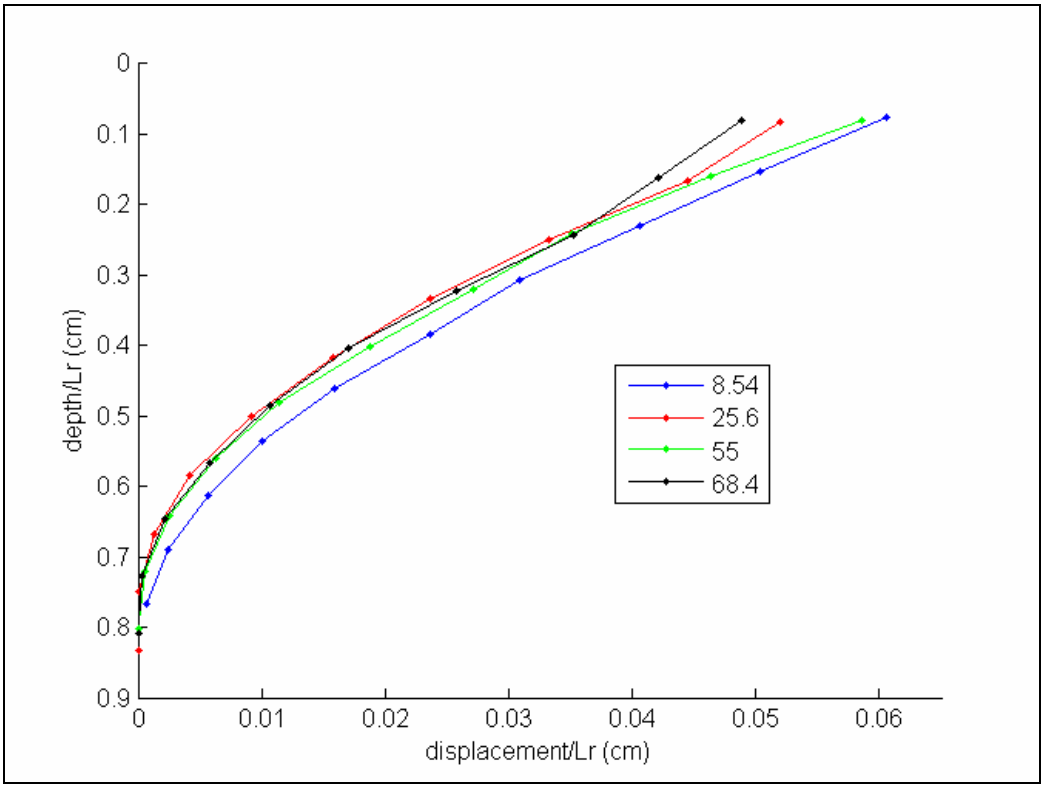

Figure 77 – Prototype Subsurface Displacements Scaled by *Lr*

6 – CONCLUSIONS

6.1 SUMMARY OF RESULTS

This thesis has presented both experimental and theoretical methods to measure and predict both subsurface and surficial sediment transport under near-breaking waves. Both subsurface and surficial transport was experimentally measured and predicted for the solitary wave and three wave burst. The validity of the theoretical models was tested by comparing the results of the theoretical models to experimental findings. Both theoretical models yielded good agreement with experimental observations. A laboratory wave condition presented in *Madsen* (1974) was scaled up to the size of waves one might encounter in the field. The quantities of both types of transport were estimated using the theoretical models. Subsurface transport was found to be proportional to the length scale squared while surficial transport is proportional to the length scale to the power of 3/2.

6.1.1 Surficial Transport

The experimental surficial transport under the solitary wave condition became nearly constant over the downwave half of the sediment tray, as predicted by calculations of theoretical bead excursion lengths. The surficial transport decreased as the number of waves passed over a newly smoothed sediment bed increased. This phenomenon is likely the result of the waves agitating the sediment bed, strengthening it in the same manner as the mechanical vibrations in section 3.3.3.

The theoretical surficial transport was calculated by a method which accounts for the enhanced shear stress under the wave crests and utilizes a Meyer-Peter and Mueller (MP-M) type bedload equation (*Madsen*, 1991). This method is expected to overestimate the surficial transport for the solitary wave condition as it uses the friction factor estimated using the velocity rise for the entire wave. Upon contrasting the experimental and theoretical estimates, the theoretical prediction of surficial transport proved to be conservatively high as expected. The coefficient of 14 used in the MP-M equation was developed by dividing a semi-theoretical constant of 8 by the tangent of the sediment angle of moving friction, ϕ_m, which was taken to be $\phi_m = 30^\circ$. If it is assumed that this angle increases in a manner similar to the vibrated sediment samples (section 3.3.3) it is clear that a decrease in sediment transport could be expected as more waves passed over a smoothed sediment bed.

The TWB also achieved a near constant experimental transport over the down wave portion of the sediment tray. The theoretical methodology produced an estimate slightly smaller than experimental observations. Given the highly approximate nature of sediment transport predictions, the theoretical model proved to be surprisingly good for both wave conditions.

6.1.2 Subsurface Transport

Estimates of the bottom pressure gradient beneath a breaking wave were made from laboratory measurements of velocity for the three-wave burst and solitary wave conditions. Building on the theoretical model of *Madsen* (1974), a method was developed that predicts the movements of subsurface sediments that undergo a soil-mechanics type failure. Experimental observations of subsurface sediment movements contained two anomalies that might not be as pronounced in the

field. First, the beads beneath the sediment-water interface moved first in the direction of wave propagation and then moved back in the opposite direction. The movement back was not anticipated. Second, there was a marked decrease in subsurface sediment deflections as the number of waves that had been passed over a newly constructed sediment bed increased. The bed's properties apparently changed over the course of the experiment.

6.1.2.1 Subsurface Sediment Seaward Movements

The pressure gradient records of the solitary and TWB wave condition (Figure 6 and Figure 9) show a significantly larger magnitude pressure gradient ahead of the wave crest than following the passage of the wave crest. The positive pressure gradient after passage of the wave crest is theoretically not large enough to create a subsurface failure as defined by (2) for the beads used in this study. However, seawards sediment movement can possibly be attributed to two factors. First, when the sediment column moves forward, prior to the passage of the wave crest, the sediment bed experiences an increase in porosity. The increase in pore space can be seen in videos by observing a slight upward movement (~1mm) in the shallower depths of the sediment tray during their shoreward excursion. This phenomenon was also quantitatively measured in the experiments *Flores and Sleath* (1998) and *Dick and Sleath* (1991) who used similar plastic beads. This increase in porosity surely affects intergranular particle interactions, and would likely reduce the "instantaneous" internal angle of friction. This reduction in friction angle would make it much easier for the small pressure gradient after passage of the crest to move the subsurface sediment seawards. Dilation of the sediment bed is not considered in the theoretical subsurface model presented in this thesis.

Second, the sediment deflections experienced in the laboratory are not large enough to allow individual sediment grains to slide past one another; a true soil-mechanics type failure is not experienced. To allow one sediment grain to move fully past another particle directly above or below, the slope of the deflection: $\frac{d(deflection)}{dz}$ must be greater than one. This would be considered the minimum slope that would have to be exceeded to before a true soil mechanics type failure would occur. For each model and prototype deflection presented in this thesis, the slope of the deflection is well below one. However, it is possible that a breaking wave in the field could produce a pressure gradient record that yields a subsurface sediment deflection with a slope larger than one. In this thesis, only laboratory waves that are breaking on a horizontal or 1:10 slope are examined. In the field, a gentler slope might allow a shoaling wave to develop a pressure distribution capable of producing a deflection with a slope greater than one. In the experiments presented in this thesis, the slope of the deflections of the colored sediment column is approximately ~1/25.

Figure 78 shows the difference between the subsurface sediment movements encountered in the laboratory and those which could possibly exist in the field. Two adjacent layers of subsurface sediments in failure are shown. For illustrative purposes, the reference frame of the cartoons moves along with the bottom sediment layer (half circles). The relative position of the two layers is shown at three different times: before movement occurs (a), at the maximum shoreward excursion (b), and at the final position after the wave has passed by (c). In the laboratory, the forward excursion is not large enough to move one sediment layer more than one diameter relative to an adjacent layer. The result is a sediment bed which is unstable, allowing a relatively weak positive pressure gradient of to nearly return it to its original position. However, in the field it is possible that the relative movement between two adjacent sand grains could be much

larger than a typical sand grain diameter. A small amount of seaward movement might be sustained but is likely to be negligible in relation to the large forward displacement.

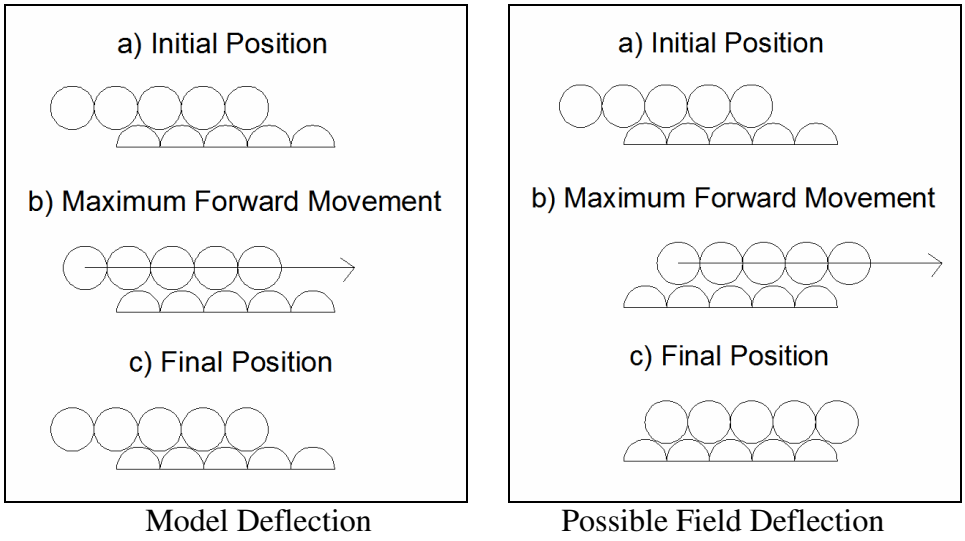

Model Deflection Possible Field Deflection

Figure 78 – Difference Between Model and Possible Field Subsurface Sediment Movements

Gollub and Pine (2006) performed an experiment on the reversibility of systems in which they placed granulated material, $d = 200\mu m$, in the gap formed between two concentric cylinders. The inner cylinder was rotated a specific number of degrees and then rotated back to its original position. The positions of individual particles were tracked throughout the experiment. It was found that below a critical rotation threshold the positions of the beads were reversible; returning the beads to their initial position. However, if the inner cylinder was turned past this threshold the particles did not return to their initial positions; the process was irreversible.

It is suspected that for the subsurface deflections in the laboratory, sediment excursions are still within the reversible limit; they almost return to their initial position after the shoreward movement, leaving the colored sediment column almost unchanged. If a true failure was to occur, the colored sediment column would likely no longer have clearly defined interfaces with the clear plastic beads after the forward excursion. These interfaces would be scattered as a

result of colored and clear sediment grains exchanging places with one another, creating an irreversible state.

6.1.2.2 Attenuation of Subsurface Movements

In each of the experiments, an attenuation of subsurface movement is seen as additional waves were passed over a newly formed sediment bed. This attenuation occurs both for the forward excursion and the net movement (forward excursion minus reverse excursion). This obvious change in the sediment bed is accounted for in the theoretical simulations by increasing the friction angle of the sediment. Similar increases in the friction angle were seen after samples of beads were mechanically vibrated (section 3.3.3). For the PET beads the theoretical predictions corresponded well to experimental observations using friction angles within the range of those measured in 3.3.3. There were indications, however, that the PVC beads became cohesive after submersion. The results of this experiment can be considered spurious.

Groot et. al. (2006) notes a soil element "behaves quite differently" the first time it is loaded in comparison to subsequent loadings. During the first loading sediment grains redistribute and change positions. They do not return to their original positions during unloading. Subsequent loadings do to not experience similar redistributions. The initial deformations are therefore plastic, while subsequent loading/unloading cycles produce elastic deformations.

It should be noted that *Groot et. al.* (2006) is not a paper concerned with ~10 cm waves passing over lightweight plastic bead beds, but instead large-marine structures with much higher soil element stresses. Although *Groot et. al.* (2006) categorizes the loadings into two discreet bins, the initial, virgin loading and all subsequent loadings, it can be reasoned if the loadings were

small, the switch from plastic to elastic deformation might occur over many loading/unloading cycles.

In the experiments, the initial subsurface deformations experience a plastic deformation with intergranular redistributions during each loading. After many waves, the sediment grains reach a preferred position yielding a bed stronger than the initial, virgin bed. During this rearrangement the sediment particles move to positions slightly downwave which can be seen in the cumulative (forward minus backwards) depth-integrated displacements. The change in the cumulative depth-integrated displacement per wave is large for the first ~20 waves but becomes much smaller for subsequent waves. This transition point is indicative of the transition from plastic to elastic deformations. Once the sediment bed has reached an elastic state, the forward movements have become much smaller, as the particles have realigned themselves into a stronger state. This transition can be adequately characterized by an increase in the friction angle.

6.1.3 Correlation of Experimental and Theoretical Results

For experiments using PET beads, the theoretical model produces subsurface sediment deflections that are similar to those observed experimentally using friction angles comparable to those measured in section 3.3.3. Because the phase velocity of a breaking wave is neither uniform nor constant, the theoretical results are presented using several different phase velocities for each experiment. A significant shortcoming in the theoretical method is the use of the phase velocity to transform velocity derivatives, pressure derivatives, and pressure distribution domains back and forth from time to space. An experimental setup including multiple pressure transducers or a single moveable pressure transducer could avoid the inherent inaccuracies of using a single phase velocity to make these transformations.

A potential problem of the experimental setup is that the thickness of the sediment layer overlying the visible portion of the colored column is not constant. Surficial transport erodes the sediment layer overlying the colored column, necessitating that the sediment be replaced several times during the course of an experiment. This layer of overlying sediment is not visible from the side of the wave flume; it is always assumed to be exactly 2cm thick. When this layer has eroded slightly, the depths at which experimental subsurface deflections are measured have been overestimated. This means that the experimental deflections shown throughout this study might actually have occurred at a shallower depth. However, the maximum discrepancy in depth is likely to have a maximum of ~1cm because the sediment elevation above the colored column was monitored and replaced when necessary. Like all measures of sediment transport, the experimental results show some variation from one experiment to the next.

In comparing the theoretical deflections to the experimental results, two metrics can be used to analyze effectiveness of the theoretical model: the correlation of maximum depth of the displacements and the correlation of the sediment forward excursion distance at each depth. If a friction angle is chosen such that the theoretical maximum depth of displacement matches the experimental maximum depth of displacement, the theoretical displacement lengths usually overestimate the experimental displacement lengths by a small amount. Overall, however, the predictive accuracy of the theoretical model is quite good, especially given the simplicity of the theoretical model. Unlike the much more complex model of *Drake and Calatoni* (2001), this model does not take into account any complex intergranular interactions.

6.1.4 Transport Under the Prototype Wave

The estimates of surficial and subsurface transport were made by scaling a wave presented in *Madsen* (1974). Velocity record estimates were made using water surface elevation records and pressure gradient records were estimated from differential pressure transducer data. Three different scaling factors were used to generate waves of various sizes typical of the surfzone using Froude modeling relationships. Due to uncertainty in the model wave condition's approximate phase velocity, three different phase velocities were used that should encompass the range of plausible phase velocities.

Not surprisingly, theoretical surficial transport was found to be roughly proportional to the length scale raised to the power of 1.5, which can be easily demonstrated analytically for cases in which a constant friction factor is used. Because the difference between the two friction factors used in these calculations do not scale uniformly with the length scale, some variation in the above proportionality is expected.

The slip circle length, maximum depth of displacement, and forward excursion were all found to be proportional to the length scale. Consequently, the subsurface transport was found to be proportional to the length scale squared. Therefore, if a given wave condition is scaled, preserving the Froude number in both model and prototype, the ratio of subsurface transport to bedload transport can be expected to increase as the size of the wave increases. However, because in real-life large and small waves will undoubtedly have unique pressure distributions and velocity records that cannot be scaled using simple arguments, this statement is very approximate.

Because the critical pressure gradient is only exceeded by a small margin, the subsurface transport estimated for the prototype wave is extremely sensitive to changes in friction angle when using sediment characteristics typical of a sandy sediment bed. This extreme sensitivity is unlikely to occur in the field in which bottom undulations, sediment bed inhomogenities, and bottom pressure gradients that exceed the critical threshold by a large margin can be present.

Table 17 and Table 18 show that surficial and subsurface transport quantities could be of the same order of magnitude for conditions typical of a surfzone. However, many assumptions were made in the calculation of both modes of transport. The estimates of each type of transport beneath the prototype wave can only be expected to give approximate, order of magnitude estimates under the best of circumstances. A major assumption in the estimates of prototype subsurface transport is that no "rebound" of sediments occurs in the seaward direction, as was seen in laboratory experiments. If a large seaward rebound occurred in field a considerably smaller magnitude of net subsurface transport would be sustained.

In the coastal environment, sediment transport rarely occurs on a horizontal plane. The inclination of beaches should be considered when making estimates of sediment transport in the field. If a breaking wave (with a large negative pressure gradient) is traveling down a slope, the transport down the slope will be enhanced, whereas, transport up the slope will be reduced if the same wave travels up a slight inclination.

All transport estimates in this thesis assume a horizontal beach. The model wave condition, obtained from *Madsen* (1974), broke on a 1:10 slope; however, the prototype's transport magnitudes were calculated for a horizontal sediment-water interface. This discrepancy likely

introduces error into the results as a wave that breaks on a level plane will surely have a different velocity and pressure-gradient record than one that breaks on a slope.

To estimate subsurface transport, taking into account the inclination of the sediment-water interface, several modifications must be made to the methodologies presented in 4.2.4. The critical pressure gradient, which must be exceeded for subsurface failure to occur, can be re-derived using a force balance incorporating a sloping bottom.

The following formula gives the critical pressure gradient for a sediment bed as a function of β, the inclination of the sediment-water interface from the horizontal:

$$\left(-\frac{\partial p}{\partial x}\right)_{cr} = (\rho_t - \rho) g \tan(\phi)\left(1 + \frac{\tan\beta}{\tan\phi}\right) \tag{106}$$

which is the same as (2), except for the term, $\left(1+\frac{\tan\beta}{\tan\phi}\right)$. Figure 79 gives a depiction of subsurface movement up an incline. The following sign convention is used: β is positive for transport up an incline and β is negative for transport down an incline.

Given the maximum magnitude of a breaking wave's pressure gradient and typical sediment parameters, (106) can be used to determine the critical slope, β_{cr}, in which an equilibrium between seepage, gravitational, and intergranular forces is achieved. With an inclination above β_{cr} a failure of the sediment movement will not occur up the slope, beneath this threshold a failure will occur. For the prototype wave ($\left(\frac{\partial p}{\partial x}\right)_{\min}$ = -770 g/(cm s^2)) , a critical slope of β_{cr} = 5.7° (or roughly 1:10) would be sufficient to stabilize the sediment bed using typical sediment

parameters ($\rho_t - \rho = 1.08$ g/cm^3 and $\phi = 32^\circ$). Shoreward subsurface transport would attenuate to zero as the angle of inclination is increased from 0° to $\beta_{cr.}$

Conversely, the effect of slope could increase subsurface sediment transport when a wave breaks down a slope, as would occur on the lee side of a sandbar. Overall, slope is expected to play a substantial role in subsurface transport.

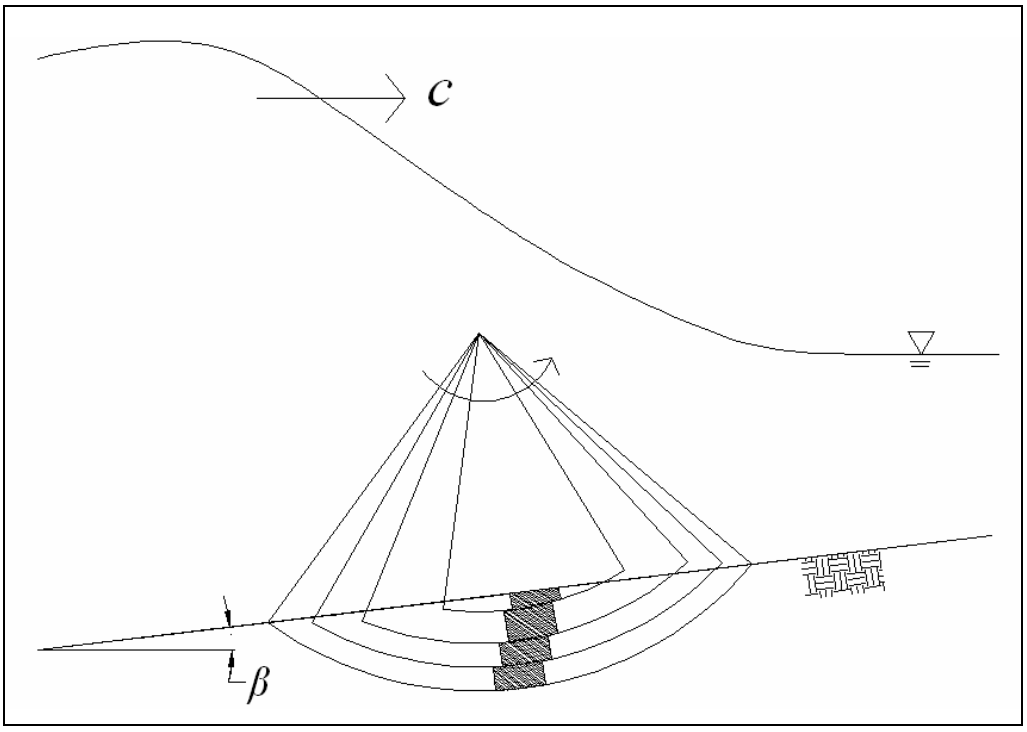

Figure 79 – Subsurface Deflections on a Slope

6.2 AREAS OF FUTURE RESEARCH

The experimental and theoretical methods presented in this thesis only begin to scratch the surface of what we are capable of understanding about sediment transport under breaking waves. Measurements of subsurface sediment movement in the field would be very useful to confirm the theoretical model presented in this thesis. As a starting point, the field observations of *Foster et. al.* (2006) provides breaking wave velocity and pressure gradient records as well as the

movements of the upper two centimeters of the sediment bed. However, the sediment within these upper two centimeters could still be considered in the bedload regime.

In the laboratory, the effect of the bottom surface slope on both types of transport could be investigated by placing the sediment tray on an incline. The effects of different sediment densities and diameters could also be ascertained by performing experiments with several types of lightweight sediment. The use of a differential pressure transducer would allow direct measurement of pressure gradients instead of relying on estimates derived from the velocity record. Several differential pressure transducers would allow researchers to avoid transformations using phase velocity. An approximate analytical solution to the theoretical subsurface model using well-defined wave and sediment parameters would also prove useful to avoid lengthy numerical computations.

The theoretical models could also be refined. Using knowledge of boundary layer dynamics, the analytical surficial transport model could be made more sophisticated. By incorporating more processes into the theoretical subsurface transport model this could similarly be refined, without reaching the complexity and computational demands of a grain-grain interaction model.

BIBLIOGRAPHY

Carter, J. D. "Experiments on Waves and Currents Over a Movable Bed." M.Sc. Thesis. MIT. 2002.

Conley, D.C. and D.L. Inman. "Field Observations of the Fluid-Granular Boundary Layer Under Near-Breaking Waves." *Journal of Geophysical Research*. 97, 9631-9343. 1992.

Day, C. "Sea-Level Rise Exacerbates Coastal Erosion." *Physics Today.* February 2004.

Dick, J.E. and J.F.A. Sleath. "Velocities and Concentrations in Oscillatory Flow Over Beds of Sediment." *Journal of Fluid Mechanics.* vol. 233. 1991.

Dong, C. and Huang, C. "Generation and Propagation of Water Waves in a Two-Dimensional Numerical Viscous Wave Flume." *Journal of Waterway, Port, Coastal and Ocean Engineering.* (130). 2004.

Drake, T.G. and J. Calatoni. Discrete Particle Model for Sheet Flow sediment Transport in the Nearshore. *Journal of Geophysical Research.* 19,859-19,868. 2001.

Efunda. "Engineering Fundamentals." (2006) Accessed: February 21, 2006. Available online at: http://www.efunda.com/math/areas/CircularSegment.cfm

Flores, N.Z. and J.F.A Sleath. "Mobile Layer in Oscillatory Sheet Flow." *Journal of Geophysical Research.* (103). 1998

Foda, Mostafa. "Role of Wave Pressure in Bedload Sediment Transport." *Journal of Waterway, Port, Coastal and Ocean Engineering.* 243-249. Nov./Dec. 2003.

Foster, D.L., A.J. Bowen, R.A. Holman, and P. Natoo. "Field Evidence of Pressure Gradient Induced Incipient Motion." *Journal of Geophysical Research.*" Vol. 111. May 2006.

Gallagher, E.L., S. Elgar, and R. Guza. "Observations of Sand Bar Evolution on a Natural Beach." *Journal of Geophysical Research.* 3203-3215. Feb. 15, 1998.

Gollub, J. and Pine, D. "Microscopic Irreversibility and Chaos." *Physics Today.* Aug. 2006.

Guo, J.K. "Logartihmic Matching and its Applications in Computational Hydraulics and Sediment Transport." *Journal of Hydraulic Research*. 40(5). 555-565. 2001.

Groot, M. B.; M.D. Bolton, P. Foray, P. Meijers, A.C. Palmer, R. Sandven, A. Sawicki, and T.C. Teh. "Physics of Liquefaction Phenomena around Marine Structures." *Journal of Waterway, Port, Coastal, and Ocean Engineering*. July/August 2006.

The H. John Heinz III Center for Science, Economics, and the Environment. "Evaluation of Erosion Hazards Summary." Prepared for the Federal Emergency Management Agency. April 2000.

Henderson, S.M., J.S. Allen, and P.A. Newberger. "Nearshore Sandbar Migration Predicted by an Eddy-diffusive Boundary Layer Model." *Journal of Geophysical Research.* Vol. 109. 2004.

Hoefel, F., and S. Elgar. "Wave-induced Sediment Transport and Sandbar Migration." *Science.* 1885-1887. March 21, 2003.

Komar, P.D. and D.L. Inman. "Longshore Transport on Beaches." *Journal of Geophysical Research*. 75, 5914-5927, 1970.

Madsen, O.S. "The Stability of a Sand Bed Under Action of Breaking Waves." R.M. Parsons Laboratory Report No. 182. March 1974.

Madsen, O.S. " Mechanics of Cohesionless Sediment Transport in Coastal Waters." Coastal Sediments. 15-27. (1991).

Madsen, O.S. "Spectral Wave-Current Bottom Boundary Layer Flows." 24th ICCE. 384-398. 1994.

Mei, C.C., Stiassnie, M., and Yue, D. *Theory and Applications of Ocean Surface Waves*. World Scientific Publishing Company. 2005.

Meriam, J.L. and Kraige, L.G. *Engineering Mechanics Dynamics*. 4th Edition. John Wiley and Sons. 1997.

Northcutt, G. "Defending the Coast from Attack." *Erosion Control.* Nov./Dec. 2001.

Pilkey, O.H. and A.G. Cooper. "Society and Sea-Level Rise." *Science.* March 19, 2004. 1781-1782.

The Resources Agency of California. "California's Ocean Resources: An Agenda for the Future." July 1995. Accessed: October 9, 2005. Available online at: http://resources.ca.gov/ocean/html/chapt_5c.html

Sea Grant. "Reducing the Nation's Vulnerability to Coastal Natural Hazards." Accessed: October 9, 2005. Available online at: http://www.nsgo.seagrant.org/themesnpa/pdf/coastalhazards_impacts.pdf

Schlichting, H. *Boundary Layer Theory*. McGraw Hill Book Co. Inc. 1955.

Sherman, D. J., Barron, K.M., and Ellis, J.T. "Retention of Beach Sands by Dams and Debris Basins in Southern California." Journal of Coastal Research. Special Issue 36. 2002. 662-674.

Sontek. 2006. http://www.sontek.com. Last updated: May 19, 2006.

Soulsby, R. *Dynamics of Marine Sands.* Thomas Telford. 1997.

Skougaard. O. *et. al.* "Sinusoidal and Cnoidal Gravity Waves." Tables and Formulae., Institute of Hydrodynamics and Hydraulic Engineering. Technical University Denmark.

Sleath, A. I. "Simple Models of Turbulent Wave and Current Bottom Boundary Layer Flow: Theoretical Formulations and Applications" M.Sc. Thesis. MIT. 2002.

Sleath, J.F.A. "Conditions for Plug Formation in Oscillatory Plug." *Continental Shelf Research.* 19 (1999).

Surf Lifesaving Queensland. 2004. http://www.lifesaving.com.au/beachSmart/wavesRips.cfm Viewed: Sept. 11, 2006.

Thornton, E., R. Humiston, and W. Bierkemeier. "Bar/Trough Generation on a Natural Beach." *J. Geophys. Res.*, May 15, 1996, 12,097-12,110.

Zhang, K., Douglas, B.C., Leatherman, S.P. "Global Warming and Coastal Erosion." *Climatic Change.* 64: 41-58, 2004.